

Disorder in solids probed by NMR chemical shielding using semi-empirical dispersion corrected density functional theory

Dissertation

Zur Erlangung des akademischen Grades

Doktor der Naturwissenschaften (Dr. rer. nat.)

an der Fakultät Biologie, Chemie und Geowissenschaften der Universität
Bayreuth

vorgelegt von

Dominik Greim

geboren in Bayreuth

Bayreuth 2020

Die vorliegende Arbeit wurde in der Zeit von Mai 2014 bis Januar 2020 in Bayreuth am Lehrstuhl Anorganische Chemie III unter Betreuung von Herrn Professor Dr. Jürgen Senker angefertigt.

Dissertation eingereicht am: 21.01.2020

Zulassung durch die Promotionskommission: 12.02.2020

Wissenschaftliches Kolloquium: 30.10.2020

Amtierender Dekan: Prof. Dr. Matthias Breuning

Prüfungsausschuss:

Prof. Dr. Jürgen Senker (Gutachter)

Prof. Dr. Josef Breu (Gutachter)

Prof. Dr. Matthias Breuning (Vorsitz)

Prof. Dr. Roland Marschall





Für meine Familie.

Danksagung

Zuallererst möchte ich mich bei Jürgen bedanken, nicht nur für die Möglichkeit zu promovieren, sondern auch für die Freiheiten, die er seinen Doktoranden dabei lässt. Außerdem danke für die fachlichen Anregungen und für das Verständnis dafür, dass niemand alles wissen kann.

Außerdem bedanke ich mich bei meiner Familie, ganz besonders bei meiner Mutter, die immer hinter mir steht, sich meine Beschwerden über Sorgen und Probleme anhört hat und mir mit Rat und Tat zur Seite steht.

Selbstverständlich wäre meine Promotion ohne meine Freunde und Kollegen an den Lehrstühlen AC I, III und IV niemals möglich gewesen. Danke Helen, unsere alldonnerstäglichen Gesprächsrunden über fachliches und fachfremdes bleiben uns hoffentlich erhalten. Danke Marion, dafür dass du dafür gesorgt hast, dass es nie langweilig im Labor wurde. Danke Katja und Thomas für die netten Feierabende inklusive hochinteressanter Themen und Diskussion. Danke Tobi, für die langjährige Freundschaft und Unterstützung seit Beginn unseres Studiums. Danke Wolfgang und Beate für die jederzeit freundliche und engagierte Unterstützung in allen Bereichen, ob Forschung, Organisation oder Persönliches. Danke Robert, Lisa, Kevin, Adrian, Renée und alle die ich nicht namentlich genannt habe.

Ich möchte mich außerdem bei denen Bedanken, die den Lehrstuhl in der Zwischenzeit verlassen haben: Paul, Marko, Nadine, Klaus, Mario, Maria, Julia, Thomas W. und Kilian, ohne euch wäre die Anfangszeit am Lehrstuhl nicht halb so unterhaltsam gewesen und ich wäre vielleicht gar nicht in der ACIII gelandet.

Auch danke an „meine“ Studenten, die ich im Rahmen von Praktika betreuen durfte. Ich habe von euch mindestens genauso viel gelernt wie ihr von mir.

Und danke Natalie, für jeden einzelnen Tag.



Contents

Nomenclature.....	ix
Abstract	xi
Zusammenfassung.....	xiv
1. Introduction	1
1.1 NMR Crystallography.....	1
1.2 Quality of predictions of NMR and EFG properties by DFT.....	4
1.3 Investigation of disorder using NMR crystallography.....	8
2. Synopsis	12
2.1 Cs ₄ Ga ₆ Q ₁₁ (Q=S, Se).....	12
2.2 Idasanutlin.....	16
2.3 Disorder in Na ₃ [Al(L-lactate) ₃] * 6 H ₂ O	22
References	28
3. Index of Publications	34
4. Publications	36
4.1 Synthesis and Characteriszaion of Cs ₄ Ga ₆ Q ₁₁ (Q = S, Se) - Chalcogenometalates with Exotic Polymeric Anions	36
4.2 Polymorphism in Idasanutlin.....	60
4.3 The structure of Na ₃ [Al(L-lactate) ₃] ₂] * 6 H ₂ O crystallized from Lohtragon® Al 250 – a commercial cement adjuvant	96
5. Addendum	124
5.1 Density Functional Theory (DFT).....	124
The Kohn-Sham <i>ansatz</i>	125
Periodic boundary conditions and Pseudopotentials.....	128
The gauge including projector augmented wave method	129
Semi-empirical dispersion correction	132



Nomenclature

1D	One-dimensional
BZ	Brillouin-Zone
CP	Cross Polarization
DFT	Density Functional Theory
EFG	Electric field gradient
GIPAW	Gauge-including projector augmented wave
GGA	Generalized-gradient approximation
LDA	local density approximation
MAS	Magic Angle Spinning
PBE	Perdew-Burke-Ernzerhof functional
ssNMR	solid-state Nuclear Magnetic Resonance
PP	Pseudopotential
(P)XRD	(Powder) X-ray diffraction
vdW	van-der-Waals

Abstract

In this work NMR crystallography was used to solve five crystal structures of four different compounds. These range from inorganics incorporating new type of polymeric anions over metal organic to new organic pharmaceuticals. All of them exhibit different degrees of disorder in their crystal structure, which we investigated further, focusing on a combination of solid state nuclear magnetic resonance (ss-NMR) and density functional (DFT) methods. The latter employing semi empirical dispersion corrected density functional theory in conjunction with the gauge including projector augmented wave method. Due to the large size of the unit cells of those compounds it proved impossible to employ established techniques for DFT calculations like the supercell approach. Therefore, more simplified, less computational demanding approaches had to be used calculating only single unit cells in varying structures. Upon these, we were able to predict the isotropic chemical shielding for all incorporated NMR active nuclei within these chemicals, for which measurements were feasible, and also investigated quadrupolar coupling constants computed by DFT. This enabled us to assign NMR signals that could not be explained by the undistorted crystal structures.

The first two compounds, the chalcogengallates $\text{Cs}_4\text{Ga}_6\text{Q}_{11}$ (Q=S, Se), are the first of a new type, incorporating polymeric anions. They crystallize isotypically in the triclinic space group $P\bar{1}$ with one formula unit in the asymmetric unit and two formula units in each unit cell. In both compounds condensed GaQ_4 tetrahedra form complex anionic “Dreier double” chains ${}_{\infty}^1[\text{Ga}_6\text{Q}_{11}^{4-}]$. The ${}^{71}\text{Ga}$ NMR spectra measured at 14.1 T, that were still not well resolved, show at least three distinct crystallographic sites, potentially fitting both the crystal structure and the prediction by DFT. In contrast, ${}^{133}\text{Cs}$ shows very good agreement with the experiment for both used functionals, PBE and LDA, employing the zeroth order regular approximation. Both the experimental spectra and the DFT predictions show four signals for each structure, with two of them overlapping strongly in the case of the selenide. Using this crystal structure with altered stoichiometry for additional DFT calculations of the distorted structures enabled the assignment of additional signals in the ${}^{133}\text{Cs}$ NMR spectrum of $\text{Cs}_4\text{Ga}_6\text{Se}_{11}$ caused by defects. These take the form of an additional Selenide atom added to the polymeric anion chain forming a Ga-Se-Se-Ga bond sequence.

The third compound, Idasanutlin, is a potential drug for leukaemia treatment. The structure of two polymorphs, form I and III, crystallizing in space group $P1$ and $P2_1$, incorporating two and four formula units, were solved. The former using single crystal XRD based on synchrotron measurements, the latter using NMR crystallography. Both share the same dimer motif in which two single molecules are bridged by double hydrogen bonds *via* their acid groups. These dimers are stacked on top of each other in a chair like manner. The difference between phase I and III is an AB layering of modification III and ABC layering for polymorph I. The DFT predicted ^1H shifts reflect the difference of the hydrogen bonding within the two polymorphs and the differences in the packing for the amide hydrogen atom. The ^{13}C and ^{15}N NMR spectra show no conspicuousness with the DFT predictions of the isotropic chemical shifts of phase I show good agreement with the experimental spectrum. The ones of form III, though, show slight deviations between experiment and calculations for ^{15}N , probably caused by thermal motion. polymorph III additionally exhibits slight defects in the form of a benzene ring, rotated by 180° which is, in terms of NMR solely observable in the ^{19}F ssNMR spectra. Using the signal integrals and $^{19}\text{F}^{19}\text{F}$ DQSQ build-up curves together with DFT calculations of the distorted structure we were able to assign all ^{19}F signals and were able to conclude that the disorder is, in fact, distributed statistically throughout the crystallites.

The fourth compound, $\text{Na}_3[\text{Al}(\text{L-lactate})_3]_2 \cdot 6 \text{H}_2\text{O}$, was crystallized from commercial Lohtragon[®] solution and is commonly used in superabsorbers and as cement adjuvant. It inherits the space group $P3_2$ with one formula unit in the asymmetric unit. The crystal structure consists of two $\text{Al}(\text{L-lactate})_3$ complexes interconnected by three very short symmetrical hydrogen bonds *via* their half deprotonated hydroxy groups forming a binuclear $[\text{Al}(\text{L-lactate})_3]_2$ complex. These binuclear complexes are arranged in layers, with only vdW-interaction within those. In the interlayer space the negative charge is compensated by Na^+ ions which are additionally surrounded by water to reach distorted octahedral coordination. The binuclear complex could only be identified by the combination of ssNMR and DFT predictions due to a signal with very high shift observed in ^1H NMR. All other ^1H predicted shifts cover a broad range, while the experiment shows well resolved signals. This behaviour can be attributed to mobility, which could not be included into the predictions due to the sheer size of the unit cell. Though, through averaging of the shifts of each chemical group, it was possible to reach very good

agreement with the experimental ^1H NMR spectrum, as the high number of hydrogen atoms in the unit cell samples the energy hypersurface sufficiently. The ^{13}C predictions fit the experiment very well, the same is the case for the quadrupolar nuclei ^{23}Na and ^{27}Al and their coupling constants. The low temperature spectrum of ^{23}Na shows very good agreement with the predicted three sites. While for ^{27}Al the coupling fits the experiment well the asymmetry shows slight deviations, in line with results of other studies.

The findings in this work, mainly the investigations of the different types of disorder using ssNMR and DFT techniques, may help future crystal structure solutions of compounds exhibiting large unit cells.

Zusammenfassung

In dieser Arbeit wurden mit Hilfe von NMR-Kristallographie fünf Kristallstrukturen von vier verschiedenen Verbindungen gelöst. Diese reichen von einer neuen Art anorganischer polymerer Anionen über metallorganische binukleare Aluminiumkomplexe bis hin zu organischen Pharmazeutika. Allen gemein ist, dass sie zu einem gewissen Grad Fehlordnung in ihrer Kristallstruktur aufweisen, welche durch eine Kombination von Festkörper nuklearer magnetischer Resonanz (FK-NMR) und Methoden auf Basis der Dichtefunktionaltheorie (DFT) detailliert untersucht wurde. Letztere Methode umfasste die semi-emprirische Korrektur von Dispersionswechselwirkungen und die Berechnung von NMR-Parametern auf Basis der *gauge including projector augmented wave* Methode. Aufgrund der Größe der Einheitszellen der Verbindungen war es unmöglich diese durch konventionelle Herangehensweisen, wie z.B. den Superzellen-Ansatz zu berechnen. Deshalb musste auf einfachere, weniger anspruchsvolle Arten für die Berechnung zurückgegriffen werden, bei denen die Ergebnisse nur auf Variationen einzelner Einheitszellen beruhen. Mit diesen konnte sowohl die isotrope chemische Verschiebung der vorhandenen NMR-aktiven Kerne, als auch die quadrupolare Kopplung von Spin $> \frac{1}{2}$ Kernen der Verbindungen vorhergesagt werden. Dies ermöglichte eine Zuordnung von Signalen in FK-NMR-Experimenten, die durch die Strukturen ohne Fehlordnung nicht erklärt werden konnten.

Die ersten beiden Verbindungen, die Chalkogengallate $\text{Cs}_4\text{Ga}_6\text{Q}_{11}$ (Q=S, Se) sind die ersten einer neuen Art, die polymere Anionen enthalten. Sie kristallisieren isotypisch in der triklinen Raumgruppe $P\bar{1}$ mit einer Formeleinheit in der asymmetrischen Einheit und zwei Formeleinheiten in der Einheitszelle. Beide Verbindungen bestehen aus GaQ_4 Tetraedern die durch Kondensation komplexe anionische „Dreier“ Doppelketten mit der Formel $\infty[\text{Ga}_6\text{Q}_{11}^{4-}]$ ausbilden. Trotz der Messung der ^{71}Ga FK-NMR-Spektren bei 14,1 T war es nur möglich eine Mindestanzahl an drei kristallographisch unterschiedlichen Ga-Positionen zu bestimmen, was prinzipiell sowohl zur Kristallstrukturlösung als auch zu den Vorhersagen durch DFT Berechnungen passt. Hingegen zeigen die experimentellen ^{133}Cs FK-NMR-Spektren sehr gute Übereinstimmung mit Berechnungen sowohl auf Basis des PBE Funktionals als auch auf Basis der lokalen Dichtenäherung unter Verwendung der *zeroth order regular*

approximation. Sowohl Experiment als auch Vorhersage zeigen vier Signale für beide Verbindungen, von denen die mittleren Beiden im Fall des Selenids überlappen. Durch DFT Berechnungen mit unterschiedlicher Stöchiometrie der Kristallstruktur des Selenids konnten weitere Signale, die im ^{133}Cs FK-NMR-Spektrum auftauchen als Defekte zugeordnet werden. Diese zeigen die Form von zusätzlichen Selenidatomen innerhalb der polymeren Anionenkette und führen zu einer Ga-Se-Se-Ga Bindungsfolge.

Die dritte Verbindung, Idasanutlin, ist ein Arzneimittelkandidat zur Behandlung von Leukämie. Es wurden die Kristallstrukturen der beiden Polymorphe I und III, die in den Raumgruppen $P1$ und $P2_1$ mit zwei, respektive vier Formeleinheiten in der Einheitszelle kristallisieren gelöst. Während erstere Struktur durch Röntgendiffraktion gelöst wurde, war für Zweitere NMR-Kristallographie notwendig. Beide Polymorphe zeigen dasselbe Dimermotiv bei dem zwei Moleküle über ihre Säuregruppen doppelt wasserstoffbrückengebunden sind. Diese Dimere sind in den Kristallstrukturen vergleichbar mit Stühlen übereinandergestapelt. Der Unterschied zwischen Modifikation I und III ist eine AB-Schichtung dieser Stapel im Fall von Phase III und einer ABC-Schichtung bei I. Die Vorhersage der chemischen Verschiebung von ^1H zeigt den Unterschied in den Wasserstoffbrückenbindungen und die unterschiedliche Umgebung des Wasserstoffs der Amidgruppe aufgrund des Packungsunterschieds. Während die ^{13}C und ^{15}N FK-NMR-Spektren und deren Vorhersage für Form I keine Auffälligkeiten erkennen lassen, zeigen sich leichte Abweichungen für ^{15}N im Fall von Polymorph III. Außerdem zeigt Modifikation III eine Fehlordnung innerhalb der Struktur in der ein fluoro-chloro-Benzolring eines der Moleküle um 180° verdreht ist, was sich in den ^{19}F FK-NMR-Spektren beobachten lässt. Durch die Integrale dieser Signale in Verbindung mit $^{19}\text{F}^{19}\text{F}$ DQSQ-Aufbaukurven und DFT Berechnungen der fehlgeordneten Struktur konnten alle Signale zugeordnet werden. Zusätzlich konnte herausgefunden werden, dass die Fehlordnung statistisch innerhalb der Kristallite verteilt ist.

Die vierte Verbindung, $\text{Na}_3[\text{Al}(\text{L-Lactate})_3]_2 \cdot 6 \text{H}_2\text{O}$, wurde aus kommerziell erhältlicher Lohtragon[®] Lösung kristallisiert, die breite Anwendung beispielsweise in Superabsorbent und Betonzusatzstoff findet. Es bildet eine Struktur in der Raumgruppe $P3_2$ mit einer Formeleinheit in der asymmetrischen Einheit. Die Grundbausteine bestehen aus zwei $\text{Al}(\text{L-Lactate})_3$ Komplexen, die über drei sehr kurze symmetrische Wasserstoffbrückenbindungen über ihre halb deprotonierten OH Gruppen verbunden sind. Diese binuklearen Komplexe bilden Schichten innerhalb derer lediglich

van-der-Waals-Wechselwirkungen zu beobachten sind. Im Zwischenschichtraum wird die negative Ladung durch Na^+ -Ionen ausgeglichen, die zusätzlich von Wasser komplexiert werden um eine verzerrt oktaedrische Koordination zu erreichen. Die binuklearen Komplexe konnten einzig durch die Kombination von FK-NMR und DFT Berechnungen identifiziert werden, da im ^1H FK-NMR-Spektrum ein stark verschobenes Signal beobachtet wurde. Alle anderen ^1H Vorhersagen zeigen eine breite Verteilung der Verschiebungen, während das Experiment klar aufgelöste Signale zeigt. Diese Diskrepanz ist auf die fehlende Mobilität in den DFT Vorhersagen zurückzuführen, die aufgrund der schieren Größe der Zelle der Struktur nicht in die Berechnung einbezogen werden konnte. Es war allerdings möglich durch Mittelung der Verschiebung der einzelnen chemischen Gruppen eine gute Übereinstimmung mit dem Experiment herzustellen, da die hohe Anzahl an Wasserstoffatomen innerhalb der Struktur die Energiehyperfläche der Einheitszelle bereits ausreichend abtastet. Sowohl die NMR Vorhersagen für ^{13}C als auch die Berechnung der quadrupolaren Kopplungskonstanten für ^{23}Na und ^{27}Al passen zum Experiment. In der Tieftemperaturmessung von ^{23}Na zeigen sich deutlich drei kristallographisch unterschiedliche Positionen. Während die vorhergesagte Kopplung für ^{27}Al gut zum Experiment passt, zeigen sich für den Asymmetrieparameter leichte Abweichungen, die aber bereits in anderen Studien beobachtet wurde.

Die Ergebnisse dieser Arbeit, besonders die Untersuchungen verschiedener Arten von Fehlordnung mit Hilfe von FK-NMR und DFT-Methoden könnte bei zukünftigen Lösungen von Kristallstrukturen helfen, die große Einheitszellen aufweisen.

1. Introduction

1.1 NMR Crystallography

Characterizing the structure of crystalline powders is one of the major challenges in modern chemistry. In both, new materials and pharmaceutical applications, the amount of such samples is growing. Information about the three-dimensional structure of these materials is crucial to be able to identify trends and predict and enhance physical properties like E-modulus, transparency, the melting point or solubility.^[1] Therefore, recently significant progress was made in different fields of structural characterization, namely PXRD,^[2–6] ssNMR^[7–10] and quantum mechanical simulations.^[11–14] The combination of these methods, called NMR crystallography,^[15,16] enables crystal structure solutions that were not feasible before.^[12,17,18]

XRD is based on constructive interference of the diffracted X-ray beams on the electron clouds which follows the Bragg-equation:^[19]

$$2d \sin \theta = n\lambda \quad (1.1.1)$$

where d is the interplanar distance, n is a positive integer, λ the wavelength of the incident wave and θ the scattering angle. As the X-ray beam penetrates the whole powder sample due to the relatively weak interaction of electromagnetic waves with matter, the diffraction pattern is an average over the whole of it. Additionally, when dealing with powders, reflex overlap causes a significant loss of accessible information. Therefore, the information from PXRD is of a long-range nature, like e.g. the size and symmetry of the unit cell. For samples crystallizing in higher symmetries like cubic or hexagonal crystal systems usually a cell can be found by indexing the reflexes. For large cells with low symmetry this becomes increasingly difficult, especially due to reflex overlap, but is sometimes still feasible.^[20–22]

To interpret the diffraction pattern, it is important to know the structure factor F_{hkl} as it determines the phase and amplitude of the x-ray beams:

$$F_{hkl} = \sum_{j=1}^N f_j e^{-2\pi i(hx_j + ky_j + lz_j)} \quad (1.1.2)$$

this sums over all atoms j within the unit cell. x , y and z are the coordinates of each atom, hkl being the Miller indices and f is the element dependent scattering factor

NMR on the other hand, is sensitive to short-range environmental effects like bonding or packing. It is based on the fact that the energy levels of spin up and spin down split up in strong external magnetic fields B_0 called Zeeman effect:^[23,24]

$$\Delta E = \gamma \hbar B_0 \quad (1.1.3)$$

With γ being the nucleus dependant gyromagnetic ratio and \hbar the reduced Planck constant.

Different effects can be used for structural determination, with the most common ones being chemical shift, direct dipole-dipole and quadrupolar interactions. The former describes the interaction of external applied magnetic fields with the local field induced by the electron current at the nucleus position. It is obviously dependent on the orientation of the molecule and therefore, the crystallite as a whole to the external field, which results in broad NMR spectra for powdered samples. This can be overcome using magic angle spinning, where the sample is rotated around an axis inclined by 54.74° with respect to the external magnetic field to average out all anisotropic parts of the chemical shielding tensor, leaving only the isotropic shielding (Figure 1). The latter can give insights into properties like bonding oxidation state and local environment, which are resembled in the chemical shift that a resonance experiences. Intensities of resonances can be used to identify the number of independent crystallographic sites within the asymmetric unit cell of a compound's crystal structure.^[15,25]

The dipole-dipole interaction, due to it being only dependant on constants and the inverse of the cubic distance, can be used to measure distances, or distance distributions between atoms.^[26]

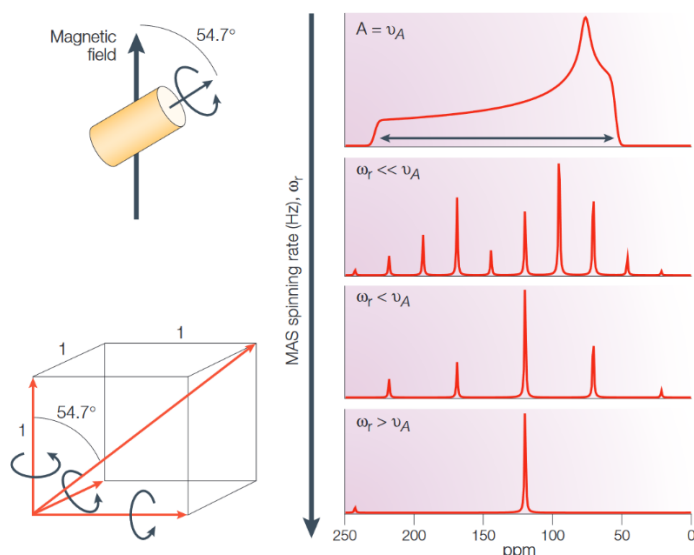


Figure 1: Schematic depiction of the MAS experiment in which a polycrystalline sample is rotated about an axis inclined at the magic angle of 54.74° to the external field at a spinning rate ω_r and the effect on the NMR spectrum this has. Reprinted by permission from Copyright.com, Nature, Nature reviews Drug Discovery, 4, pages555–568(2005) Copyright 2005 ^[27]

Quadrupolar interactions are an important tool for structure solutions as most the NMR active nuclei available have a spin $> \frac{1}{2}$. These nuclei exhibit a quadrupole moment, meaning that the charge distribution is non-spherical, which lets them interact with the electric field gradient (EFG) at their position. This makes quadrupolar nuclei very sensitive to their direct surrounding and bonding scenario, therefore coordination polyhedral and numbers are easily accessible structural information.^[28] Validation of structure models is possible through simulations using DFT level calculations of NMR parameters, which are explained in the addendum (5.1).

The combination of these methods enables high precision predictions of NMR parameters of all kinds of compounds for structure validation^[29,30] and has even been used to solve structures without the need for diffraction techniques.^[31]

1.2 Quality of predictions of NMR and EFG properties by DFT

While the vast majority of chemical elements have at least one NMR active isotope^[32] we will concentrate on the following, as these were part of the publications this thesis is based on: ^1H , ^{13}C , ^{15}N , ^{19}F , ^{23}Na , ^{27}Al , ^{69}Ga and ^{133}Cs with focus on the isotropic chemical shift and for the latter four quadrupolar couplings. To be able to assess the abilities and boundaries of NMR crystallography and especially DFT predictions of NMR parameters it is important to have a rough overview about the current state of results in this field for these nuclei which is given in the following.

For ^1H it has been shown that the prediction of the ssNMR parameter is in good agreement with experiment (e.g. exemplary Figure 1, left side) and that the chemical shift is an extremely good indicator of hydrogen bonding in all sorts of structures.^[12,18,33–36] There is a distinct relation between length of the hydrogen bond and the isotropic chemical shift of the bound hydrogen atom.^[37] Depending on the functional used for calculation, the strength of the hydrogen bonding and therefore the isotropic chemical shift tends to be overestimated^[38] even though this can also be accounted to thermal effects not being included in DFT calculations. The latter can be overcome by application of dynamics simulations in cases with fewer atoms.^[39,40] These thermal effects are in general the main cause of discrepancies between the ssNMR prediction and measurements due to the fact that light nuclei and chemical groups are easily thermally excitable.^[41]

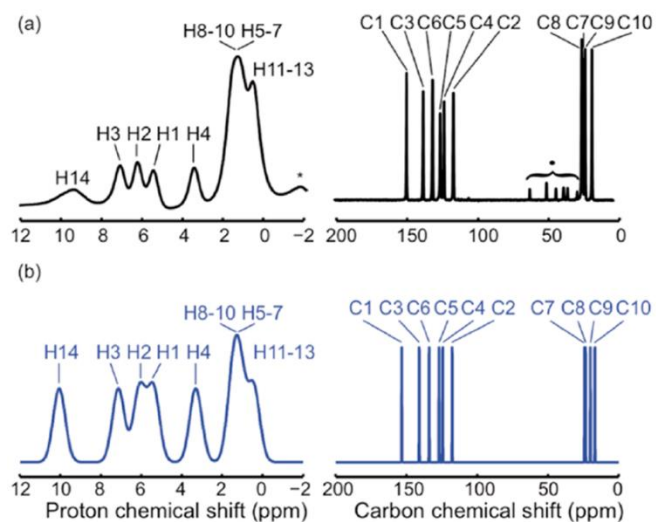


Figure 2: Experimental and DFT calculated ^1H and ^{13}C NMR spectrum of Thymol. Reprinted with permission from ^[42] Copyright 2012 American Chemical Society.

Just like ^1H , ^{13}C NMR predictions are very well evaluated through the vast number of publications on the topic and are proven to be in good agreement with experiment (see exemplary Figure 2, right side and (Figure 3),^[12,42–50] even comparing to liquid measurements^[51–54] and many articles comparing quality of the calculations.^[55–59] While calculations of ^{13}C NMR parameters have become widely applicable, one main problem is that for complex molecules a lot of resonances in near vicinity of each other, like e.g. substituted benzene rings, with differences in shift that are so small that they can't be reliably reproduced with DFT methods.^[44]

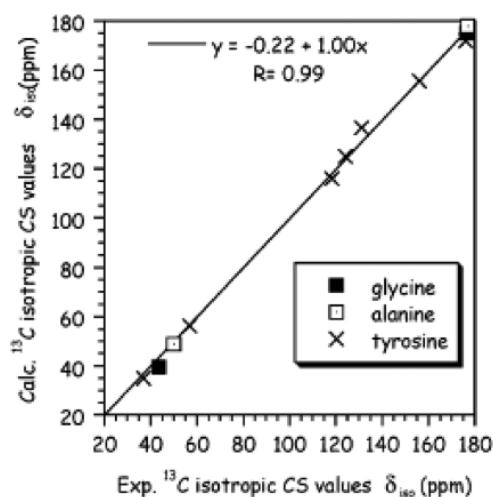


Figure 3: Experimental and calculated ^{13}C isotropic shifts for L-alanine, L-Tyrosine and α -glycine. Reprinted with permission from ^[39] Copyright 2012 American Chemical Society

^{15}N , in contrast to ^1H and ^{13}C , is a low abundant nucleus^[32] which results in considerably longer measurement times. This explains why DFT predictions of ^{15}N NMR are not as thoroughly investigated as they are for the latter. There are however plenty for solids,^[60–65] as well as liquid NMR^[66,67] and reviews on the topic available.^[68–70] It has been shown that the mean absolute errors of the isotropic chemical shift for ^{15}N compared to the experiment is considerably higher than for ^{13}C when using common functionals like LDA and PBE but can be reduced by using the KT functional.^[70–72] On the other hand it is not common practice to use a different functional for certain nuclei. Much rather this means that these functionals can still be improved in terms of their accuracy for ^{15}N predictions.

^{19}F , as a terminal group in organic chemistry, is very sensitive to packing and therefore of special interest for NMR crystallography.^[73] It is therefore well investigated^[12,74–84] and it has been shown in several studies that the linear scaling of the negative calculated isotropic shielding with the experimental isotropic shift deviates from the expected slope of -1 (Figure 4).^[78,84] Additionally, the same behaviour has been observed for Chlorine.^[85]

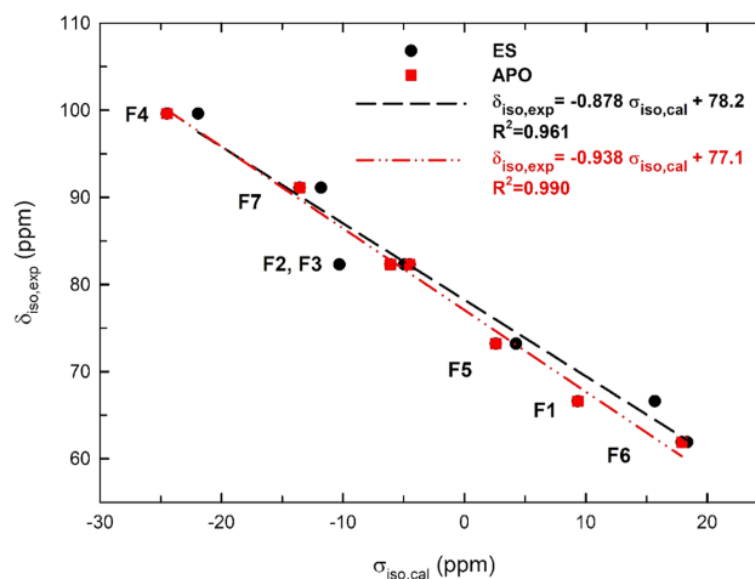


Figure 4: Plot of experimental isotropic chemical shift against calculated ^{19}F isotropic chemical shielding of ThF_4 . Slopes deviate considerably from -1. Reprinted with permission from [76] Copyright 2018 American Chemical Society

In the case of ^{23}Na the isotropic shift range of its usual oxidation state +1 is rather small and depends mainly on its coordination number.^[28,86] On the other hand as a 3/2 nucleus it has a rather large quadrupolar coupling and makes it therefore interesting for studies of its surrounding. The DFT-employing investigations mainly focus on inorganic structures, showing good agreement between experiment and prediction,^[76,87,88] even if signal overlap is significant.^[89]

^{27}Al is a 5/2 quadrupolar nucleus^[32] which in conjunction with the isotropic shift and DFT predictions can be used to probe the close surrounding of Al^[90,91] and intramolecular structures.^[92,93] This has been tested in several studies,^[94,95] finding that while both CSA and EFG calculations show good agreement with the experiment in most cases,^[96] the quadrupolar asymmetry parameter has a rather high error margin in some cases.^[84,95,97,98]

While Gallium, with ^{69}Ga being a 3/2 quadrupolar nucleus, is not commonly investigated, there are some studies on the accuracy of DFT predictions of NMR parameters. Some of these show good agreements with the experiment,^[99,100] but there are also cases in which the quadrupolar coupling constants deviate considerably from the experiment.^[101–103]

Data on calculations of the quadrupolar spin 7/2 nuclei ^{133}Cs is sparse but shows good agreement in prediction of trends, even though the accuracy can't be rated reliably as only three publications are known to the author up until today.^[104–106] The quadrupolar

coupling for this nucleus is negligible small,^[32] therefore quadrupolar predictions are not discussed.

With the accuracy that is achieved with these modern DFT calculations it is possible to achieve investigations that are rarely feasible with other methods like e.g. XRD. In these cases, the local character of NMR is used to identify structural features that are rarely accessible with other methods, namely, disorder.

1.3 Investigation of disorder using NMR crystallography

There are several types of disorder in crystalline solids (Figure 5). While in inorganic solids vacancies (Figure 5b/c) and substitutional defects (Figure 5e) are very common, solids become more and more prone to dislocational disorder (Figure 5d & f) the less spherical their smallest building units become in both geometry and charge. The added complexity leads to a more intricate energy hypersurface with more local minima, giving rise to conformational and orientational discrepancies, that can, ultimately, lead to completely different crystal structures.^[1,107]

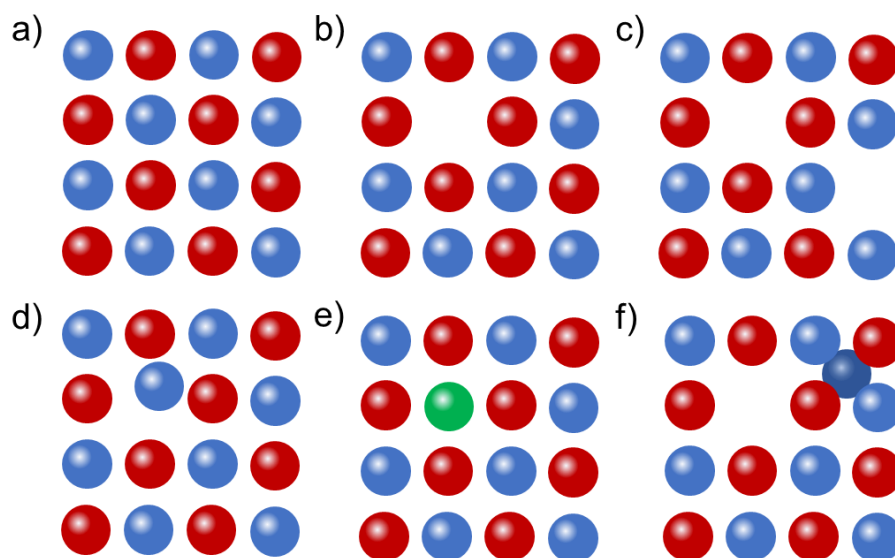


Figure 5: Ordered crystalline AB material (a), with A site vacancies (b), Schottky defect (c), distorted A site (d), ion replacement (e) and Frenkel defect (f). Each of the shown types of disorder can also occur in combination with each other.

Due to the fact that NMR is very sensitive to changes in the near vicinity of the nucleus measured, it is possible to observe the influence defects and disorder not only on the position they occur but also in the first and also second coordination sphere.^[108,109] While the most obvious impact on the measurement is the influence on the chemical shift

(Figure 6), there is also an effect on other NMR parameters, like anisotropy and on quadrupolar couplings.^[23] Furthermore, for quadrupolar nuclei the coupling is dependent on the symmetry of the charge distribution around the observed nucleus making quadrupolar nuclei a very powerful tool to investigate disorder in solids.^[110]

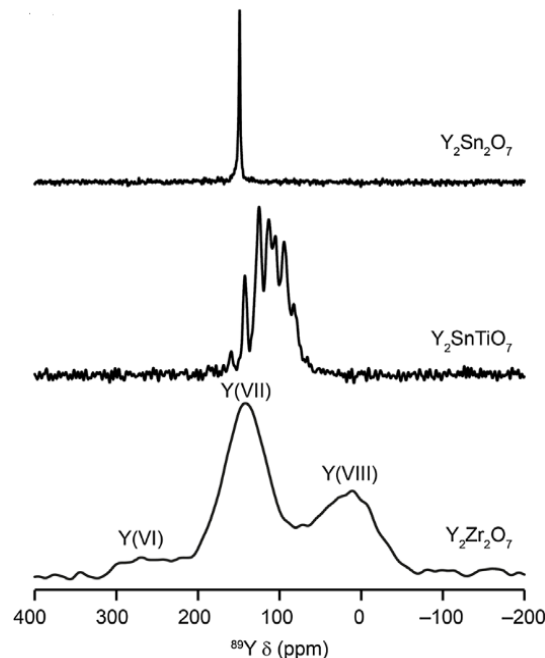


Figure 6: ^{89}Y MAS NMR spectra of three isotructural compounds without disorder (top), B-site cation disorder (middle) and both cation and anion disorder (bottom). Reprinted with permission from ^[25], Copyright 2017 Taylor & Francis Online

While in the past it was common to calculate NMR properties through DFT-based local methods using a cluster approach (Figure 7a) advances have led to periodic boundary conditions being the de facto standard for calculations of solids.^[79,111] While for calculations of non-disordered solids can be carried out just by using the crystal structures, the procedure to calculate properties of disordered materials became more complicated. Since these calculations are carried out under periodic boundary conditions a simple replacement of atoms within the unit cell alters the stoichiometry of the compound that is being calculated. Therefore it is necessary to multiply the original unit cell along at least one axis and then introduce disorder in the now bigger cell (Figure 7b & c). This of course adds a lot to the cost of each calculation as each supercell contains a multiple of atoms the original cell and inhibits less symmetry.^[25]

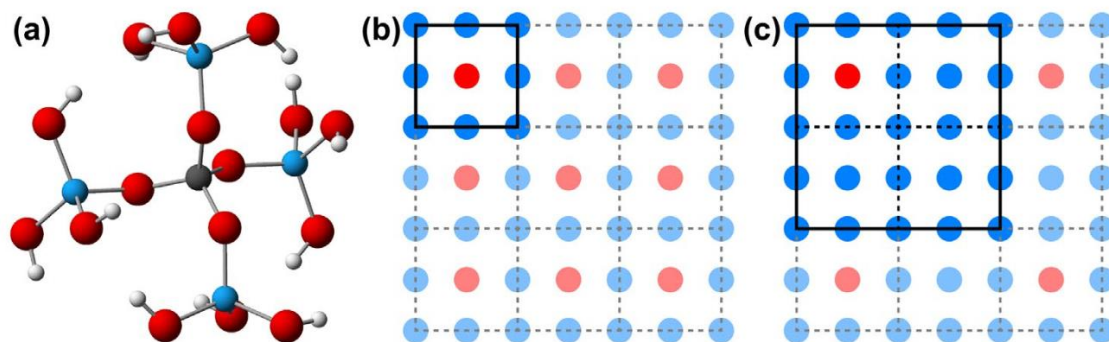


Figure 7: Representation of calculation approaches for disordered solids on the example of aluminiumphosphate: molecular approach using a cluster of aluminiumphosphate, saturated by OH groups (a) defect introduced into the unitcell and therefore altering the stoichiometry (b) and a 2x2 supercell of (b) with disorder (c) with lower impact on stoichiometry. Reprinted with permission from ^[25], Copyright 2017 Taylor & Francis Online

Another problem of such calculations that commonly occur are discrepancies caused by thermal motion. This is usually taken into account by employing molecular dynamics on DFT basis to the disordered supercell structures. After the equilibration of the system, for each step of MD simulation an additional NMR calculation is carried out. Averaging over the ensemble that is generated by this approach yields the thermal (Boltzmann weighted) average NMR parameters.^[30] This obviously not only adds the molecular dynamics calculation itself on top of the calculations, but it makes additional calculations of the NMR parameters of each step of the structure in motion necessary. Therefore, this approach can only be used for small systems while using plenty of computational resources.^[25]

There are numerous studies on defects and disorder in solids using these techniques,^[15,16,112] with topics spanning over the whole reach of solids including batteries^[113,114], solar cells^[98,115] fuel cells^[116] and even investigations of water within the earths deep interior.^[18] Another recent developed approach is ab initio random structure search. This is a method to screen for crystal structures of a given compound solely by computational means. It generates random unit cells and fills these with an appropriate number of atoms or molecules of the compound investigated and subsequently geometry optimizes the resulting structure. In this fashion it scans the energy hypersurface quite similar to molecular dynamics, but with the advantage of including variations of the unit cell.^[117] While this is a highly generalized approach it comes at the cost of having to calculate thousands of structures to sufficiently sample the structural energy

hypersurface. Therefore, it is highly computational demanding and not a viable option for large molecules and unit cells.^[35,111]

As mentioned before calculations of large disordered systems using these methods is not feasible. Therefore, we employed different simplified versions of them within this thesis to solve the structure and the disorder within these for three different compounds ranging from organic pharmaceuticals, like Idasanutlin, over metalorganic compounds, like $\text{Na}_3[\text{Al}(\text{L-lactate})_3] \cdot 6 \text{H}_2\text{O}$, to inorganic compounds incorporating heavy atoms like $\text{Cs}_4\text{Ga}_6\text{Q}_{11}$ (Q=S,Se). In the case of $\text{Cs}_4\text{Ga}_6\text{Se}_{11}$ we used calculations of single unit cells while altering the stoichiometry since the defect structure showed an additional Selenide atom. For Idasanutlin we simulated single unit cells as well, but the occurring disorder does not alter the sum formula. For $\text{Na}_3[\text{Al}(\text{L-lactate})_3] \cdot 6 \text{H}_2\text{O}$ only a single calculation for the unit cell was carried out since the unit cell has a very large volume (1833\AA^3). We then used the one of the problems of calculations such big unit cells, namely the high number of atoms, to sample the energy hypersurface by averaging over each chemical group.

2. Synopsis

This work consists of one manuscript and two publications (see Chapter 3 & 4) dealing with crystal structure solutions using an NMR crystallographic approach of four compounds exhibiting five crystal structures, that are all distorted in different ways. While the structure solution followed the known XRD and NMR approach for powdered or single crystal samples,^[3,118] additional insights into the nature of disorder in these solids was gained by the combination of DFT calculations and NMR. Due to the size of the unit cells these compounds form, different, less computational demanding approaches than the ones explained in 1.3 were necessary, while retaining the periodicity.

2.1 Cs₄Ga₆Q₁₁ (Q=S, Se)

Cs₄Ga₆Q₁₁ are the first two compounds of a new class of chalcogenogallates with polymeric anions. These complement the quasi-binary phase diagram of Deiseroth and Han^[119] and add a new phase diagram for the Sulfidic system. Both crystallize isotypically in the triclinic space group $P\bar{1}$ and the unit cell comprises of two formula units.

The six crystallographically independent gallium sites are surrounded by Se or S tetrahedrally. These tetrahedrons are connected to form characteristic anionic Ga₆Q₁₁⁴⁻ double strands. While within the strands the tetrahedrons are mostly connected edge-sharing, the bond between the strands are solely corner-sharing (Figure 8). The Ga tetrahedrons are deformed to varying degree with the least distortion being one site that is connected only corner sharing. The Cs sites are coordinated ten times within a sphere of 5.0 Å.

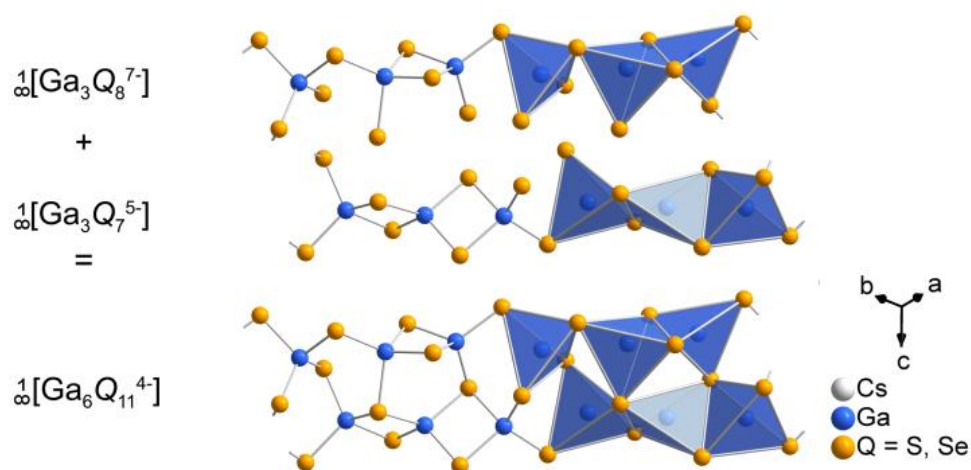


Figure 8: Ga_6Q_{11} substructure with the polymeric edge sharing chains that are connected corner sharing to a second chain to form double strands. © 2018 Wiley-VCH Verlag GmbH & Co. KGaA, Weinheim

The recorded ^{71}Ga NMR spectra show broad shapes due to the quadrupolar nature of the nucleus. Experimental fitting yielded at least three different crystallographic sites. In the case of $\text{Cs}_4\text{Ga}_6\text{S}_{11}$ (Figure 9 left) and $\text{Cs}_4\text{Ga}_6\text{Se}_{11}$ (Figure 9 right) the calculated NMR parameters for ^{71}Ga show potentially good agreement with the experimental spectra, but the latter lack the resolution to make a reliable statement about the accuracy of the predictions. It would therefore have been necessary to record spectra at higher fields to reliably evaluate the quality of the DFT predictions.

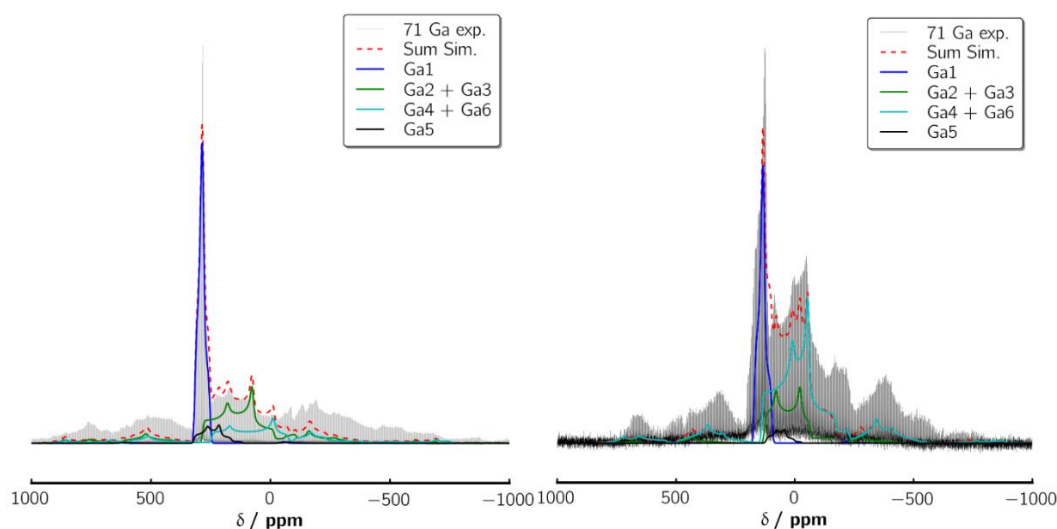


Figure 9: ^{71}Ga QCPMG-MAS ssNMR spectra of $\text{Cs}_4\text{Ga}_6\text{S}_{11}$ (left) and $\text{Cs}_4\text{Ga}_6\text{Se}_{11}$ (right) measured at a field of 14.1 T with the DFT predicted spectrum (red dashed line) and its single sites.

The ^{133}Cs ssNMR spectra of both compounds, $\text{Cs}_4\text{Ga}_6\text{S}_{11}$ and $\text{Cs}_4\text{Ga}_6\text{Se}_{11}$, show four signals, even though in case of the latter the signal width merges two of these into a single signal (Figure 10). This fits the four crystallographic independent Cs sites that were found in the crystal structure solution. We also compared the ^{133}Cs isotropic shift yielded by both LDA and PBE functionals, both while additionally employing the zeroth order regular approximation, with the experiment. The accuracy of both functionals is very good with the experiment lying in between the two.

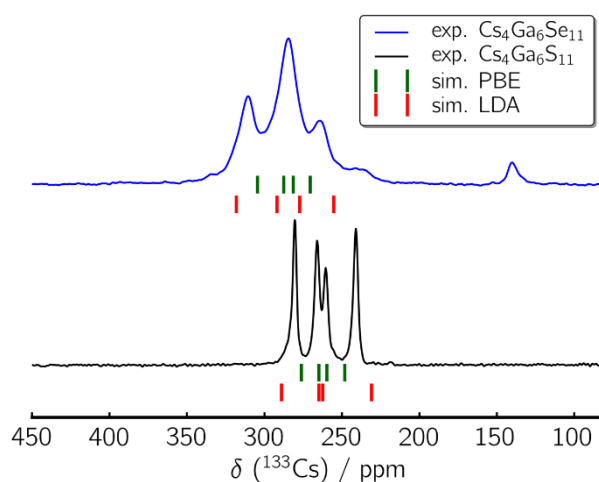


Figure 10: ^{133}Cs ssNMR MAS spectra of $\text{Cs}_4\text{Ga}_6\text{S}_{11}$ (bottom) and $\text{Cs}_4\text{Ga}_6\text{Se}_{11}$ (top) with the DFT predicted isotropic shifts for the functionals PBE (green) and LDA (red). © 2018 Wiley-VCH Verlag GmbH & Co. KGaA, Weinheim

Due to the very good prediction yielded from both functionals we investigated the disorder incorporated in the Selenide compound. According to the crystal structure solution this disorder occurs in the form of an additional Selenide atom within the GaSe strands.

Even though $\text{Cs}_4\text{Ga}_6\text{Se}_{11}$ is the smallest compound in terms of number of atoms and unit cell investigated within this thesis, it is already too large and therefore computational demanding, to be able to employ the super cell approach. Therefore, the calculations for the disordered structure were modelled using one and two of the aforementioned defects within a single unit cell, resulting in a stoichiometry of $\text{Cs}_4\text{Ga}_6\text{Se}_{11.5}$ and $\text{Cs}_4\text{Ga}_6\text{Se}_{12}$, respectively. Even though this is a rather simplistic approach, this enabled us to assign the additional signals that occurred in the experimental spectrum of the selenide compound (Figure 11). The simulations show a downshift in the ppm range for the Cs site at 240 ppm independent of the employed functional. We were therefore able to conclude that the small signal at ~ 240 ppm is caused by a single defect per unit cell while the additional signal at ~ 140 ppm might be caused by a double defect unit cell. It has to be noted though, that this approach does have its limits. The calculations are only able to give trends for the isotropic shifts and can't be seen as a tool to pinpoint exact shift values. It therefore remains uncertain if the additional signal at 140ppm is actually caused by the defect or by something else, since none of the calculations show a downwards shift that strong.

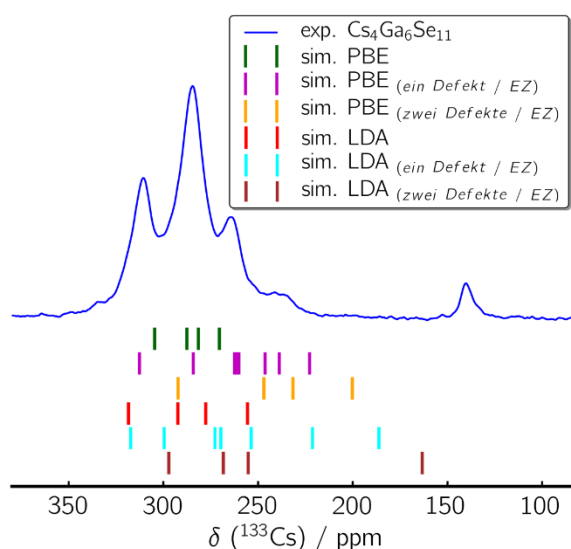


Figure 11: ^{133}Cs ssNMR MAS spectra of $\text{Cs}_4\text{Ga}_6\text{Se}_{11}$ with the DFT predicted isotropic shifts for the functionals PBE and LDA for different (non-)defect configurations of the structure. © 2018 Wiley-VCH Verlag GmbH & Co. KGaA, Weinheim

2.2 Idasanutlin

Idasanutlin (Figure 12) is an active pharmaceutical agent that serves as antagonist to the MDM2 binding receptors. This makes it interesting as a potential drug to fight leukaemia. During our studies of the crystal structures besides of different co-crystals incorporating solvents we found two pure polymorphs, form I and III being (meta-)stable at ambient conditions. Due to the lack of a single crystal structure solution of modification III we solved the structure during this project using a combination of PXRD and NMR spectroscopy. In the meantime, though, a single crystal solution became available through a cooperation partner which proved our solution correct and to which we resort to in this work due to the higher quality of the solution.

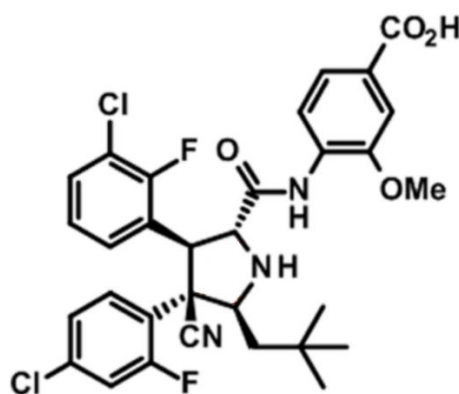


Figure 12: Structure of Idasanutlin

In both crystal structures two molecules form a dimer through double hydrogen bonds realized over their acid groups (Figure 13a&b). These dimers are then stacked in a chair like manner on top of each other (Figure 13c) forming rods which are then arranged in a brick like manner. The difference of polymorph I & III is the arrangement of these rods. While in phase I these are stacked in an ABC like layering where each layer is shifted by $1/3$ towards the underlying, form III exhibits an AB like stacking where the second layer is shifted by $1/3$ as well, but the third layer is then shifted back by $-1/3$ to form an AB like structure. Besides this the differences between the two are minor, with the main difference being that the hydrogen bonding between the dimers is symmetric for polymorph I while it is asymmetric for phase III. Additionally, the latter exhibits disorder in its crystal structure where a fraction of 0.23 of one of the molecules benzene rings is rotated by $\sim 180^\circ$.

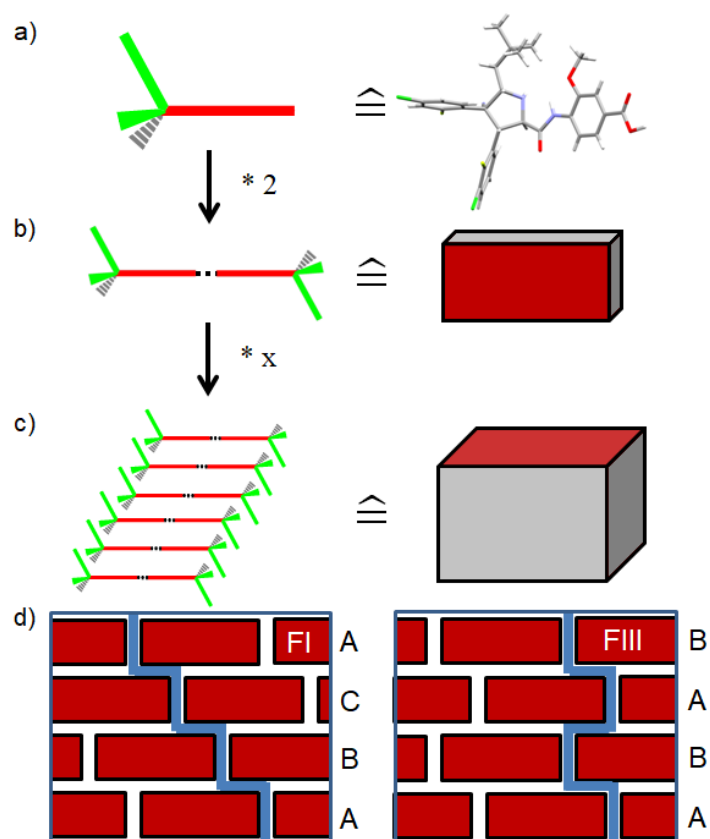


Figure 13: Packing scheme of form I and III of Idasanutlin with the scheme of a single molecule (a), the scheme of a dimer (b), the chair like packing of those dimers (c) and the brick like arrangement of form I and III (d)

The crystal metrics of both of form I are $a=6.525$ $b=12.926$ $c=18.359$ $\alpha=99.62^\circ$ $\beta=91.60^\circ$ and $\gamma=94.15^\circ$, while form III exhibits $a=26.000$ $b=18.565$ $c=6.494$ and $\beta=91.86^\circ$. In contrast to the non-symmetric triclinic structure of polymorph I, polymorph III crystallizes in the monoclinic space group $P2_1$ with a unit cell double the size of the former. This leads to the fact that the unit cells inhibit two molecules in the case of phase I and four in modification III. To accommodate for the disorder in polymorph III and due to the sheer number of atoms in the unit cell of this compound, we again employed a simplistic approach of additionally DFT-calculating a unit cell incorporating the rotated benzene ring. This also implies that we were not able to conduct molecular dynamics and therefore no motional effects on the predicted NMR parameters are included.

The case study of Idasanutlin clearly illustrates the importance of ^1H NMR spectra for NMR crystallography. While the packing of the two polymorphs merely differs, there are distinct differences observable in both the spectra and DFT predictions. For form I the hydrogen bonding of the dimer structure only shows a single signal, pointing towards symmetrical hydrogen bonding, whereas for form III two signals show up indicating an asymmetrical hydrogen bonding pattern. The second distinct feature that can clearly be assigned are the signals of the amide groups in both polymorphs, where in modification I two resonances and in phase III a single resonance is predicted by DFT and observed in the spectra. Besides the ^1H ssNMR DFT predictions span over rather broad ranges for each chemical group, while the spectrum shows well resolved signals. This is especially true for highly mobile groups like CH_3 . While molecular dynamics simulations would most definitely have improved the quality of the DFT prediction as mentioned before this was not possible. The lack of motion in the calculation might also explain the very broad distribution of the signals in general.

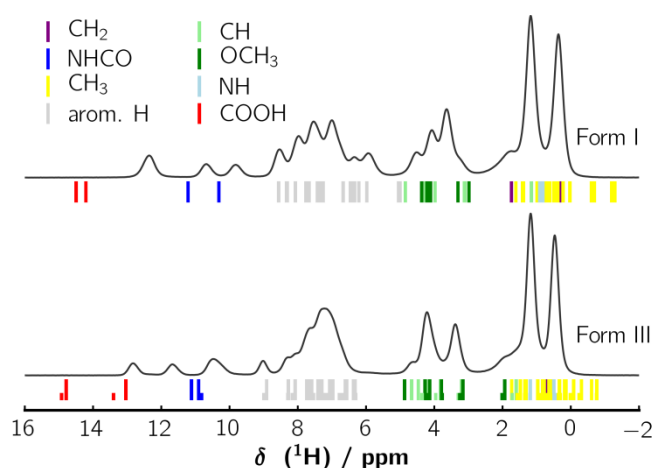


Figure 14: ^1H ssNMR spectra of form I (top) and III (bottom) with DFT simulated shifts coloured by their corresponding chemical group. Small bars below the spectrum of form III belong to the disordered structure.

As stated in chapter 1.2 the ^{13}C ssNMR for this compound mostly serves a fingerprint due to the high number of carbon atoms in the asymmetric unit. The ^{13}C ssNMR spectra and DFT predictions (Figure 15) show a number of 60 resonances predicted by DFT. Especially the lower ppm region, containing the CH_3 and CH_2 groups, shows broad regions of signals due to packing, which are averaged in the experimental spectrum due to the high mobility of the isopropane group. Furthermore, the regions between 60-70 and 110-135 ppm yield significant overlap for both experimental and simulated signals.

The C-F and C-Br signal groups both show an overestimation of the isotropic shifts. It has to be noted that calculations for carbon atoms bound to heavy elements like bromine should include relativistic effects if possible.^[120] On the other hand, the amide and acid carbon show very accurate predictions from the DFT simulation.

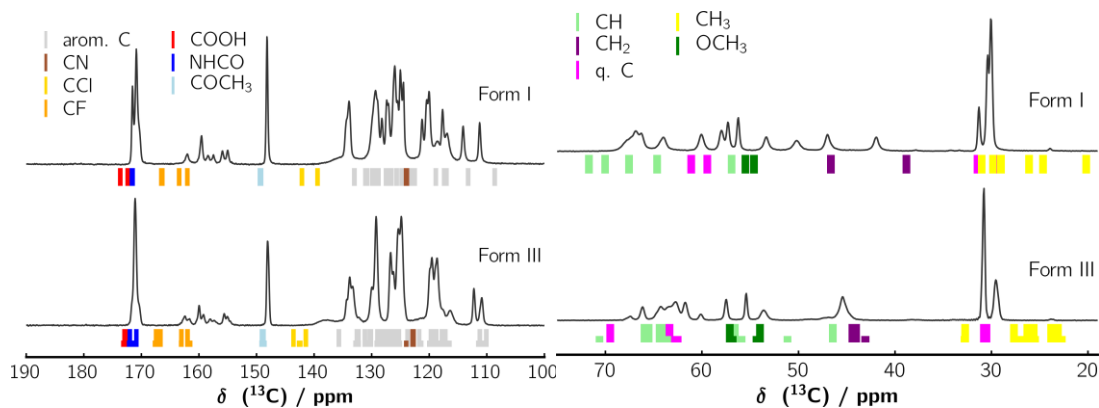


Figure 15: Low (left) and high (right) field regions of the ^{13}C ssNMR spectrum of form I and III with DFT simulated shifts coloured corresponding to their chemical group. Small bars below the spectrum of form III belong to the disordered structure.

As expected, the ^{15}N NMR spectra of Idasanutlin show three chemical groups. In the spectrum of polymorph I, the amide and secondary amine group split up noticeably due to packing effects. For modification III this splitting is smaller for the amide, as was expected considering the ^1H NMR, while the secondary amine group shows larger difference in packing. The DFT predictions for ^{15}N of form I show good agreement, while phase III does show differences in the splitting of the cyano group (Figure 16). These differences are on the other hand well within the error margin of the method and could just as well be caused by dynamic effects or by the defect structure.

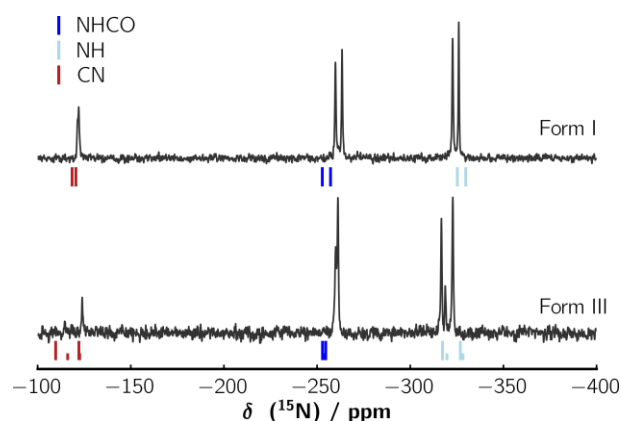


Figure 16: ^{15}N MAS ssNMR spectrum of form I and III of Idasanutlin with DFT predicted chemical shifts coloured according to their chemical groups. Small bars below the spectrum of form III belong to the disordered structure.

The ^{19}F NMR spectra show three signals for form I and a non-trivial spectrum for phase III (Figure 17). Deconvolution of the latter yields seven signals with integrals ranging from 0.08 up to 1.32. This shows the disorder within the structure, that affects one of the fluorinated benzene rings. The shift predictions, as was stated in chapter 1.2, show systematic deviations from the expected values. This is also observable for the prediction of modification I & III of Idasanutlin (Figure 17). The splitting of all signals is larger than in the experiment and it is clear that a smaller scaling factor would lead to a perfect fit of the prediction.

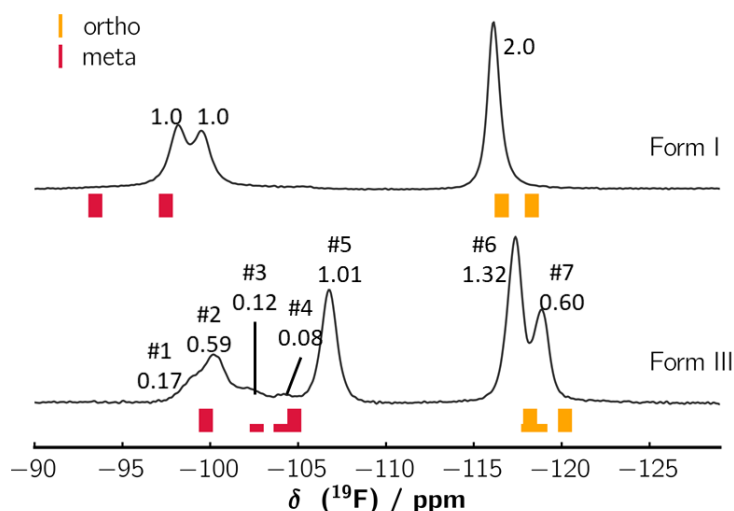


Figure 17: ^{19}F MAS ssNMR measurement of form I and III of Idasanutlin with DFT predictions coloured according to the Fluorine position on the benzene rings and integrals of the exp. signals. Small bars below the spectrum of form III belong to calculation of the disordered structure. For form III the exp- signals are numbered from highest to lowest ppm value

Still, the prediction for single different ^{19}F species is rather good, which is shown for the two calculations of the ordered and disordered substructures of polymorph III. In the ^{19}F spectrum the disordered substructure can be directly observed, and the quality of the prediction is more than good enough to assign single signals to each substructure (Figure 18 left). But the experimental spectrum shows an additional resonance when compared with the prediction. This signal can only be explained by the two substructures being in close proximity to each other, so they alter the Fluorine environment. Assuming the disorder is distributed statistically in each crystal it is possible to calculate the theoretical fraction of each of the four possible surroundings by multiplying the occupancies of both substructures (from XRD) with each other. This yields fractions of: $0.77 \times 0.77 = 0.593$; $2 \times 0.77 \times 0.23 = 0.177$ and $0.23 \times 0.23 = 0.053$ (Figure 18 right).

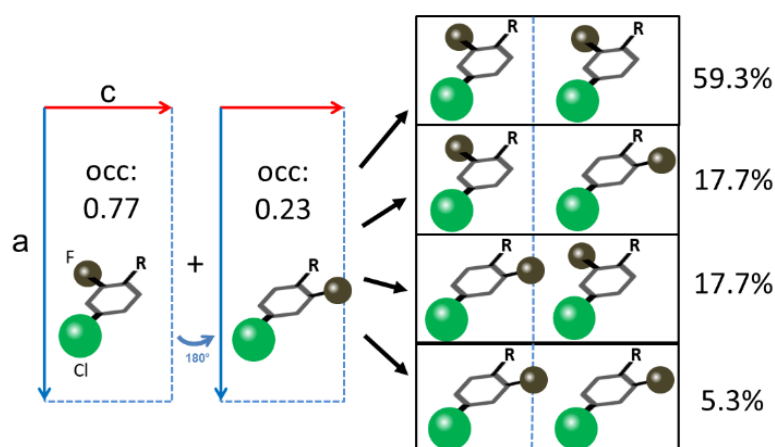


Figure 18: Schematic representation of the possible different fluorine environments due to the disorder within the structure with their percentage of the whole sample under the assumption that the disorder is distributed statistically and the occupancies from XRD are exact.

These fit the integrals in the ^{19}F ssNMR spectrum of phase III well, especially Signal #2 and #4. Due to the integral of signal #1 it is evident, that this one is probably caused by one of the ‘mixed’ structures shown on the right side in the middle of Figure 18. Since in the case of the upper middle structure the fluorine atoms point away from each other the environments they are only slightly different from the other ones. But for the lower middle structure the fluorine atoms point into the same direction the influence should be significant. Therefore, we assume that signal #1 is caused by the two fluorine atoms pointing towards each other. Due to the very short distance of these ^{19}F species, this could be proven by a very rapid build-up in the $^{19}\text{F}^{19}\text{F}$ DQSQ build-up curve of this signal.

2.3 Disorder in $\text{Na}_3[\text{Al}(\text{L-lactate})_3] \cdot 6 \text{H}_2\text{O}$

$\text{Na}_3[\text{Al}(\text{L-lactate})_3] \cdot 6 \text{H}_2\text{O}$ was crystallized from a commercial Lohtragon® AL 250 solution which is used for industrial applications like superabsorbers and cement adjuvants. The main building unit of this compound consists of aluminium complexed by three L-lactate ligands in a bidental fashion via their acid and hydroxy groups (Figure 19) forming octahedrons. Due to the unique characteristics that aluminium exhibits when being complexed by alpha-hydroxy carboxylic acids^[121] half of the hydroxy groups deprotonate to form three very short symmetric hydrogen bonds between two of these aluminium(L-lactate)₃ complexes forming a binuclear three times negatively charged $[\text{Al}(\text{L-lactate})_3]_2$ unit. The negative charge in these is mainly distributed on the sides where the carboxy groups are facing. These complexes form layers through van der Waals interactions of the methyl side chains. The negative charge is compensated by sodium which is additionally coordinated by water in the interlayer space (Figure 20).

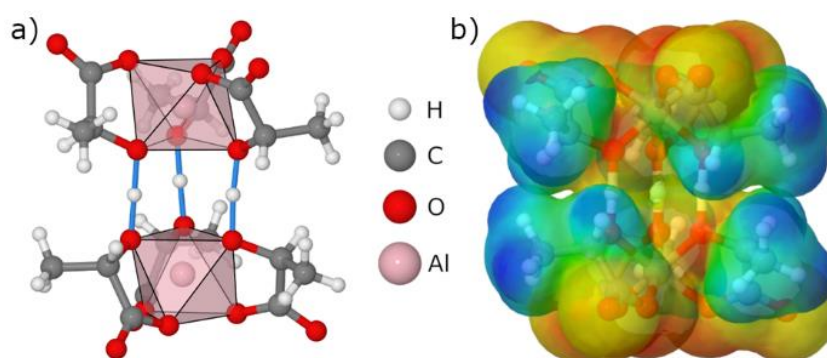


Figure 19: Bincular $[\text{Al}(\text{L-Lactate})_3]_2^{3-}$ complex with the two $\text{Al}(\text{L-Lactate})_3$ subunits being connected by three very short symmetric hydrogen bonds, depicted in blue with an O-H-O distance of 2.54 Å (a). The electrostatic potential on the 80% van-der-Waals surface of the binuclear complex with red indicating negative charge and blue being slight positive charge (b). Reprinted with permission from^[122]. Copyright 2019 American Chemical Society.

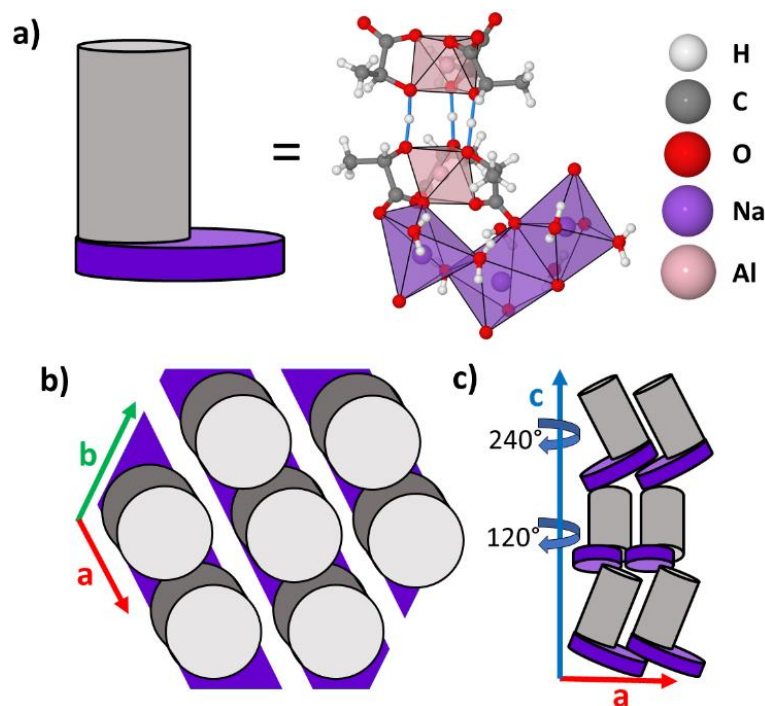


Figure 20: Packing scheme of $\text{Na}_3[\text{Al}(\text{L-lactate})_3] \cdot 6 \text{H}_2\text{O}$ with the asymmetric unit consisting of one formula unit incorporating one binuclear complex (a), the arrangement in the a/b plane (b) and their stacking along the c -axis (c). Reprinted with permission from ^[122]. Reprinted with permission from ^[122]. Copyright 2019 American Chemical Society.

In the study of $\text{Na}_3[\text{Al}(\text{L-lactate})_3]_2 \cdot 6 \text{H}_2\text{O}$ the importance of ^1H ssNMR spectra was even higher than in the previous study due to the fact that a single crystal structure solution was already carried out, fitting the XRD data very well. This structure proposal consisted of two separate $\text{Al}(\text{lactate})_3$ complexes with completely protonated OH groups. Additionally, three of the six water molecules were deprotonated, effectively forming NaOH in the interlayer space. While at the first glance this seems to make sense, it neglects the unique properties of Aluminium. When complexing Al^{3+} with alpha-hydroxy carboxylic acids not only the acid group tends to deprotonate but also the hydroxy group becomes acidic to a point where it deprotonated even at sub 7 pH values.^[121] This effect leads to the very unique structure that was found during our studies on basis of the ^1H ssNMR spectrum that was recorded of the compound. The spectrum shows typical signals for methyl, **CHOH** and a sharp signal for water (Figure 21). The latter shows smaller FWHM indicating high mobility of the H_2O molecules. While any signs of **CHOH** and **OH⁻** signals are missing, remarkably, there is a signal at 16.4 ppm which is a shift range that is rather uncommon for organic solids.^[41] In fact this high isotropic chemical shift indicates either very strong hydrogen bonding or extremely strong

acids.^[37,41] The latter could easily be ruled out by pH measurements of the parent solution which showed a value 5.5. Combining all these findings we concluded that the hydroxy groups of the two $\text{Al}(\text{L-lactate})_3$ complexes are deprotonated by $\frac{1}{2}$ leaving only water in the interlayer space. These deprotonated hydroxy groups on the other hand give rise to three very short symmetric hydrogen bonds that connect the two complexes to form a binuclear $[\text{Al}(\text{L-lactate})_3]_2^{3-}$ cluster.

The DFT calculation of this structure clearly shows the low field shifted signals which is in very good agreement with the experiment. This also indicates that the bonding is very strong rendering the influence of dynamics very small for the hydrogen bonds. Due to the sheer size of the unit cell ($c > 30 \text{ \AA}$) it was impossible to calculate molecular dynamics of this compound. Therefore for ^1H we averaged over all signals of each chemical group. Due to the relatively high amount of protons in this compound this yielded a sufficient probe of the hypersurface. This is clearly evident when looking at the averages of the calculations in comparison with the experimental signals which fit very well.

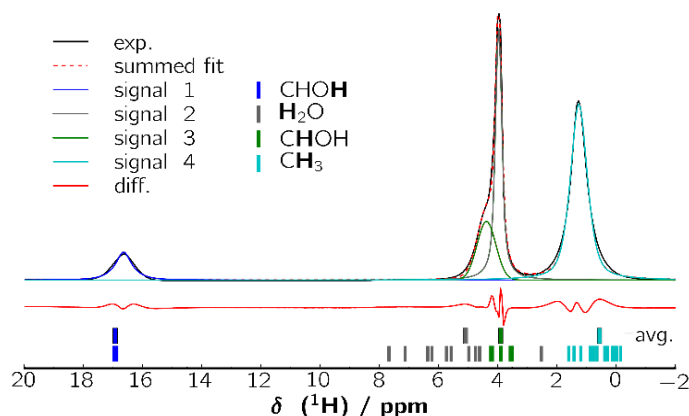


Figure 21: ^1H ssNMR spectrum of $\text{Na}_3[\text{Al}(\text{L lactate})_3]_2 * 6 \text{ H}_2\text{O}$ with deconvolution and DFT predicted values including averages (bottom bars). Reprinted with permission from ^[122]. Reprinted with permission from ^[122]. Copyright 2019 American Chemical Society.

The assignment of chemical groups for ^{13}C NMR spectroscopy is straight forward due to the limited number of carbon atoms. The DFT prediction fits the experiment very well overall, even splittings are reproduced (Figure 22), with the CHOH group showing the least and the acid group the highest splitting. These splittings on the other hand are within the error margin of the method. Additionally, the acid groups face towards the dynamically disordered sodium-water interlayer which means the simulation is only a snapshot of probably one local minimum while the spectrum shows a superposition of thermally accessible structures that can be realised within the structure.

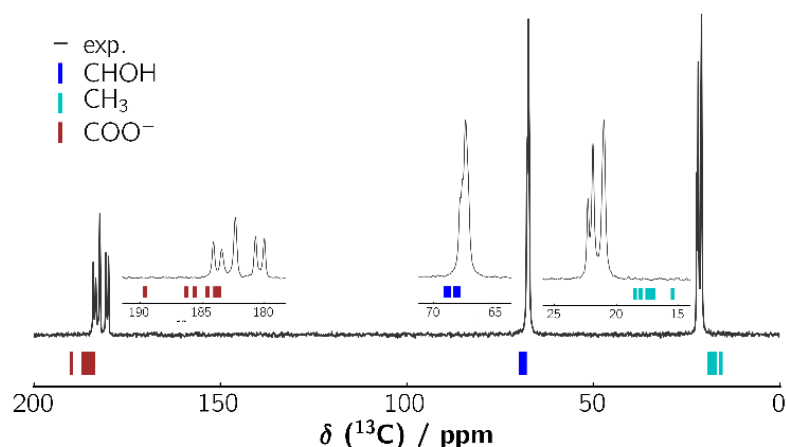


Figure 22: ^{13}C MAS ssNMR spectrum of $\text{Na}_3[\text{Al}(\text{L lactate})_3]_2 \cdot 6 \text{H}_2\text{O}$ measured at 12.5kHz with the DFT predicted chemical shifts coloured according to their chemical groups (bottom bars). Reprinted with permission from ^[122]. Reprinted with permission from ^[122]. Copyright 2019 American Chemical Society.

Due to the interlayer mobility the static ^{23}Na NMR spectrum at room temperature only shows a single resonance, while the prediction almost perfectly resembles the shape of the low temperature spectrum at 93K with its three different crystallographic sites. (Table 1, Figure 23). The comparison of the deconvolution of the experimental spectrum with the DFT predictions shows very good overall agreement, proofing that the interlayer structure is correct in terms of sodium coordination and environment.

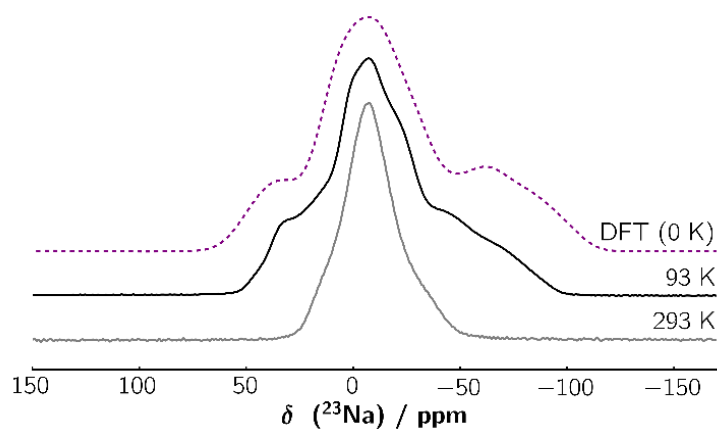


Figure 23: Static ^{23}Na ssNMR of $\text{Na}_3[\text{Al}(\text{L-lactate})_3]_2 \cdot 6 \text{H}_2\text{O}$ measured at 293 K (solid grey line) and 93 K (solid black line) and the DFT predicted spectrum (purple dashed line). Reprinted with permission from ^[122]. Reprinted with permission from ^[122]. Copyright 2019 American Chemical Society.

Table 1: Comparison of experimental ^{23}Na ssNMR parameters from deconvolution and DFT predicted ones including isotropic chemical anisotropy and quadrupolar interaction for $\text{Na}_3[\text{Al}(\text{L-lactate})_3]_2 \cdot 6 \text{H}_2\text{O}$

	Na1 exp	Na1 DFT	Na2 exp.	Na2 DFT	Na3 exp.	Na3 DFT
$\delta_{\text{iso}} / \text{ppm}$	1.35	1.83	-2.91	-1.41	3.42	1.4
$\delta_{\text{aniso}} / \text{ppm}$	10.22	10.2	5.47	5.47	8.74	-8.74
η	0.65	0.65	0.33	0.33	0.81	0.81
C_Q / MHz	2.21	-2.54	1.15	1.37	2.01	2.07
η_Q	0.25	0.26	0.60	0.60	0.76	0.77

The deconvolution of the ^{27}Al NMR spectrum yields two crystallographic sites. The prediction for $\text{Na}_3[\text{Al}(\text{L-lactate})_3]_2 \cdot 6 \text{H}_2\text{O}$ also results in two different Al sites (Figure 24) which fits both the structure and the experimental spectrum, even though both of these are part of the binuclear complex, which in itself is centrosymmetric. This points towards the interlayer space as a differentiating factor for the individual Al sites. In general, the prediction fits the experiment very well even though the quadrupolar asymmetry parameters are slightly off, which is a common problem for ^{27}Al DFT predictions. [84,95,97,98]

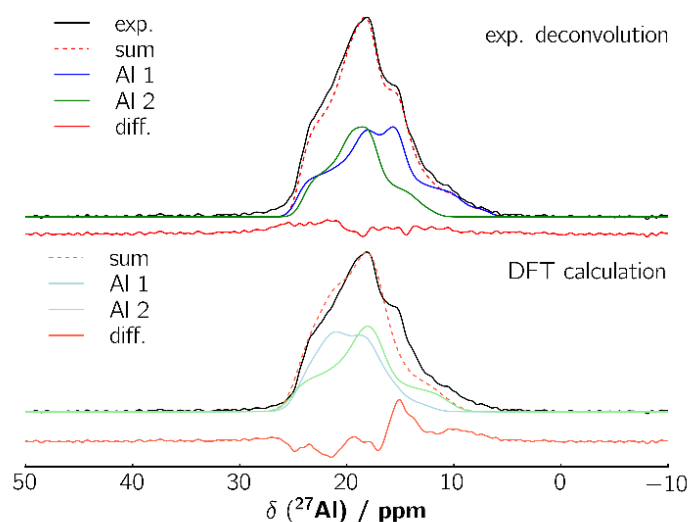


Figure 24: ^{27}Al MAS ssNMR spectrum of $\text{Na}_3[\text{Al}(\text{L-lactate})_3]_2 \cdot 6 \text{H}_2\text{O}$ with experimental deconvolution (top) and the DFT prediction (bottom) both with difference plot towards the experimental spectrum. The experimental isotropic shieldings and quadrupolar coupling constants are for Al1: $\sigma_{\text{iso}} = 24.6$, $C_q = 5.0$ MHz, $\eta_q = 0.75$ and for Al2: $\sigma_{\text{iso}} = 22.9$, $C_q = 4.6$ MHz, $\eta_q = 0.8$. The DFT predicted values are: Al1: $\sigma_{\text{iso}} = 22.9$, $C_q = 5.2$ MHz, $\eta_q = 0.5$ and Al2: $\sigma_{\text{iso}} = 24.6$, $C_q = 4.6$ MHz, $\eta_q = 0.51$. Reprinted with permission from [122]. Copyright 2019 American Chemical Society.

Additionally, we used pH dependent ^{27}Al liquid NMR spectroscopy (Figure 25) and DFT predictions for the bi- and mononuclear $\text{Al}(\text{L-lactate})_3$ (Table 2) to investigate which species is predominant in the stem solution. This relies on the findings of earlier studies, that at low pH values mononuclear $\text{Al}(\text{L-lactate})_3$ species have been observed^[123] and the fact that in solution the width of the Aluminium signals depends mainly on the quadrupolar coupling, rather than dynamic effects as ligand exchange is in the fast motion limit at room temperature.^[124] The DFT predictions for mononuclear $\text{Al}(\text{L-Lactate})_3$ species in vacuum result in a doubling of the C_Q values compared to the binuclear $[\text{Al}(\text{L-lactate})_3]_2^{3-}$. This fits the observation that for low pH values of the solution, the linewidth of the Aluminium doubles. Therefore, it is highly likely that at medium pH values the binuclear $[\text{Al}(\text{L-lactate})_3]_2^{3-}$ complex is the predominant species.

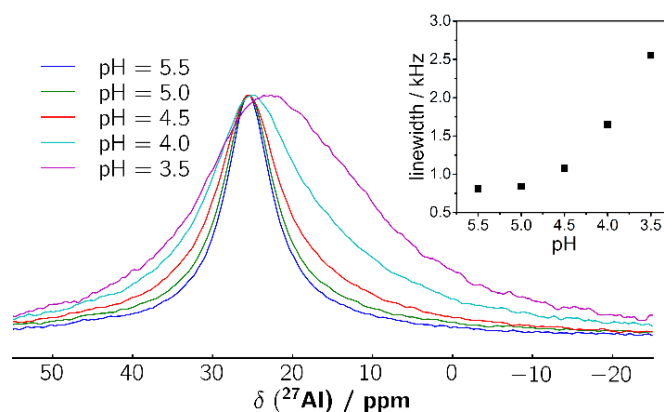


Figure 25: pH dependent ^{27}Al liquid NMR measurement of the $\text{Na}_3[\text{Al}(\text{L-lactate})_3]_2$ stem solution and the linewidth of each signal in dependence of pH. Reprinted with permission from ^[122]. Copyright 2019 American Chemical Society.

Table 2: DFT predicted isotropic chemical shift, quadrupolar coupling and quadrupolar asymmetry of several mono- and binuclear $\text{Al}(\text{L-lactate})_3$ species.

	$\text{Al}(\text{L-lactate})_3$	$\text{Al}(\text{L-lactate})_3^{1-}$	$\text{Al}(\text{L-lactate})_3^{2-}$	$[\text{Al}(\text{L-lactate})_3]_2^{3-}$
δ_{iso} ppm	/ 31.6	41.1	48.5	24.4 / 25.0
C_Q MHz	/ 11.3	-10.7	-9.6	3.8 / 3.8
η_Q	0.02	0.81	0.7	0.41 / 0.44

References

- [1] A. F. Holleman, E. Wiberg, *Holleman-Wiberg Lehrbuch Der Anorganischen Chemie*, Walter De Gruyter, **1971**.
- [2] G. Oszlányi, A. Sütő, *IUCr, Acta Crystallogr. Sect. A Found. Crystallogr.* **2004**, *60*, 134–141.
- [3] G. Oszlányi, A. Sütő, *IUCr, Acta Crystallogr. Sect. A Found. Crystallogr.* **2008**, *64*, 123–134.
- [4] P. J. M. van Laarhoven, E. H. L. Aarts, in *Simulated Annealing Theory Appl.*, **1987**, pp. 7–15.
- [5] J. Pannetier, J. Bassas-Alsina, J. Rodriguez-Carvajal, V. Caignaert, *Nature* **1990**, *346*, 343–345.
- [6] Y. G. Andreev, G. S. MacGlashan, P. G. Bruce, *Phys. Rev. B* **1997**, *55*, 12011–12017.
- [7] P. . Madhu, X. Zhao, M. H. Levitt, *Chem. Phys. Lett.* **2001**, *346*, 142–148.
- [8] X. Zhao, M. Edén, M. H. Levitt, *Chem. Phys. Lett.* **2001**, *342*, 353–361.
- [9] M. H. Levitt, in *Encycl. Magn. Reson.*, John Wiley & Sons, Ltd, **2007**.
- [10] P. E. Kristiansen, D. J. Mitchell, J. N. S. Evans, *J. Magn. Reson.* **2002**, *157*, 253–266.
- [11] C. Pickard, F. Mauri, *Phys. Rev. B* **2001**, *63*, 245101
- [12] J. R. Yates, S. E. Dobbins, C. J. Pickard, F. Mauri, P. Y. Ghi, R. K. Harris, *Phys. Chem. Chem. Phys.* **2005**, *7*, 1402.
- [13] J. Yates, C. Pickard, F. Mauri, *Phys. Rev. B* **2007**, *76*, 024401
- [14] R. P. Chapman, D. L. Bryce, *Phys. Chem. Chem. Phys.* **2009**, *11*, 6987.
- [15] C. Martineau, J. Senker, F. Taulelle, *Annu. Reports NMR Spectrosc.* **2014**, *82*, 1–57.
- [16] R. K. Harris, R. E. Wasylshen, M. J. Duer, *NMR Crystallography*, Wiley, **2009**.
- [17] L. Seyfarth, J. Senker, *Phys. Chem. Chem. Phys.* **2009**, *11*, 3522.
- [18] H. Grüninger, K. Armstrong, D. Greim, T. Boffa-Ballaran, D. J. Frost, J. Senker, *J. Am. Chem. Soc.* **2017**, *139*, 10499–10505.
- [19] W. L. Bragg, *Scientia* **1929** *23*, 45,153
- [20] T. W. Martin, T. E. Gorelik, D. Greim, C. Butterhof, U. Kolb, J. Senker, J. Breu, *CrystEngComm* **2016**, *18*,
- [21] T. Martin, D. Greim, W. Milius, M. Niedermaier, B. Ludescher, J. Von Wegerer, W. Brysch, K. Bärwinkel, J. Senker, J. Breu, *Z. Anorg Allg. Chem* **2015**, *641*,
- [22] C. Hammond, *The Basics of Crystallography and Diffraction*, International Union Of Crystallography, **1997**.
- [23] M. J. Duer, *Introduction to Solid-State NMR Spectroscopy*, Blackwell, **2004**.
- [24] M. H. Levitt, *Spin Dynamics: Basics of Nuclear Magnetic Resonance*, John Wiley & Sons, **2001**.
- [25] R. F. Moran, D. M. Dawson, S. E. Ashbrook, *Int. Rev. Phys. Chem.* **2017**, *36*, 39–115.
- [26] T. P. Jarvie, G. T. Went, K. T. Mueller, *J. Am. Chem. Soc.* **1996**, *118*, 5330–5331.
- [27] A. Watts, *Nat. Rev. Drug Discov.* **2005**, *4*, 555–568.
- [28] K. J. D. MacKenzie, M. E. Smith, *Multinuclear Solid-State NMR of Inorganic Materials*, Pergamon, **2002**.
- [29] M. Haouas, F. Taulelle, C. Martineau, *Prog. Nucl. Magn. Reson. Spectrosc.* **2016**, *94–95*, 11–36.
- [30] W. Koch, M. C. Holthausen, *A Chemist's Guide to Density Functional Theory*, John Wiley & Sons, **2015**.
- [31] B. Elena, G. Pintacuda, N. Mifsud, L. Emsley, **2006**, *128*, 29, 95559560

- [32] Bruker Analytik GmbH, *Almanac 2000*, Rheinstetten **2000**.
- [33] L. Seyfarth, J. Senker, *Phys. Chem. Chem. Phys.* **2009**, *11*, 3522.
- [34] L. Seyfarth, J. Seyfarth, B. V. Lotsch, W. Schnick, J. Senker, *Phys. Chem. Chem. Phys.* **2010**, *12*, 2227.
- [35] R. F. Moran, D. McKay, C. J. Pickard, A. J. Berry, J. M. Griffin, S. E. Ashbrook, *Phys. Chem. Chem. Phys.* **2016**, *18*, 10173–10181.
- [36] M. B. Mesch, K. Bärwinkel, Y. Krysiak, C. Martineau, F. Taulelle, R. B. Neder, U. Kolb, J. Senker, *Chem. - A Eur. J.* **2016**, *22*, 16878–16890.
- [37] T. Steiner, *Angew. Chemie Int. Ed.* **2002**, *41*, 48–76.
- [38] V. N. Staroverov, G. E. Scuseria, J. Tao, J. P. Perdew, *J. Chem. Phys.* **2003**, *119*, 12129–12137.
- [39] T. M. Alam, Z. Liao, M. Nyman, J. Yates, *J. Phys. Chem. C* **2016**, *120*, 10675–10685.
- [40] A. Bagno, F. D'Amico, G. Saielli, *ChemPhysChem* **2007**, *8*, 873–881.
- [41] M. Hesse, H. Meier, B. Zeeh, *Spektroskopische Methoden in Der Organischen Chemie*, Georg Thieme Verlag, **2005**.
- [42] C. Bonhomme, C. Gervais, F. Babonneau, C. Coelho, F. Pourpoint, T. Azaïs, S. E. Ashbrook, J. M. Griffin, J. R. Yates, F. Mauri, et al., *Chem. Rev.* **2012**, *112*, 5733–5779.
- [43] A. Bagno, F. Rastrelli, G. Saielli, *Chem. - A Eur. J.* **2006**, *12*, 5514–5525.
- [44] A. Bagno, F. Rastrelli, G. Saielli, *J. Phys. Chem. A*, **2003**, *107*, 46, 9964–9937
- [45] G. A. Olah, T. Shamma, A. Burrichter, G. Rasul, G. K. S. Prakash, *J. Am. Chem. Soc.*, **1997**, *119*, 52, 12923–12928
- [46] R. Y. Dong, A. Marini, *J. Phys. Chem. B* **2009**, *113*, 14062–14072.
- [47] T. Kupka, M. Stachów, L. Stobiński, J. Kaminský, *J. Mol. Graph. Model.* **2016**, *67*, 14–19.
- [48] H. Yang, T. Wang, D. Oehme, L. Petridis, M. Hong, J. D. Kubicki, *Cellulose* **2018**, *25*, 23–36.
- [49] P. Szczeciński, A. Gryff-Keller, S. Molchanov, *J. Org. Chem.*, **2006**, *71*, 12, 4636–4641
- [50] F. Pourpoint, J. Yehl, M. Li, R. Gupta, J. Trébosc, O. Lafon, J.-P. Amoureux, T. Polenova, *ChemPhysChem* **2015**, *16*, 1619–1626.
- [51] A. Bagno, F. Rastrelli, G. Saielli, *J. Org. Chem.*, **2007**, *72*, 19, 7373–7381
- [52] D. Kubica, A. Gryff-Keller, *J. Phys. Chem. B* **2015**, *119*, 5832–5838.
- [53] G. K. Pierens, *J. Comput. Chem.* **2014**, *35*, 1388–1394.
- [54] S. Molchanov, A. Gryff-Keller, *J. Phys. Chem. A*, **2017**, *121*, 9645–9653.
- [55] K. B. Wiberg, *J. Comput. Chem.* **1999**, *20*, 1299–1303.
- [56] E. Y. Pankratyev, A. R. Tulyabaev, L. M. Khalilov, *J. Comput. Chem.* **2011**, *32*, 1993–1997.
- [57] P. Cimino, L. Gomez-Paloma, D. Duca, R. Riccio, G. Bifulco, *Magn. Reson. Chem.* **2004**, *42*, S26–S33.
- [58] W. Migda, B. Rys, *Magn. Reson. Chem.* **2004**, *42*, 459–466.
- [59] D. Xin, C. A. Sader, O. Chaudhary, P.-J. Jones, K. Wagner, C. S. Tautermann, Z. Yang, C. A. Busacca, R. A. Saraceno, K. R. Fandrick, et al., *J. Org. Chem.* **2017**, *82*, 5135–5145.
- [60] T. Kupka, M. Stachów, M. Nieradka, J. Kaminsky, T. Pluta, *J. Chem. Theory Comput.* **2010**, *6*, 1580–1589.
- [61] K. Märker, M. Pingret, J.-M. Mouesca, D. Gasparutto, S. Hediger, G. De Paëpe, *J. Am. Chem. Soc.* **2015**, *137*, 13796–13799.
- [62] P. Cerreia Vioglio, L. Catalano, V. Vasylyeva, C. Nervi, M. R. Chierotti, G. Resnati, R. Gobetto, P. Metrangolo, *Chem. - A Eur. J.* **2016**, *22*, 16694–16694.

- [63] S. Sneddon, J. Kahr, A. F. Orsi, D. J. Price, D. M. Dawson, P. A. Wright, S. E. Ashbrook, *Solid State Nucl. Magn. Reson.* **2017**, *87*, 54–64.
- [64] P. Siudem, K. Paradowska, J. Bukowicki, *J. Mol. Struct.* **2017**, *1146*, 773–781.
- [65] J. S. Stevens, S. J. Byard, C. C. Seaton, G. Sadiq, R. J. Davey, S. L. M. Schroeder, *Phys. Chem. Chem. Phys.* **2014**, *16*, 1150–1160.
- [66] V. A. Semenov, D. O. Samultsev, L. B. Krivdin, *Magn. Reson. Chem.* **2014**, *52*, 686–693.
- [67] J. Tomasi, B. Mennucci, R. Cammi, *Chem. Rev.* **2005**, *105*, 2999–3094.
- [68] L. B. Krivdin, *Prog. Nucl. Magn. Reson. Spectrosc.* **2017**, *102–103*, 98–119.
- [69] I. Alkorta, J. Elguero, *Struct. Chem.* **2003**, *14*, 377–389.
- [70] D. O. Samultsev, V. A. Semenov, L. B. Krivdin, *Magn. Reson. Chem.* **2014**, *52*, 222–230.
- [71] T. W. Keal, D. J. Tozer, *J. Chem. Phys.* **2003**, *119*, 3015–3024.
- [72] T. W. Keal, D. J. Tozer, *J. Chem. Phys.* **2004**, *121*, 5654–5660.
- [73] C. Zehe, M. Schmidt, R. Siegel, K. Kreger, V. Daebel, S. Ganzleben, H.-W. Schmidt, J. Senker, *CrystEngComm* **2014**, *16*, 9273–9283.
- [74] J. Dabachi, M. Body, J. Dittmer, F. Fayon, C. Legein, *Dalt. Trans.* **2015**, *44*, 20675–20684.
- [75] M. Lu, S. Sarkar, M. Wang, J. Kraus, M. Fritz, C. M. Quinn, S. Bai, S. T. Holmes, C. Dybowski, G. P. A. Yap, et al., *J. Phys. Chem. B* **2018**, *122*, 6148–6155.
- [76] L. Martel, E. Capelli, M. Body, M. Klipfel, O. Beneš, L. Maksoud, P. E. Raison, E. Suard, L. Visscher, C. Bessada, et al., *Inorg. Chem.* **2018**, *57*, 15350–15360.
- [77] A. Rakhmatullin, I. B. Polovov, D. Maltsev, M. Allix, V. Volkovich, A. V. Chukin, M. Boča, C. Bessada, *Inorg. Chem.* **2018**, *57*, 1184–1195.
- [78] A. Vyalikh, L. G. Bulusheva, G. N. Chekhova, D. V. Pinakov, A. V. Okotrub, U. Scheler, *J. Phys. Chem. C* **2013**, *117*, 7940–7948.
- [79] P. M. J. Szell, S. A. Gabriel, R. D. D. Gill, S. Y. H. Wan, B. Gabidullin, D. L. Bryce, *Acta Crystallogr. Sect. C Struct. Chem.* **2017**, *73*, 157–167.
- [80] F. G. Vogt, L. M. Katrincic, S. T. Long, R. L. Mueller, R. A. Carlton, Y. T. Sun, M. N. Johnson, R. C. B. Copley, M. E. Light, *J. Pharm. Sci.* **2008**, *97*, 4756–4782.
- [81] A. J. Robbins, W. T. K. Ng, D. Jochym, T. W. Keal, S. J. Clark, D. J. Tozer, P. Hodgkinson, *Phys. Chem. Chem. Phys.* **2007**, *9*, 2389.
- [82] J. Zhang, M.-A. Pilette, F. Cuevas, T. Charpentier, F. Mauri, M. Latroche, *J. Phys. Chem. C* **2009**, *113*, 21242–21252.
- [83] M. Biswal, M. Body, C. Legein, A. Sadoc, F. Boucher, *J. Solid State Chem.* **2013**, *207*, 208–217.
- [84] A. A. Arnold, V. Terskikh, Q. Y. Li, R. Naccache, I. Marcotte, J. A. Capobianco, *J. Phys. Chem. C* **2013**, *117*, 25733–25741.
- [85] O. Socha, P. Hodgkinson, C. M. Widdifield, J. R. Yates, M. Dračinský, *J. Phys. Chem. A* **2017**, *121*, 4103–4113.
- [86] H. Koller, G. Engelhardt, A. P. M. Kentgens, J. Sauer, *J. Phys. Chem.* **1994**, *98*, 1544–1551.
- [87] E. Gambuzzi, T. Charpentier, M. C. Menziani, A. Pedone, *Chem. Phys. Lett.* **2014**, *612*, 56–61.
- [88] T. Charpentier, S. Ispas, M. Profeta, F. Mauri, C. J. Pickard, *J. Phys. Chem. B* **2004**, *108*, 4147–4161.
- [89] S. E. Ashbrook, L. Le Pollès, R. Gautier, C. J. Pickard, R. I. Walton, *Phys. Chem. Chem. Phys.* **2006**, *8*, 3423–3431.
- [90] P. Florian, E. Veron, T. F. G. Green, J. R. Yates, D. Massiot, *Chem. Mater.* **2012**, *24*, 4068–4079.
- [91] D. M. Dawson, J. M. Griffin, V. R. Seymour, P. S. Wheatley, M. Amri, T. Kurkiewicz, N. Guillou, S. Wimperis, R.

- I. Walton, S. E. Ashbrook, *J. Phys. Chem. C* **2017**, *121*, 1781–1793.
- [92] F. Suzuki, Y. Nishiyama, H. Kaji, *Chem. Phys. Lett.* **2014**, *605–606*, 1–4.
- [93] D. M. Dawson, R. I. Walton, S. Wimperis, S. E. Ashbrook, *Acta Crystallogr. Sect. C* **2017**, *73*, 191–201.
- [94] B. Zhou, B. L. Sherriff, T. Wang, *Am. Mineral.* **2009**, *94*, 865–871.
- [95] M. Choi, K. Matsunaga, F. Oba, I. Tanaka, *J. Phys. Chem. C* **2009**, *113*, 3869–3873.
- [96] A. Wong, M. E. Smith, V. Terskikh, G. Wu, *Can. J. Chem.* **2011**, *89*, 1087–1094.
- [97] S. E. Ashbrook, M. Cutajar, C. J. Pickard, R. I. Walton, S. Wimperis, *Phys. Chem. Chem. Phys.* **2008**, *10*, 5754–5764.
- [98] A. Lafond, X. Rocquefelte, M. Paris, C. Guillot-Deudon, V. Jouenne, *Chem. Mater.* **2011**, *23*, 5168–5176.
- [99] B. A. Hammann, Z. L. Ma, K. M. Wentz, M. K. Kamunde-Devonish, D. W. Johnson, S. E. Hayes, *Dalt. Trans.* **2015**, *44*, 17652–17659.
- [100] D. S. Middlemiss, F. Blanc, C. J. Pickard, C. P. Grey, *J. Magn. Reson.* **2010**, *204*, 1–10.
- [101] Y. Zhang, B. E. G. Lucier, V. V Terskikh, R. Zheng, Y. Huang, *Solid State Nucl. Magn. Reson.* **2017**, *84*, 118–131.
- [102] A. Sadoc, M. Biswal, M. Body, C. Legein, F. Boucher, D. Massiot, F. Fayon, *Solid State Nucl. Magn. Reson.* **2014**, *59–60*, 1–7.
- [103] F. Blanc, D. S. Middlemiss, L. Buannic, J. L. Palumbo, I. Farnan, C. P. Grey, *Solid State Nucl. Magn. Reson.* **2012**, *42*, 87–97.
- [104] J. Czernek, J. Brus, *Chem. Phys. Lett.* **2017**, *684*, 8–13.
- [105] T. Ohkubo, T. Okamoto, K. Kawamura, R. Guégan, K. Deguchi, S. Ohki, T. Shimizu, Y. Tachi, Y. Iwadate, *J. Phys. Chem. A* **2018**, *122*, 48, 9326–9337
- [106] D. Friedrich, D. Greim, M. Schlosser, R. Siegel, J. Senker, A. Pfitzner, *Angew. Chemie Int. Ed.* **2018**, *57*, 48, 16219–16214
- [107] R. A. Van Santen, *J. Phys. Chem.* **1984**, *88*, 5768–5769.
- [108] C. K. Perkins, E. S. Eitheim, B. L. Fulton, L. B. Fullmer, C. A. Colla, D.-H. Park, A. F. Oliveri, J. E. Hutchison, M. Nyman, W. H. Casey, et al., *Angew. Chemie* **2017**, *129*, 10295–10298.
- [109] D. L. Bryce, F. Taulelle, *Acta Cryst* **2017**, *73*, 3, 126–127
- [110] S. T. Holmes, R. W. Schurko, *J. Phys. Chem. C* **2018**, *122*, 1809–1820.
- [111] L. Rapp, B. Haberl, C. J. Pickard, J. E. Bradby, E. G. Gamaly, J. S. Williams, A. V Rode, *Nat. Commun.* **2015**, *6*, 7555.
- [112] J. Wang, B. Lukose, M. O. Thompson, P. Clancy, *J. Appl. Phys.* **2017**, *121*, 045106.
- [113] R. J. Messinger, M. Ménétrier, E. Salager, A. Boulineau, M. Duttine, D. Carlier, J.-M. Ateba Mba, L. Croguennec, C. Masquelier, D. Massiot, et al., *Chem. Mater.* **2015**, *27*, 5212–5221.
- [114] I. D. Seymour, D. S. Middlemiss, D. M. Halat, N. M. Trease, A. J. Pell, C. P. Grey, *J. Am. Chem. Soc.* **2016**, *138*, 9405–9408.
- [115] M. Paris, L. Choubrac, A. Lafond, C. Guillot-Deudon, S. Jobic, *Inorg. Chem.* **2014**, *53*, 8646–8653.
- [116] Y. J. Lee, B. Bingöl, T. Murakhtina, D. Sebastiani, W. H. Meyer, G. Wegner, H. W. Spiess, *J. Phys. Chem. B* **2007**, *111*, 9711–9721.
- [117] C. J. Pickard, R. J. Needs, *J. Phys. Condens. Matter* **2011**, *23*, 053201.
- [118] G. M. Sheldrick, IUCr, *Acta Crystallogr. Sect. A Found. Crystallogr.* **2008**, *64*, 112–122.
- [119] H. J. Deiseroth, F. S. Han, *Stud. Inorg. Chem* **1983**, *3*, 655–658.

- [120] G. Casella, A. Bagno, S. Komorovsky, M. Repisky, G. Saielli, *Chem. - A Eur. J.* **2015**, *21*, 18834–18840.
- [121] B. Corain, B. Longato, A. A. Sheikh-Osman, G. G. Bombi, C. Maccà, *J. Chem. Soc., Dalt. Trans.* **1992**, 169–172.
- [122] D. Greim, W. Milius, B. Bojer, R. Siegel, J. Breu, J. Senker, *Cryst. Growth Des.* **2019**, *19*, 4557–4563.
- [123] G. Giorgio Bombi, B. Corain, A. A. Sheikh-Osman, G. C. Valle, *Inorganica Chim. Acta* **1990**, *171*, 79–83.
- [124] A. Steigel, H. W. Spiess, *Dynamic NMR Spectroscopy*, Springer Science & Business Media, **2012**.
- [125] R. M. Martin, *Electronic Structure: Basic Theory and Practical Methods*, Cambridge University Press, **2004**.
- [126] P. W. Atkins, R. S. Friedman, *Molecular Quantum Mechanics*, Oxford University Press, **2011**.
- [127] M. Born, R. Oppenheimer, *Ann. Phys.* **1927**, *389*, 457–484.
- [128] P. Hohenberg, W. Kohn, *Phys. Rev.* **1964**, *136*, B864–B871.
- [129] W. Kohn, L. J. Sham, *Phys. Rev.* **1965**, *140*, A1133–A1138.
- [130] L. J. Sham, W. Kohn, *Phys. Rev.* **1966**, *145*, 561–567.
- [131] D. M. Ceperley, B. J. Alder, *Phys. Rev. Lett.* **1980**, *45*, 566–569.
- [132] D. Strauch, U. Rössler, *Semiconductors*, Springer **2017**.
- [133] N. Sheremetyeva, D. J. Cherniak, E. B. Watson, V. Meunier, *Phys. Chem. Miner.* **2018**, *45*, 173–184.
- [134] S. Yang, Y. Yang, M. Wu, C. Hu, W. Shen, Y. Gong, L. Huang, C. Jiang, Y. Zhang, P. M. Ajayan, *Adv. Funct. Mater.* **2018**, *28*, 1707379.
- [135] S. S. Lobanov, X. Dong, N. S. Martirosyan, A. I. Samtsevich, V. Stevanovic, P. N. Gavryushkin, K. D. Litasov, E. Greenberg, V. B. Prakapenka, A. R. Oganov, et al., *Phys. Rev. B* **2017**, *96*, 104101.
- [136] M. Zhong, Q.-J. Liu, H. Qin, Z. Jiao, F. Zhao, H.-L. Shang, F.-S. Liu, Z.-T. Liu, *Eur. Phys. J. B* **2017**, *90*, 115.
- [137] K. Panwar, S. Tiwari, N. L. Heda, *AIP Conf. Proc.* **2018**, 1942, 090032.
- [138] J. C. A. Prentice, B. Monserrat, R. J. Needs, *Phys. Rev. B* **2017**, *95*, 014108.
- [139] C. W. Murray, G. J. Laming, N. C. Handy, R. D. Amos, *Chem. Phys. Lett.* **1992**, *199*, 551–556.
- [140] F. Herman, J. P. Van Dyke, I. B. Ortenburger, *Phys. Rev. Lett.* **1969**, *22*, 807–811.
- [141] J. P. Perdew, K. Burke, *Int. J. Quantum Chem.* **1996**, *57*, 309–319.
- [142] P. S. Svendsen, U. von Barth, *Phys. Rev. B* **1996**, *54*, 17402–17413.
- [143] J. P. Perdew, K. Burke, M. Ernzerhof, *Phys. Rev. Lett.* **1996**, *77*, 3865–3868.
- [144] N. W. Ashcroft, N. D. Mermin, *Introduction to Solid State Physics*, Saunders, **1976**.
- [145] H. J. Monkhorst, J. D. Pack, *Phys. Rev. B* **1976**, *13*, 5188–5192.
- [146] M. Methfessel, A. T. Paxton, *Phys. Rev. B* **1989**, *40*, 3616–3621.
- [147] N. Troullier, J. L. Martins, *Phys. Rev. B* **1991**, *43*, 1993–2006.
- [148] D. Vanderbilt, *Phys. Rev. B* **1990**, *41*, 7892–7895.
- [149] C. G. Van de Walle, P. E. Blöchl, *Phys. Rev. B* **1993**, *47*, 4244–4255.
- [150] C. J. Pickard, F. Mauri, *Phys. Rev. B* **2001**, *63*, 245101.
- [151] J. R. Yates, C. J. Pickard, F. Mauri, *Phys. Rev. B* **2007**, *76*, 024401.
- [152] F. Mauri, B. G. Pfommer, S. G. Louie, *Phys. Rev. Lett.* **1996**, *77*, 5300–5303.

- [153] S. Kristyán, P. Pulay, *Chem. Phys. Lett.* **1994**, *229*, 175–180.
- [154] P. Hobza, J. Šponer, T. Reschel, *J. Comput. Chem.* **1995**, *16*, 1315–1325.
- [155] J. Šponer, J. Leszczynski, P. Hobza, *J. Comput. Chem.* **1996**, *17*, 841–850.
- [156] J. Pérez-Jordá, A. D. Becke, *Chem. Phys. Lett.* **1995**, *233*, 134–137.
- [157] N. Kurita, H. Sekino, *Chem. Phys. Lett.* **2001**, *348*, 139–146.
- [158] O. Couronne, Y. Ellinger, *Chem. Phys. Lett.* **1999**, *306*, 71–77.
- [159] A. D. Becke, *Phys. Rev. A* **1988**, *38*, 3098–3100.
- [160] G. Rimmler, A. Alker, M. Bosco, R. Diodone, D. Fishlock, S. Hildbrand, B. Kuhn, C. Moessner, C. Peters, P. D. Rege, et al., *Org. Process Res. Dev.* **2016**, *20*, 2057–2066.
- [161] C. Lee, W. Yang, R. G. Parr, *Phys. Rev. B* **1988**, *37*, 785–789.
- [162] A. D. Becke, *J. Chem. Phys.* **1993**, *98*, 5648–5652.
- [163] F. J. Devlin, J. W. Finley, P. J. Stephens, M. J. Frisch, *J. Phys. Chem.* **1995**, *99*, 16883–16902.
- [164] M. Dion, H. Rydberg, E. Schröder, D. C. Langreth, B. I. Lundqvist, *Phys. Rev. Lett.* **2004**, *92*, 246401.
- [165] K. Lee, É. D. Murray, L. Kong, B. I. Lundqvist, D. C. Langreth, *Phys. Rev. B* **2010**, *82*, 081101.
- [166] Y. Zhao, D. G. Truhlar, *Acc. Chem. Res.* **2008**, *41*, 157–167.
- [167] O. A. von Lilienfeld, I. Tavernelli, U. Rothlisberger, D. Sebastiani, *Phys. Rev. Lett.* **2004**, *93*, 153004.
- [168] Y. Y. Sun, Y.-H. Kim, K. Lee, S. B. Zhang, *J. Chem. Phys.* **2008**, *129*, 154102.
- [169] E. R. Johnson, I. D. Mackie, G. A. DiLabio, *J. Phys. Org. Chem.* **2009**, *22*, 1127–1135.
- [170] S. Grimme, *J. Comput. Chem.* **2006**, *27*, 1787–1799.
- [171] S. Grimme, *J. Comput. Chem.* **2004**, *25*, 1463–1473.
- [172] P. Jurečka, J. Černý, P. Hobza, D. R. Salahub, *J. Comput. Chem.* **2007**, *28*, 555–569.
- [173] S. Grimme, J. Antony, S. Ehrlich, H. Krieg, *J. Chem. Phys.* **2010**, *132*, 154104.
- [174] J.-D. Chai, M. Head-Gordon, *Phys. Chem. Chem. Phys.* **2008**, *10*, 6615.
- [175] Y. Liu, W. A. I. Goddard, *Mater. Trans.* **2009**, *50*, 1664–1670.
- [176] P. Pyykkö, M. Atsumi, *Chem. - A Eur. J.* **2009**, *15*, 186–197.
- [177] S. Grimme, A. Hansen, J. G. Brandenburg, C. Bannwarth, *Chem. Rev.* **2016**, *116*, 5105–5154.
- [178] A. Tkatchenko, M. Scheffler, *Phys. Rev. Lett.* **2009**, *102*, 073005
- [179] F. London, *Zeitschrift für Phys.* **1930**, *63*, 245–279.
- [180] F. London, *Trans. Faraday Soc.* **1937**, *33*, 8b – 26.
- [181] A. Unsöld, *Ann. Phys.* **1927**, *387*, 355–393.
- [182] A. J. Stone, *The theory of intermolecular forces*, Oxford University Press, **1996**.
- [183] F. O. Kannemann, A. D. Becke, *J. Chem. Phys.* **2012**, *136*, 034109.
- [184] X. Chu, A. Dalgarno, *J. Chem. Phys.* **2004**, *121*, 4083–4088.
- [185] F. L. Hirshfeld, *Theor. Chim. Acta* **1977**, *44*, 129–138.

3. Index of Publications

- D. Friedrich, D. Greim, M. Schlosser, R. Siegel, J. Senker, A. Pfitzner, *Angew. Chemie Int. Ed.* **2018**, *57*, 16210, DOI 10.1002/anie.201805239.
- D. Greim, A. Schmutzler, J. Thun, G. Steinfeld, G. Santiso-Quinones, R. Siegel, H. Grüninger and J. Senker (*to be submitted*)
- D. Greim, W. Milius, B. Bojer, R. Siegel, J. Breu, J. Senker, *Cryst. Growth Des.* **2019**, *19*, *8*, 4557-4563; DOI: 10.1021/acs.cgd.9b00394

4. Publications

4.1 Synthesis and Characterization of Cs₄Ga₆Q₁₁ (Q = S, Se) - Chalcogenometalates with Exotic Polymeric Anions

This work is the result of a cooperation between the Inorganic Chemistry of the University of Regensburg and the Inorganic Chemistry III of the University of Bayreuth and will be reprinted with permission from D. Friedrich, D. Greim, M. Schlosser, R. Siegel, Jürgen Senker and Arno Pfitzner, DOI: 10.1002/anie.201805239 Angew. Chemie 2018 Vol 130, 49, p. 16442-16447 Copyright 2018 Wiley-VCH

D. Friedrich and D. Greim contributed equally.

My contributions are:

- conception and main authorship of the article
- geometry optimization and calculation of NMR parameters and band structures of the two compounds using relativistic DFT+D
- modelling and calculation of defect structures of Cs₄Ga₆Se₁₁
- evaluation of both ssNMR MAS measurements and Calculations for ¹³³Cs and ⁶⁹Ga

The other authors contributions are:

- conception and main authorship of the article
- synthesis of both structures
- crystal structure solutions from Single Crystal XRD
- UV/Vis measurements and evaluation
- ¹³³Cs and ⁶⁹Ga ssNMR MAS measurements

Synthesis and Characterization of $\text{Cs}_4\text{Ga}_6\text{Q}_{11}$ ($\text{Q} = \text{S}, \text{Se}$): Chalcogenometalates with Exotic Polymeric Anions

Daniel Friedrich⁺, Dominik Greim⁺, Marc Schlosser, Renée Siegel, Jürgen Senker,^{*} and Arno Pfitzner^{*}

Dedicated to Professor Bernt Krebs on the occasion of his 80th birthday

Abstract: Two new chalcogenogallates $\text{Cs}_4\text{Ga}_6\text{Q}_{11}$ ($\text{Q} = \text{S}, \text{Se}$) were obtained by a controlled thermal treatment of CsN_3 in the presence of stoichiometric amounts of Ga_2Q_3 and the elemental chalcogens at elevated temperatures. Both isotopic compounds crystallize in the space group $\text{P}\bar{1}$ (no. 2). The most prominent structural feature in these chalcogenogallates are the complex anionic Dreier double chains ${}_{\infty}[\text{Ga}_6\text{Q}_{11}^{4-}]$ formed by condensed GaQ_4 tetrahedra. The semiconductors $\text{Cs}_4\text{Ga}_6\text{S}_{11}$ ($E_g = 3.14$ eV) and $\text{Cs}_4\text{Ga}_6\text{Se}_{11}$ ($E_g = 2.41$ eV) were further studied by using UV/Vis, ^{133}Cs and ^{71}Ga solid-state NMR spectroscopy, and complementary DFT calculations. The ^{133}Cs MAS NMR spectra are characteristic for cationic cesium and vibrational spectra show two distinct regions, attributed to the Ga–Q valence and deformation vibrations, respectively. High-temperature studies revealed incongruent melting of both solids, which is also depicted in updated binary phase-diagrams $\text{Cs}_2\text{Q}–\text{Ga}_2\text{Q}_3$ ($\text{Q} = \text{S}, \text{Se}$).

Group 13 chalcogenides are most famous for their semi-conducting properties.^[1] The combination with other elements results in multinary chalcogenides $\text{M}_x\text{T}_y\text{Q}_z$ ($\text{M} = \text{metal}$, $\text{T} = \text{Group 13 element (triel)}$, $\text{Q} = \text{chalcogen}$) with different bonding situations. Compounds containing moderately electropositive transition metals crystallize mostly in extended three-dimensional networks, while the combination with very electropositive alkali- or alkaline earth metals leads to ionic phases with polymeric anionic structures. The latter compounds are commonly referred to as chalcogenometalates. Group 13 chalcogenometalates crystallize in a large variety of different structures.^[2] The smallest building blocks in the anionic substructures of these materials are TQ_4^{5-} tetrahedra. Condensation of these tetrahedra by common corners or edges results in the formation of more complex one-, two-, or

three-dimensional anionic substructures.^[2] Usually, linkage by common edges is only possible if the central cation has a relatively low charge and if the anions are large and therefore easily polarizable. Therefore, more uncommon, exotic connectivity can be expected for the complex chalcogenotriellate anions. The binary phase diagram of the systems alkali metal–triel–chalcogen reveals that most known phases are located on the quasi-binary section $\text{M}_2\text{Q}–\text{T}_2\text{Q}_3$ (Figure 1). By analogy to similar systems, the chemical composition has a huge influence on the dimensionality of the resulting chalcogenotriellate anions.^[3]

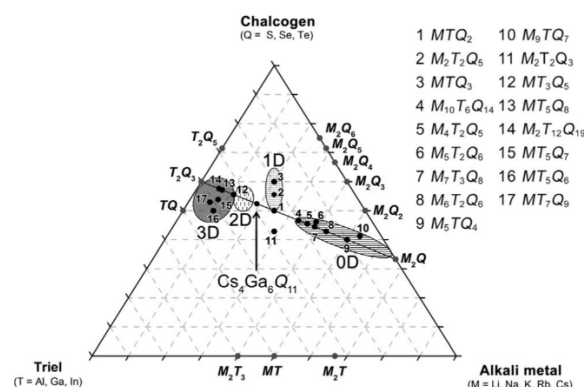


Figure 1. Ternary phase diagram of the systems alkali metal–triel–chalcogen including the known binary and ternary chalcogenides as well as the most important intermetallic phases. The quasi-binary section $\text{M}_2\text{Q}–\text{T}_2\text{Q}_3$ and the regions with different dominating dimensionalities of the anionic substructures are also depicted.

A look at the resulting crystal structures in the binary phase diagrams $\text{M}_2\text{Q}–\text{T}_2\text{Q}_3$ further clarifies this influence. Owing to the high alkali metal content in compounds with $\text{M}_2\text{Q} > 50\%$, only molecular anionic substructures with a low degree of condensation are formed. As a result of the high alkali metal content in compounds like $\text{M}_5\text{TQ}_4^{[4a-c]}$ or $\text{K}_{12}\text{In}_2\text{Se}_9$,^[4d] only isolated TQ_4^{5-} tetrahedra can be found. A decrease in the alkali metal content leads to the formation of oligomeric anions with increasing chain lengths. In compounds like $\text{M}_6\text{T}_2\text{Q}_6$,^[5] $\text{Cs}_8\text{Ga}_4\text{Se}_{10}$,^[6] and $\text{Cs}_{10}\text{Ga}_6\text{Se}_{14}$,^[7] the TQ_4^{5-} tetrahedra are connected by common corners to form dimeric, tetrameric, and hexameric anions, respectively. The high triel content in compounds with $\text{M}_2\text{Q} < 50\%$ also has an

[*] Dr. D. Friedrich,^[+] Dr. M. Schlosser, Prof. Dr. A. Pfitzner
Institut für Anorganische Chemie, Universität Regensburg
Universitätsstraße 31, 93040 Regensburg (Germany)
E-mail: arno.pfitzner@chemie.uni-regensburg.de

D. Greim,^[+] Dr. R. Siegel, Prof. Dr. J. Senker
Lehrstuhl für Anorganische Chemie III, Universität Bayreuth
95440 Bayreuth (Germany)
E-mail: juergen.senker@uni-bayreuth.de

[*] These authors contributed equally.

Supporting information (experimental section) and the ORCID identification number(s) for the author(s) of this article can be found under <https://doi.org/10.1002/anie.201805239>.

influence on the degree of condensation of the tetrahedral building blocks. The high triel content favors the formation of two- or three-dimensional structures with more complex chalcogenotrirelate anions. Besides normal-valent compounds like MT_3S_5 ($M = Rb, Cs$; $T = Ga, In$),^[8] $K_2In_{12}Se_{19}$,^[9] and MT_5Q_8 ,^[10] several mixed-valent indates exist, such as MT_3Q_6 , MIn_5S_7 ($M = K, Rb, Cs$),^[11] and MT_7Q_9 ^[12] featuring extended three-dimensional networks. The crystal structures of phases with similar elemental contents ($M_2Q \approx T_2Q_3$) feature one- or two-dimensional anionic structures with low degrees of condensation. Polymeric anionic chains can be found in $Rb_4T_2S_5$ ($T = Al, In$).^[50,13] In mixed-valent compounds like $Cs_2Ga_2Q_5$,^[14] $CsGaQ_3$ ^[15] ($Q = S, Se$) and several borates,^[16] polychalcogenide units are incorporated in the anionic chains. The compounds with a chemical composition MTQ_2 ($M_2Q = T_2Q_3$) are particularly interesting.^[17,18] These solids crystallize in several polymorphic modifications of varying dimensionality depending on the elements involved. An example for this polymorphism are the compounds $CsGaQ_2$. At high temperatures the anionic layers ${}_{\infty}^2[T_4Q_8^-]$ found in the ambient temperature modification transform to SiS_2 analogous chains ${}_{\infty}^1[TO_2^-]$.^[18] An analogous relationship between the stoichiometric composition and the resulting dimensionality of the anionic substructures is also observed in comparable systems like nitride and oxynitride silicates as well as phosphosilicates.^[19] Figure 1 also depicts the regions of differing dimensionalities observed in the anionic substructures in the systems $M_xT_yQ_z$ ($M = \text{alkali metal}$, $T = \text{triel}$, $Q = \text{chalcogen}$). These regions, however, only reflect the predominating trend as, especially in combination with small alkali metals, some exceptions are observed. On the triel-rich part of the quaternary section $M_2Q-T_2Q_3$, a large gap can be observed between the compositions MTQ_2 and MT_3Q_5 . Especially in the systems $M_2Q-Ga_2Q_3$, only few gallium rich phases have been structurally characterized. This observation leads to the assumption that more undiscovered phases with potentially exotic anionic structures could exist in the gallium rich part of the phase diagrams $M_2Q-Ga_2Q_3$. Our investigations on the synthesis and characterization of new chalcogenogallates in this less investigated region of the phase diagrams $Cs_2Q-Ga_2Q_3$ lead to the discovery of the new phases $Cs_4Ga_6Q_{11}$ ($Q = S, Se$). An analogous telluride could not be isolated to this date. The anionic substructure of the title compounds significantly differs from all previously known chain-like anions among main group chalcogenides.

The higher degree of condensation in the chalcogenogallate anions leads to the formation of double chains, which can be regarded as an intermediate between the known simple anionic chains and two-dimensional layers. Among main-group chalcogenides, such double chains are only known to exist for oxosilicates.^[20] To the best of our knowledge, similar main-group chalcogenometalates could only be stabilized using structure-directing organic cations as seen for example in $[C_{13}H_{27}N_2]_2[In_4Te_8]$ ^[21] and some selenoindates.^[22] Among transition-metal chalcogenides, only the thioferrate strands ${}_{\infty}^1[Fe_2S_3^{2-}]$ in $BaFe_2S_3$ ^[23] and $Cs_7[FeS_2]_2[Fe_2S_3]_2$ ^[24] are known.

Both title compounds $Cs_4Ga_6S_{11}$ and $Cs_4Ga_6Se_{11}$ crystallize isotypically in the triclinic space group $P\bar{1}$ with two formula units per unit cell.^[25,26] The six independent Ga sites

are tetrahedrally coordinated by the chalcogenide anions (Supporting Information, Tables S1–S6). These tetrahedra are connected amongst each other and form characteristic, anionic strands ${}_{\infty}^1[Ga_6Q_{11}^{4-}]$ ($Q = S, Se$) along $[1\bar{1}0]$. Owing to the complex connectivity in these anions, it is reasonable to split the double chains in the single chains for the discussion (Figure 2). The first chain ${}_{\infty}^1[Ga_3Q_8^{7-}]$ is formed by alternating, corner-sharing GaQ_4 and Ga_2Q_6 units, while the second chain ${}_{\infty}^1[Ga_3Q_7^{5-}]$ is composed of *trans*-corner-sharing Ga_3Q_8 units. These two single chains are connected at four common corners to form the dreier double chains ${}_{\infty}^1[Ga_6Q_{11}^{4-}]$ (in analogy to the nomenclature of silicates by F. Liebau).^[20]

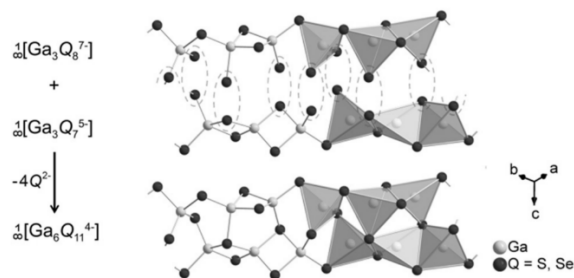


Figure 2. Condensation of the two Einer single chains to the complex, polymeric Dreier double chains in the anionic substructures of $Cs_4Ga_6Q_{11}$ ($Q = S, Se$).

The distances $Ga-Q$ are in the ranges $d(Ga-S) = 2.235(2)$ Å to $d(Ga-S) = 2.381(3)$ and $d(Ga-Se) = 2.355(2)$ Å to $d(Ga-Se) = 2.502(2)$ Å, with mean distances of $\bar{d}(Ga-S) = 2.291$ Å and $\bar{d}(Ga-Se) = 2.415$ Å. These values are only slightly smaller than the sum of the ionic radii, indicating covalent contributions to the $Ga-Q$ bonding. The angles $Q-Ga-Q$ range from $92.1(1)^\circ$ to $125.1(1)^\circ$ in $Cs_4Ga_6S_{11}$ and $92.99(5)^\circ$ to $125.54(7)^\circ$ in $Cs_4Ga_6Se_{11}$. Despite this large range, the majority of the observed angles do not deviate much from the angles in an ideal tetrahedron (Supporting Information, Tables S3, S6). Both distances and angles are in agreement to other comparable compounds.^[6,7,8a,14,15,18] Owing to the complex connectivity of the GaQ_4 tetrahedra, some distances and angles differ significantly from an ideal tetrahedron. A closer look at the structure reveals that the tetrahedron around Ga1 is the least and the tetrahedron around Ga5 is the most distorted. This is most likely because $Ga1Q_4$ is solely linked by common corners. All four crystallographic Cs sites are tenfold coordinated by the chalcogenide anions within a sphere of 5.0 Å. The distances $d(Cs-Q)$ are in the range of $d(Cs-S) = 3.427(3)$ to $d(Cs-S) = 4.796(3)$ Å and $d(Cs-Se) = 3.578(2)$ Å to $d(Cs-Se) = 4.952(2)$ Å with mean bond distances of $\bar{d}(Cs-S) = 3.789$ Å and $\bar{d}(Cs-Se) = 3.919$ Å. The Cs cations form a complex cationic substructure with $Cs-Cs$ distances in the range of $d(Cs-Cs) = 4.647(1)$ Å to $d(Cs-Cs) = 5.433(1)$ Å in $Cs_4Ga_6S_{11}$ and $d(Cs-Cs) = 4.842(2)$ Å to $d(Cs-Cs) = 5.587(2)$ Å in $Cs_4Ga_6Se_{11}$. Owing to the topology of this cationic network, a hexagonal rod packing results for the embedded chalcogenotrirelate strands. The $Cs-Cs$ distances are in good agreement with comparable compounds like

CsGa_3S_5 , CsGaQ_2 , $\text{Cs}_2\text{Ga}_2\text{Q}_5$, and CsGaQ_3 ($\text{Q} = \text{S}, \text{Se}$),^[8a,14,15,18]

The ^{133}Cs magic-angle-spinning (MAS) solid-state(ss) NMR spectra of $\text{Cs}_4\text{Ga}_6\text{S}_{11}$ and $\text{Cs}_4\text{Ga}_6\text{Se}_{11}$ show four and five resonances in the range of 240–280 ppm for $\text{Cs}_4\text{Ga}_6\text{S}_{11}$, respectively (Figure 3). The intensity ratios in the range from

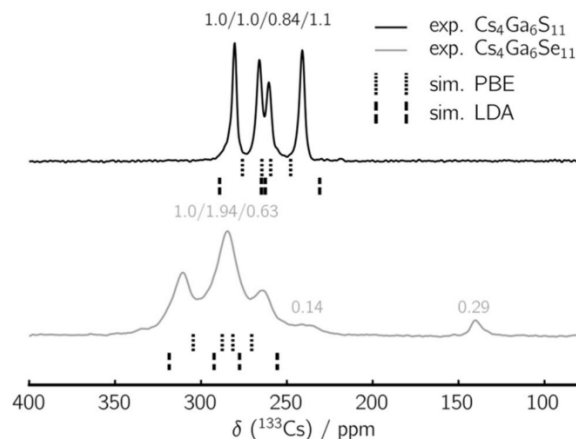


Figure 3. ^{133}Cs MAS-ss-NMR spectra of $\text{Cs}_4\text{Ga}_6\text{S}_{11}$ (20 kHz) and $\text{Cs}_4\text{Ga}_6\text{Se}_{11}$ (40 kHz). The four and three resonances and their integral convolutions (Supporting Information, Figure S1) are in good agreement with the calculated isotopic, chemical shifts of the Cs atoms using the PBE and LDA functionals.

140–310 ppm for $\text{Cs}_4\text{Ga}_6\text{S}_{11}$ are 1.0:1.0:0.84:1.1 and 1.0:1.94:0.63:0.14:0.29. Deconvolution (Supporting Information, Figure S1) of the peaks confirms that the quadrupolar coupling (C_q) of the ^{133}Cs nuclei are very small and have no influence on the peak shape. In the case of $\text{Cs}_4\text{Ga}_6\text{S}_{11}$ the number of resonances and their intensity ratios correspond to the four independent crystallographic sites of the crystal structure. The selenide, however, exhibits larger FWHM (full width at half maximum), indicating lower crystallinity of the investigated samples. The deconvolution of the two signals at 311 ppm and 285 ppm revealed three resonances with intensity ratios of 1.0:0.98:0.96 and the three remaining signals (264 ppm, 237 ppm, and 140 ppm) sum up to a relative intensity of 1.06. This is also in accordance to the four crystallographic sites with the assumption that one Cs site is shifted upfield due to defects in the anionic substructure (Supporting Information, Tables S13, S14; Figure S2).

Both new chalcogenides are direct band gap semiconductors with experimental optical band gaps of 3.14 eV for $\text{Cs}_4\text{Ga}_6\text{S}_{11}$ and 2.41 eV for $\text{Cs}_4\text{Ga}_6\text{Se}_{11}$ (Supporting Information, Figure S5). Considering the inherent uncertainties of DFT calculations (band-gap problem),^[27] these values are in good agreement with the calculations (Supporting Information, Figures S6, S7) of 3.38 eV (3.18 eV) and 2.55 eV (2.61 eV) when using the LDA(PBE) functional, respectively. Remarkably, the values for the optical band gaps of $\text{Cs}_4\text{Ga}_6\text{Q}_{11}$ ($\text{Q} = \text{S}, \text{Se}$) are between the values observed in typical one-dimensional and two-dimensional chalcogenotrirelates, which leads to the conclusion that the double chains

are an intermediate between one- and two-dimensional chalcogenogallate anions. A slightly increased degree of condensation evidently has a massive impact on the electronic properties of such low-dimensional, polymeric anions. As earlier investigations on $\text{Cs}_2\text{Ga}_2\text{Q}_5$,^[14,18c] MGAQ_2 ($\text{M} = \text{K}, \text{Rb}, \text{Cs}$; $\text{Q} = \text{S}, \text{Se}$),^[28] and analogolous aluminates^[29] already established, Ga–Q interactions in the GaQ_4 tetrahedra also cause a splitting of the electronic states to valence- and conduction band in $\text{Cs}_4\text{Ga}_6\text{Q}_{11}$ (Supporting Information, Figures S7, S6). The states above and below the Fermi energy are dominated by Ga 4s, Ga 4p, and the respective p states of the chalcogens (S 3p and Se 4p). The unoccupied Cs 6s states indicate mainly ionic bonding between Cs^+ and the chalcogenogallate anions. This observation is in line with the chemical shifts $\delta(^{133}\text{Cs})$ for both compounds, indicating a predominant ionic bonding situation, as in cesium halides such as CsCl (223.2 ppm) or CsBr (258.2 ppm).^[30] Cesium therefore does not contribute to the optical band gaps, as the highest-occupied states (Cs 5p) are located below -7 eV. In accordance to these results, the vibrational spectra of the title compounds exclusively show Ga–Q vibrations. The Raman spectra of both chalcogenogallates feature two distinct regions (Supporting Information, Figure S8), which can be attributed to Ga–Q valence (high Raman shifts) and GaC–>Q deformation vibrations or lattice vibration (lower Raman shifts), respectively.

To assign the ^{133}Cs MAS NMR resonances, additional relativistic DFT calculations were performed. As there are only a few reports on the calculation of NMR data of such heavy elements published yet, functionals using local density approximation and generalized gradient techniques were compared. The geometry-optimized structures for both functionals only differ slightly from the experimental structures (Supporting Information, Table S8). Using the PBE functional overestimates the bonding distances while using the LDA functional leads to smaller cell volumes. The Ga–Q distances in both cases (LDA and PBE); however, only deviate by one percent and the deviations of the Cs–Q distances are in the low single-digit percentage range (Supporting Information, Tables S9–S12). The calculations revealed well-resolved ^{133}Cs NMR signals for the four crystallographic sites. According to internal referencing, the maximum deviations between experiments and calculations for both compounds are below 10 ppm for both functionals (Supporting Information, Tables S13, S14). These small deviations allow for an unambiguous assignment of the experimental signals. Owing to the overall longer Cs–Q distances, calculations using the PBE functional lead to weaker splitting of the signals. Calculations using the LDA functional, however, are very close to the experimental data in both cases. The quadrupolar coupling C_q for both functionals are below 0.5 MHz for each crystallographic Cs site and therefore too weak to be resolved. For the selenide, further simulations using one and two defects per unit cell were performed (Supporting Information, Figure S2). These simulations indicate that the signals at 139 ppm and 238 ppm can be attributed to these defects. Even though the Cs4 site has the longest distances to the selenium defect site, the chemical shift δ_{iso} of this Cs site is influenced the most by

these defects. DFT calculations for all six crystallographic Ga sites led to a shift region of about 30 ppm for the ^{71}Ga chemical shifts with values of C_q between 5 and 17 MHz for both compounds (Supporting Information, Table S15). The experimental ^{71}Ga QCPMG-MAS spectra are in good agreement with these simulations (Supporting Information, Figures S3, S4, Table S15). Using magnetic fields up to 14.1 T and rotational frequencies of up to 65 kHz only allowed for four of the six Ga sites to be clearly resolved.

Thermal analysis of $\text{Cs}_4\text{Ga}_6\text{S}_{11}$ und $\text{Cs}_4\text{Ga}_6\text{Se}_{11}$ revealed thermal effects at about 700 °C for both compounds. Contrary to our initial assumptions, however, this was not the melting point of these solids. In situ analyses using high-temperature X-ray powder diffraction techniques revealed that both compounds decompose peritectically above 700 °C leading to the formation of $\text{CsGaQ}_2\text{-}m\text{C}16$ (Q = S, Se; Supporting Information, Figure S10). As the compounds $\text{Cs}_4\text{Ga}_6\text{Q}_{11}$ represent a new stoichiometric composition in the ternary systems M–T–Q, we updated the quasi-binary phase diagram $\text{Cs}_2\text{Se-Ga}_2\text{Se}_3$ published by Deiseroth in 1983^[31] and also created one for the analogous sulfide system (Supporting Information, Figure S11).

The updated phase diagrams further illustrate that more unknown phases could be discovered in the triel rich part of these systems. These compounds could potentially feature new exotic structural motifs and interesting physical properties. The analysis of $\text{Cs}_4\text{Ga}_6\text{Q}_{11}$ revealed that a minor increase in the degree of condensation already as a large impact on the electronic structure of these semiconductors. As a result, the band gaps of these double chains are in the region between the values observed for simple one-dimensional polymeric anions and anionic layers in these systems. Furthermore, the results confirm that it is possible to increase the degree of condensation in main-group chalcogenides more than usually observed. The covalent bonding character in the anionic substructures appears to be an important requirement for such an increase. Until now, only the nonlinear optical properties of some lithium chalcogenotrirelates have been studied.^[32] However, our results can be regarded as a potential strategy for the discovery of new semiconducting chalcogenides with interesting physical properties. A (partial) alkali metal substitution has no influence on the optical band gaps of these compounds as shown on our studies of $\text{Cs}_{1-x}\text{M}_x\text{GaQ}_2\text{-}m\text{C}16\text{-}m\text{C}64$ (M = K, Rb; Q = S, Se; $x = 0\text{--}1$)^[28b] solid solutions. Similar to the usage of organic cations, alkali metal substitutions have a high structure-directing potential. As the shape of the chalcogenotrirelate anions in the structures is dictated by the cationic alkali metal substructure, a controlled modification of this cationic structure by combination of different alkali metals could lead to a higher degree of condensation in the anionic structures. Especially the combination of light and heavy alkali metals could lead to the formation of more irregular one-dimensional chalcogenotrirelates. Such compounds are likely to crystallize in acentric space groups. As the optical band gaps of such materials can be controlled, these solids would especially be interesting in nonlinear optics. However, to realize these assumptions, further investigations on the controlled synthesis of such compounds are necessary.

Acknowledgements

The authors would like to thank Prof. Dr. Richard Wehrich (University of Augsburg) for fruitful discussions regarding the DFT calculations, Prof. Dr. Manfred Scheer (University of Regensburg) for the Raman measurements and Rockwood Lithium GmbH for a generous donation of cesium carbonate.

Conflict of interest

The authors declare no conflict of interest.

Keywords: azide route · chalcogenogallates · NMR spectroscopy · quantum-chemical calculations · semiconductors

How to cite: *Angew. Chem. Int. Ed.* **2018**, *57*, 16210–16214
Angew. Chem. **2018**, *130*, 16442–16447

- [1] M. Afzaal, P. O'Brien, *J. Chem. Mater.* **2006**, *16*, 1597–1602.
- [2] B. Krebs, *Angew. Chem. Int. Ed. Engl.* **1983**, *22*, 113–134; *Angew. Chem.* **1983**, *95*, 113–134.
- [3] a) A. A. Axtell, J. H. Kiao, Z. Pikramenou, M. G. Kanatzidis, *Chem. Eur. J.* **1996**, *2*, 656–666; b) J. Androulakis, S. C. Peter, H. Li, C. D. Malliakas, J. A. Peters, Z. Liu, W. Wessels, J. H. Song, H. Kin, A. J. Freeman, M. G. Kanatzidis, *Adv. Mater.* **2011**, *23*, 4163–4167.
- [4] a) B. Eisenmann, A. Hofmann, *Z. Kristallogr.* **1991**, *197*, 163–164; b) B. Eisenmann, A. Hofmann, *Z. Kristallogr.* **1991**, *197*, 169–170; c) B. Eisenmann, A. Hofmann, R. Zagler, *Z. Naturforsch. B* **1990**, *45*, 8–14; d) J. Heine, S. Dehnen, *Z. Anorg. Allg. Chem.* **2008**, *634*, 2303–2308.
- [5] a) H. J. Deiseroth, H. Fu-Son, *Z. Naturforsch. B* **1983**, *38*, 181–182; b) B. Eisenmann, A. Hofmann, *Z. Kristallogr.* **1991**, *197*, 139–140; c) B. Eisenmann, A. Hofmann, *Z. Kristallogr.* **1991**, *197*, 141–142; d) B. Eisenmann, A. Hofmann, *Z. Kristallogr.* **1991**, *197*, 143–144; e) B. Eisenmann, A. Hofmann, *Z. Kristallogr.* **1991**, *197*, 145–146; f) B. Eisenmann, A. Hofmann, *Z. Kristallogr.* **1991**, *197*, 147–148; g) B. Eisenmann, A. Hofmann, *Z. Kristallogr.* **1991**, *197*, 149–150; h) B. Eisenmann, A. Hofmann, *Z. Kristallogr.* **1991**, *197*, 151–152; i) B. Eisenmann, A. Hofmann, *Z. Kristallogr.* **1991**, *197*, 153–154; j) B. Eisenmann, A. Hofmann, *Z. Kristallogr.* **1991**, *197*, 155–156; k) B. Eisenmann, A. Hofmann, *Z. Kristallogr.* **1991**, *197*, 157–158; l) B. Eisenmann, A. Hofmann, *Z. Kristallogr.* **1991**, *197*, 161–162; m) B. Eisenmann, A. Hofmann, *Z. Kristallogr.* **1991**, *197*, 173–174; n) B. Eisenmann, A. Hofmann, *Z. Kristallogr.* **1991**, *197*, 253–254; o) H. J. Deiseroth, *Z. Naturforsch. B* **1980**, *35*, 953–958.
- [6] H. J. Deiseroth, *Z. Kristallogr.* **1984**, *166*, 283–295.
- [7] H. J. Deiseroth, H. Fu-Son, *Angew. Chem. Int. Ed. Engl.* **1981**, *20*, 962–963; *Angew. Chem.* **1981**, *93*, 1011–1012.
- [8] a) M. Schlosser, V. Frettlöh, H. J. Deiseroth, *Z. Anorg. Allg. Chem.* **2009**, *635*, 94–98; b) H. J. Deiseroth, C. Reiner, M. Schlosser, L. Kienle, *Z. Anorg. Allg. Chem.* **2002**, *628*, 1641–1647; c) H. Y. Zeng, M. J. Zhang, B. W. Liu, N. Ye, Z. Y. Zhao, F. K. Zheng, G. C. Guo, J. S. Huang, *J. Alloys Compd.* **2015**, *624*, 279–283; d) L. Kienle, V. Duppel, A. Simon, H. J. Deiseroth, *Z. Anorg. Allg. Chem.* **2003**, *629*, 443–453.
- [9] M. Schlosser, C. Reiner, H. J. Deiseroth, L. Kienle, *Eur. J. Inorg. Chem.* **2001**, 2241–2247.
- [10] a) D. Carré, M. P. Pardo, *Acta Crystallogr. Sect. C* **1983**, *39*, 822–824; b) H. J. Deiseroth, *Z. Kristallogr.* **1986**, *177*, 307–314.

- [11] H. J. Deiseroth, C. Reiner, *Z. Anorg. Allg. Chem.* **1998**, *624*, 1839–1845.
- [12] a) C. Reiner, H. J. Deiseroth, *Z. Kristallogr.* **1999**, *214*, 13; b) C. Reiner, H. J. Deiseroth, M. Schlosser, L. Kienle, *Z. Anorg. Allg. Chem.* **2002**, *628*, 249–257.
- [13] V. Winkler, M. Schlosser, A. Pflitzner, *Z. Anorg. Allg. Chem.* **2015**, *641*, 549–556.
- [14] a) D. Friedrich, M. Schlosser, A. Pflitzner, *Z. Anorg. Allg. Chem.* **2014**, *640*, 826–829; b) D. Friedrich, F. Pielhofer, M. Schlosser, R. Weihrich, A. Pflitzner, *Chem. Eur. J.* **2015**, *21*, 1811–1817.
- [15] a) M. Suseela Devi, K. Vidyasagar, *J. Chem. Doc.* **2002**, *4751*–4754; b) J. Do, M. G. Kanatzidis, *Z. Anorg. Allg. Chem.* **2003**, *629*, 621–624.
- [16] a) A. Lindemann, J. Küper, W. Hamann, J. Kuchinke, C. Köster, B. Krebs, *J. Solid State Chem.* **2001**, *157*, 206–212; b) A. Hammerschmidt, J. Küper, L. Stork, B. Krebs, *Z. Anorg. Allg. Chem.* **1994**, *620*, 1898–1904; c) A. Lindemann, J. Küper, C. Jansen, J. Kuchinke, C. Köster, A. Hammerschmidt, M. Döch, T. Pruß, B. Krebs, *Z. Anorg. Allg. Chem.* **2001**, *627*, 419–425; d) C. Püttmann, F. Hiltmann, W. Hamann, C. Brendel, B. Krebs, *Z. Anorg. Allg. Chem.* **1993**, *619*, 109–116.
- [17] a) B. Eisenmann, A. Hofmann, *Z. Kristallogr.* **1991**, *197*, 171–172; b) J. Kim, T. Hughbank, *J. Solid State Chem.* **2000**, *149*, 242–251; c) P. Lemoine, D. Carre, M. Guittard, *Acta Crystallogr. Sect. C* **1984**, *40*, 910–912; d) B. Eisenmann, A. Hofmann, *Z. Kristallogr.* **1991**, *195*, 318; e) P. Wang, X. Y. Huang, Y. L. Liu, J. Li, H. Y. Guo, *Huaxue Xuebao* **2000**, *58*, 1005–1008; f) S. J. Ewing, D. I. Woodward, A. V. Powell, P. Vaqueiro, *J. Solid State Chem.* **2013**, *204*, 159–165; g) H. Lin, J. N. Shen, L. Chen, L. M. Wu, *Inorg. Chem.* **2013**, *52*, 10726–10728; h) R. Hoppe, W. Lidecke, F. C. Frorath, *Z. Anorg. Allg. Chem.* **1961**, *309*, 49–54; i) H. J. Beister, S. Ves, W. Hönle, K. Syassen, G. Kühn, *Phys. Rev. B* **1991**, *43*, 9635–9642; j) A. Kumari, K. Vidyasagar, *Acta Crystallogr. Sect. E* **2005**, *61*, i193–i195; k) E. J. Qu, M. A. Pell, T. M. Fielberth, J. A. Ibers, *Z. Kristallogr.* **1997**, *212*, 91; l) H. Q. Zeng, F. K. Zheng, R. P. Chen, Z. C. Dong, G. C. Guo, J. S. Huang, *J. Alloys Compd.* **2007**, *432*, 69–73; m) J. Kim, T. Hughbanks, *Inorg. Chem.* **2000**, *39*, 3092–3097; n) W. Hönle, G. Kühn, H. Neumann, *Z. Anorg. Allg. Chem.* **1986**, *532*, 150–156; o) E. E. Hellstrom, R. A. Huggins, *Mater. Res. Bull.* **1979**, *14*, 881–889; p) J. Leal-Gonzalez, S. A. Melibary, A. J. Smith, *Acta Crystallogr. Sect. C* **1990**, *46*, 2017–2019; q) K. Kuriyama, T. Nozaki, *J. Appl. Phys.* **1981**, *52*, 6441–6443; r) T. Kamijoh, K. Kuriyama, *J. Cryst. Growth* **1979**, *46*, 801–803; s) W. Hönle, G. Kühn, H. Neumann, *Z. Anorg. Allg. Chem.* **1986**, *543*, 161–168; t) L. Isaenko, P. Krinitsin, V. Vedenyapin, A. Yelisseyev, A. Merkulov, J. J. Zondy, V. Petrov, *Cryst. Growth Des.* **2005**, *5*, 1325–1329.
- [18] a) D. Schmitz, W. Bronger, *Z. Naturforsch. B* **1975**, *30*, 491–493; b) D. Friedrich, M. Schlosser, A. Pflitzner, *Cryst. Growth Des.* **2016**, *16*, 3983–3992; c) D. Friedrich, M. Schlosser, R. Weihrich, A. Pflitzner, *Inorg. Chem. Front.* **2017**, *4*, 393–400.
- [19] a) M. Zeuner, S. Pagano, W. Schnick, *Angew. Chem. Int. Ed.* **2011**, *50*, 7754–7775; *Angew. Chem.* **2011**, *123*, 7898–7920; b) H. Eickhoff, L. Toffoletti, W. Klein, G. Raudaschl-Sieber, T. Fässler, *Inorg. Chem.* **2017**, *56*, 6688–6694; c) D. Johrendt, A. Haffner, A. K. Hatz, I. Moudrakovski, B. V. Lotsch, *Angew. Chem. Int. Ed.* **2018**, *57*, 6155–6160; *Angew. Chem.* **2018**, *130*, 6263–6268.
- [20] F. Liebau in *Structural Chemistry of Silicates*, Springer, Heidelberg, New York, Tokyo, **1985**.
- [21] J. Heine, S. Santer, S. Dehnen, *Inorg. Chem.* **2013**, *52*, 4424–4430.
- [22] a) P. Vaqueiro, *Inorg. Chem.* **2006**, *45*, 4150–4156; b) P. Vaqueiro, M. L. Romero, *Acta Crystallogr. Sect. E* **2007**, *63*, m1700; c) P. Vaqueiro, *J. Solid State Chem.* **2006**, *179*, 302–307; d) J. Zhou, G. Q. Bian, Y. Zhand, Q. Y. Zhu, C. Y. Li, J. Dai, *Inorg. Chem.* **2007**, *46*, 6347–6352; e) H. G. Yao, M. Ji, S. H. Ji, Y. L. An, *Z. Anorg. Allg. Chem.* **2012**, *638*, 683–687; f) X. Zhang, Z. X. Lei, W. Luo, W. Q. Mu, X. Zhang, Q. Y. Zhu, J. Dai, *Inorg. Chem.* **2011**, *50*, 10872–10877; g) S. J. Ewing, P. Vaqueiro, *J. Chem. Soc. Dalton Trans.* **2015**, *44*, 1592–1600.
- [23] H. Y. Hong, H. Steinfink, *J. Solid State Sci.* **1972**, *5*, 93–104.
- [24] M. Schwarz, C. Röhr, *Z. Anorg. Allg. Chem.* **2015**, *641*, 1053–1060.
- [25] For details on the single-crystal structure determination of Cs₄Ga₆S₁₁, see the Supporting Information. Details on the crystal structure of Cs₄Ga₆S₁₁ (.cif file) can be obtained at the Fachinformationszentrum Karlsruhe, 76344 Eggenstein-Leopoldshafen, Deutschland (+49)7247–808-666; E-mail: crysdata@fiz-karlsruhe.de) upon quoting the number CSD-434534.
- [26] For details on the single-crystal structure determination of Cs₄Ga₆Se₁₁, see the Supporting Information. Details on the crystal structure of Cs₄Ga₆Se₁₁ (.cif file) can be obtained at the Fachinformationszentrum Karlsruhe, 76344 Eggenstein-Leopoldshafen, Deutschland (+49)7247–808-666; E-mail: crysdata@fiz-karlsruhe.de) upon quoting the number CSD-434535.
- [27] D. Bagayoko, *AIP Adv.* **2014**, *4*, 127104.
- [28] a) K. Feng, D. Mei, L. Bai, Z. Lin, J. Yao, Y. Wu, *Solid State Sci.* **2012**, *14*, 1152–1156; b) D. Friedrich, M. Schlosser, M. Etter, A. Pflitzner, *Crystals* **2017**, *7*, 379.
- [29] A. Benmakhlouf, A. Bentabet, A. Bouhemadou, S. Mabed, R. Khenata, S. Bin-Omran, *Solid State Sci.* **2015**, *48*, 72–81.
- [30] K. J. D. MacKenzie, M. E. Smith in *Multinuclear Solid-State Nuclear Magnetic Resonance of Inorganic Materials*, Pergamon, Oxford, **2002**.
- [31] H. J. Deiseroth, F. S. Han, *Stud. Inorg. Chem.* **1983**, *18*, 655–658.
- [32] a) L. Isaenko, A. Yelisseyev, S. Lobanov, A. Titov, V. Prtrov, J.-J. Zondy, P. Krinitsin, M. Merkulov, V. Vedenyapin, J. Smirnova, *Cryst. Res. Technol.* **2003**, *38*, 379–387; b) J.-J. Zondy, F. Bielsa, A. Douillet, L. Hilico, O. Acef, V. Petrov, A. Yelisseyev, L. Isaenko, P. Krinitsin, *Opt. Lett.* **2007**, *32*, 1722–1724; c) A. H. Reshak, S. Auluck, I. V. Kityk, Y. Al-Douri, R. Khenata, A. Bouhemadou, *Appl. Phys. A* **2009**, *94*, 315–320.

Manuscript received: May 4, 2018

Accepted manuscript online: August 30, 2018

Version of record online: November 11, 2018



Supporting Information

Synthesis and Characterization of $\text{Cs}_4\text{Ga}_6\text{Q}_{11}$ (Q = S, Se): Chalcogenometalates with Exotic Polymeric Anions

Daniel Friedrich⁺, Dominik Greim⁺, Marc Schlosser, Renée Siegel, Jürgen Senker, and Arno Pfitzner**

anie_201805239_sm_miscellaneous_information.pdf

Inhaltsangabe**Experimentelles**

Tabelle S1. Atomkoordinaten und isotrope Auslenkungsparameter $U_{eq}/\text{\AA}^2$ von $\text{Cs}_4\text{Ga}_6\text{S}_{11}$ (20 °C).

Tabelle S2. Anisotrope Auslenkungsparameter $U_{ij}/\text{\AA}^2$ von $\text{Cs}_4\text{Ga}_6\text{S}_{11}$ (20 °C).

Tabelle S3. Ausgewählte interatomare Abstände und Winkel in $\text{Cs}_4\text{Ga}_6\text{S}_{11}$ (20 °C).

Tabelle S4. Atomkoordinaten und isotrope Auslenkungsparameter $U_{eq}/\text{\AA}^2$ von $\text{Cs}_4\text{Ga}_6\text{Se}_{11}$ (20 °C).

Tabelle S5. Anisotrope Auslenkungsparameter $U_{ij}/\text{\AA}^2$ von $\text{Cs}_4\text{Ga}_6\text{Se}_{11}$ (20 °C).

Tabelle S6. Ausgewählte interatomare Abstände und Winkel in $\text{Cs}_4\text{Ga}_6\text{Se}_{11}$ (20 °C).

Abbildung S1. Entfaltung des ^{133}Cs MAS-FK-NMR Spektrum von $\text{Cs}_4\text{Ga}_6\text{S}_{11}$ und $\text{Cs}_4\text{Ga}_6\text{Se}_{11}$.

Tabelle S7. Parameter der DFT Berechnungen mit Hilfe von CASTEP-8.0.

Tabelle S8. Zellkonstanten von $\text{Cs}_4\text{Ga}_6\text{S}_{11}$ und $\text{Cs}_4\text{Ga}_6\text{Se}_{11}$ nach Geometrieoptimierung mit Hilfe von DFT.

Tabelle S9. Chemische Verschiebung der experimentellen Spektren der DFT Simulationen unter Verwendung des PBE und des LDA Funktionals mit absoluten Abweichungen.

Tabelle S10. Parameter der DFT Berechnungen mit Hilfe von CASTEP-8.0.

Abbildung S2. UV/Vis Spektren von $\text{Cs}_4\text{Ga}_6\text{Q}_{11}$ ($Q = \text{S, Se}$).

Abbildung S3. Bandstrukturen und DOS mit den Beiträgen der jeweiligen Elemente von $\text{Cs}_4\text{Ga}_6\text{S}_{11}$ berechnet mit LDA (oben) und PBE (unten).

Abbildung S4. Bandstrukturen und DOS mit den Beiträgen der jeweiligen Elemente von $\text{Cs}_4\text{Ga}_6\text{Se}_{11}$ berechnet mit LDA (oben) und PBE (unten).

Abbildung S5. Raman-Spektren von $\text{Cs}_4\text{Ga}_6\text{S}_{11}$ und $\text{Cs}_4\text{Ga}_6\text{Se}_{11}$ im Bereich von 50 – 500 cm^{-1} .

Abbildung S6. ^{133}Cs MAS NMR Spektrum von $\text{Cs}_4\text{Ga}_6\text{Se}_{11}$ mit per DFT berechneten Werten der chemischen Verschiebungen für die Funktionale PBE und LDA für die ursprüngliche Struktur und Strukturen mit einem bzw. zwei Defekten pro Elementarzelle.

Abbildung S7. Verlauf der Röntgen-Pulverdiffraktogramme von $\text{Cs}_4\text{Ga}_6\text{S}_{11}$ und $\text{Cs}_4\text{Ga}_6\text{Se}_{11}$ im Temperaturbereich von 25 – 800 °C.

Abbildung S8. Binäre Phasendiagramme der Systeme $\text{Cs}_2\text{S} - \text{Ga}_2\text{S}_3$ (oben) und $\text{Cs}_2\text{Se} - \text{Ga}_2\text{Se}_3$ (unten).

Abbildung S9. Röntgen-Pulverdiffraktogramme von $\text{Cs}_4\text{Ga}_6\text{S}_{11}$ und $\text{Cs}_4\text{Ga}_6\text{Se}_{11}$.

Tabelle S11. Verfeinerte Zellparameter von $\text{Cs}_4\text{Ga}_6\text{S}_{11}$ und $\text{Cs}_4\text{Ga}_6\text{Se}_{11}$.

Experimentelles

Die Darstellung von $\text{Cs}_4\text{Ga}_6\text{S}_{11}$ und $\text{Cs}_4\text{Ga}_6\text{Se}_{11}$ erfolgt durch langsame thermische Zersetzung ($0.5\text{ }^\circ\text{C}/\text{min}$, 0.3 g Ansatzgröße) von CsN_3 in Gegenwart stöchiometrischer Mengen eines Galliumchalkogenids (Ga_2S_3 , GaSe) und elementarem Chalkogen. Um eine unkontrollierte, explosive Reaktion zu vermeiden, erfolgte die Zersetzung des Azids langsam am dynamischen Vakuum, wobei frei werdender Stickstoff abgezogen wurde. Im Anschluss an die Zersetzung wurden die inhomogenen Rohprodukte in evakuierten Quarzglasampullen mehrere Tage bei $680\text{ }^\circ\text{C}$, also knapp unterhalb der peritektischen Zersetzungstemperatur, getempert. Zur Bestimmung der Kristallstrukturen wurden Röntgen-Einkristallstrukturuntersuchungen an einem Vierkreis-Diffraktometer (Rigaku Supernova, $\text{Mo-K}\alpha$, $\lambda = 0.71073\text{ \AA}$, $20\text{ }^\circ\text{C}$) durchgeführt. Die Lösung der Kristallstrukturen der Titelverbindungen erfolgte mittels charge flipping Algorithmen mit dem Programm Superflip,^[31] implementiert in Jana2006^[32]. Die finalen Strukturverfeinerungen nach der Methode der kleinsten Fehlerquadrate gegen F^2 (volle Matrix) mit Hilfe des Programms Jana2006^[32] konvergierten bei $R_1 = 4.85\text{ \%}$ für $\text{Cs}_4\text{Ga}_6\text{S}_{11}$ und $R_1 = 4.09\text{ \%}$ (alle Daten) für $\text{Cs}_4\text{Ga}_6\text{Se}_{11}$.

Pulverdiffraktogramme der Chalkogenogallate wurden an einem STOE Stadi P Pulverdiffraktometer mit monochromatisierter $\text{Cu-K}\alpha_1$ Strahlung ($\lambda = 1.540598\text{ \AA}$) und einem Dectris Mythen 1K Detektor aufgenommen (vgl. Abbildung S9, Tabelle S11). Zur Aufnahme der Diffraktogramme bei hohen Temperaturen wurde ein STOE Kapillarofen 0.65 (Heizrate $10\text{ }^\circ\text{C}/\text{min}$, Temperaturinkrement $10\text{ }^\circ\text{C}$, 5 min Wartezeit vor jeder Messung) und monochromatisierte $\text{Mo-K}\alpha_1$ Strahlung ($\lambda = 0.70930\text{ \AA}$) genutzt. Die Messung der fein kristallinen Proben erfolgte in Quarzglaskapillaren (Innendurchmesser 0.3 mm) in Debye-Scherrer Geometrie. Zur Steuerung des Diffraktometers und zur Auswertung der Diffraktogramme wurde das WinX^{POW} Softwarepaket von STOE & Cie genutzt.^[33]

Die ^{133}Cs -MAS-NMR Spektren wurden an einem Bruker Avance-III HD Spektrometer bei einem B_0 Feld von 9.4 T aufgenommen und auf eine $0.1\text{ M Cs}(\text{NO}_3)$ -Lsg. referenziert. Dabei wurde nach einem 10° Flipwinkelpuls mit einer Dauer von $1\text{ }\mu\text{s}$ bei einer Rotationsfrequenz von 40 kHz mit Hilfe eines kommerziell erhältlichen Bruker 1.9 mm MAS Tripelresonanzprobenkopfes ($\text{Cs}_4\text{Ga}_6\text{Se}_{11}$) und bei einer Rotationsfrequenz von 20 kHz mit Hilfe eines 3.2 mm MAS Tripelresonanzprobenkopfes ($\text{Cs}_4\text{Ga}_6\text{S}_{11}$) gemessen. Für beide lag die Relaxationszeit bei 60 s . Die DFT-Simulationen wurden mit Hilfe des Programmpakets CASTEP 8.0 durchgeführt (vgl. Tabelle S9).^[34] Die Berechnung der NMR-Parameter erfolgte mit Hilfe des GIPAW Ansatzes.^[35] Die Referenzierung der Werte der chemischen Abschirmung erfolgte auf die jeweilige experimentelle Messung. Als relativistische Korrektur kam für alle Berechnungen die zeroth order regular approximation (zora) zum Einsatz.

Die Messung der optischen Bandlücken erfolgte mittels diffuser Reflexionsspektroskopie an einem Omega 20 Spektrometer der Firma Bruins Instruments mit BaSO_4 als Weißstandard. Die Absorptionsspektren wurden unter Zuhilfenahme einer modifizierten Kubelka-Munk Funktion berechnet.^[36]

Tabelle S1. Atomkoordinaten und isotrope Auslenkungsparameter $U_{eq}/\text{\AA}^2$ von $\text{Cs}_4\text{Ga}_6\text{S}_{11}$ (20 °C).

Atom	Wyck.	Sof.	x	y	z	U_{eq}^a
Cs1	2i	1	0.6921(1)	0.4628(1)	0.1150(1)	0.0300(1)
Cs2	2i	1	0.2295(1)	0.0407(1)	0.0514(1)	0.0312(1)
Cs3	2i	1	0.3051(1)	0.4743(1)	0.4383(1)	0.0338(1)
Cs4	2i	1	0.9028(1)	0.0187(1)	0.3694(1)	0.0336(1)
Ga1	2i	1	0.5929(1)	0.0727(1)	0.1812(1)	0.0170(2)
Ga2	2i	1	0.0170(1)	0.2517(1)	0.8163(1)	0.0185(3)
Ga3	2i	1	0.2366(1)	0.4267(1)	0.1494(1)	0.0185(3)
Ga4	2i	1	0.4075(1)	0.2724(1)	0.6924(1)	0.0178(3)
Ga5	2i	1	0.0624(1)	0.5829(1)	0.6647(1)	0.0166(2)
Ga6	2i	1	0.2912(1)	0.1107(1)	0.3525(1)	0.0177(2)
S1	2i	1	0.4667(1)	0.2691(1)	0.0710(1)	0.0226(6)
S2	2i	1	0.8648(1)	0.0196(1)	0.1470(1)	0.0218(6)
S3	2i	1	0.2509(1)	0.6084(1)	0.2116(1)	0.0263(6)
S4	2i	1	0.0051(1)	0.6033(1)	0.0855(1)	0.0232(6)
S5	2i	1	0.5121(1)	0.1554(1)	0.3113(1)	0.0212(6)
S6	2i	1	0.4476(1)	0.1395(1)	0.8261(1)	0.0209(6)
S7	2i	1	0.1451(1)	0.3076(1)	0.6761(1)	0.0174(6)
S8	2i	1	0.1302(1)	0.2503(1)	0.2373(1)	0.0180(6)
S9	2i	1	0.6350(1)	0.1553(1)	0.5972(1)	0.0256(6)
S10	2i	1	0.6801(1)	0.4513(1)	0.3371(1)	0.0215(6)
S11	2i	1	0.0784(1)	0.2629(1)	0.4481(1)	0.0215(6)

^a U_{eq} ist definiert als ein Drittel der Spur des orthogonalisierten U_{ij} Tensors.

Tabelle S2. Anisotrope Auslenkungsparameter $U_{ij}/\text{\AA}^2$ von $\text{Cs}_4\text{Ga}_6\text{S}_{11}$ (20 °C).

Atom	U_{11}	U_{22}	U_{33}	U_{23}	U_{13}	U_{12}
Cs1	0.0344(2)	0.0255(2)	0.0288(2)	-0.0128(1)	-0.0060(1)	-0.0028(1)
Cs2	0.0209(2)	0.0389(2)	0.0281(2)	-0.0077(1)	-0.0047(1)	-0.0082(1)
Cs3	0.0293(2)	0.0385(2)	0.0376(3)	-0.0182(1)	0.0074(1)	-0.0181(1)
Cs4	0.0411(2)	0.0260(2)	0.0387(3)	-0.0187(1)	-0.0192(2)	0.0066(1)
Ga1	0.0133(3)	0.0138(3)	0.0188(4)	-0.0029(2)	-0.0018(2)	-0.0020(2d)
Ga2	0.0148(3)	0.0143(3)	0.0208(4)	-0.0024(2)	-0.0027(3)	-0.0028(2)
Ga3	0.0143(3)	0.0152(3)	0.0197(4)	-0.0024(2)	-0.0016(3)	-0.0029(2)
Ga4	0.0141(3)	0.0122(3)	0.0213(4)	-0.0028(2)	-0.0023(3)	-0.0002(2)
Ga5	0.0130(3)	0.0125(3)	0.0193(4)	-0.0026(2)	-0.0021(2)	-0.0012(2)
Ga6	0.0131(3)	0.0135(3)	0.0201(4)	-0.0023(2)	-0.0011(2)	-0.0017(2)
S1	0.0178(6)	0.0176(6)	0.0184(8)	0.0009(5)	-0.0011(6)	-0.0012(6)
S2	0.0147(6)	0.0147(6)	0.0297(9)	-0.0041(5)	-0.0008(6)	-0.0008(6)
S3	0.0174(7)	0.0242(7)	0.0352(1)	-0.0053(6)	-0.0064(7)	-0.0082(7)
S4	0.0212(7)	0.0192(7)	0.0231(9)	-0.0017(6)	-0.0085(6)	-0.0050(6)
S5	0.0157(6)	0.0262(7)	0.0222(8)	-0.0085(6)	-0.0007(6)	-0.0091(6)
S6	0.0227(7)	0.0162(6)	0.0231(8)	-0.0077(5)	-0.0086(6)	0.0004(6)
S7	0.0175(6)	0.0135(6)	0.0192(8)	-0.0053(5)	-0.0029(6)	-0.0029(5)
S8	0.0160(6)	0.0153(6)	0.0179(8)	-0.0039(5)	-0.0012(6)	-0.0031(5)
S9	0.0214(7)	0.0142(6)	0.0290(9)	-0.0031(5)	0.0041(6)	-0.0017(6)
S10	0.0147(6)	0.0134(6)	0.0320(9)	-0.0046(5)	-0.0021(6)	-0.0012(6)
S11	0.0173(6)	0.0187(7)	0.0155(8)	0.0001(5)	-0.0010(6)	-0.0010(6)

Tabelle S3. Ausgewählte interatomare Abstände und Winkel in Cs₄Ga₆S₁₁ (20 °C).

Abstand /Å		Abstand /Å		Winkel /°	
Ga1-S1	2.286(2)	Cs1-S1	3.661(4)	S1-Ga1-S2	103.5(1)
Ga1-S2	2.297(3)	Cs1-S1 ⁱ	3.509(2)	S1-Ga1-S5	115.2(1)
Ga1-S5	2.269(3)	Cs1-S2	3.636(3)	S1-Ga1-S6	104.1(1)
Ga1-S6	2.276(4)	Cs1-S3	3.703(3)	S2-Ga1-S5	104.8(1)
Ga2-S2	2.237(3)	Cs1-S4 ⁱⁱ	3.657(4)	S2-Ga1-S6	113.6(1)
Ga2-S3	2.276(3)	Cs1-S4 ⁱ	3.722(2)	S5-Ga1-S6	115.2(1)
Ga2-S4	2.270(3)	Cs1-S5	4.390(3)	S2-Ga2-S3	119.7(1)
Ga2-S7	2.381(3)	Cs1-S6 ^{iv}	3.631(3)	S2-Ga2-S4	116.4(1)
Ga3-S1	2.235(2)	Cs1-S8 ⁱⁱ	4.288(3)	S2-Ga2-S7	106.9(1)
Ga3-S3	2.278(4)	Cs1-S10	3.535(3)	S3-Ga2-S4	98.8(1)
Ga3-S4	2.281(1)	Cs2-S1	3.888(4)	S3-Ga2-S7	98.0(1)
Ga3-S8	2.381(3)	Cs2-S1 ⁱⁱⁱ	3.546(2)	S4-Ga2-S7	116.0(1)
Ga4-S6	2.239(3)	Cs2-S2 ^v	3.469(3)	S1-Ga3-S3	116.7(1)
Ga4-S7	2.377(3)	Cs2-S2 ⁱⁱⁱ	3.759(3)	S1-Ga3-S4	119.6(1)
Ga4-S9	2.268(2)	Cs2-S3 ^{viii}	4.247(3)	S1-Ga3-S8	106.1(1)
Ga4-S10	2.295(3)	Cs2-S4	4.796(3)	S3-Ga3-S4	98.4(1)
Ga5-S7	2.310(3)	Cs2-S4 ^{ix}	3.507(2)	S3-Ga3-S8	118.3(1)
Ga5-S8	2.321(2)	Cs2-S6 ^{vi}	3.866(2)	S4-Ga3-S8	96.6(1)
Ga5-S10	2.263(3)	Cs2-S6 ^{vii}	3.454(3)	S6-Ga4-S7	104.4(1)
Ga5-S11	2.265(3)	Cs2-S8	3.695(3)	S6-Ga4-S9	111.5(1)
Ga6-S5	2.239(3)	Cs3-S3	3.628(3)	S6-Ga4-S10	119.9(1)
Ga6-S8	2.375(3)	Cs3-S5	3.539(3)	S7-Ga4-S9	121.1(1)
Ga6-S9	2.259(3)	Cs3-S7	4.023(2)	S7-Ga4-S10	92.3(1)
Ga6-S11	2.302(2)	Cs3-S7 ^x	4.293(3)	S9-Ga4-S10	107.1(1)
		Cs3-S9	3.971(2)	S7-Ga5-S8	125.1(1)
Ga1-Ga2	3.425(1)	Cs3-S9 ^{iv}	3.708(3)	S7-Ga5-S10	94.9(1)
Ga1-Ga3	3.401(1)	Cs3-S10	3.427(3)	S7-Ga5-S11	113.3(1)
Ga1-Ga4	3.425(2)	Cs3-S10 ^{iv}	3.908(3)	S8-Ga5-S10	111.7(1)
Ga1-Ga6	3.418(2)	Cs3-S11	3.520(4)	S8-Ga5-S11	94.6(1)
Ga2-Ga3	2.885(1)	Cs3-S11 ^x	3.573(2)	S10-Ga5-S11	119.4(1)
Ga2-Ga4	3.817(2)	Cs4-S2	3.679(3)	S5-Ga6-S8	104.4(1)
Ga2-Ga5	3.631(2)	Cs4-S3 ^{xii}	4.554(3)	S5-Ga6-S9	112.0(1)
Ga3-Ga5	3.621(2)	Cs4-S5	3.487(3)	S5-Ga6-S11	118.9(1)
Ga3-Ga6	3.821(2)	Cs4-S7 ^{vii}	3.608(3)	S8-Ga6-S9	120.7(1)
Ga4-Ga5	3.152(1)	Cs4-S8 ⁱⁱ	3.742(3)	S8-Ga6-S11	92.1(1)
Ga4-Ga6	3.458(2)	Cs4-S9	4.048(3)	S9-Ga6-S11	108.0(1)
Ga5-Ga6	3.166(1)	Cs4-S9 ^{xi}	3.886(3)		
		Cs4-S10	3.531(2)		
		Cs4-S11 ⁱⁱ	3.982(4)		
		Cs4-S11 ^{vii}	3.439(2)		
Cs1-Cs1 ⁱ	5.433(1)	Cs2-Cs4 ^v	5.345(1)		
Cs1-Cs2 ^{xiii}	5.289(1)	Cs3-Cs3 ^x	5.406(1)		
Cs1-Cs2 ⁱⁱ	4.697(1)	Cs3-Cs3 ^{iv}	4.783(1)		
Cs1-Cs2 ⁱ	5.114(1)	Cs3-Cs4 ^{xv}	4.694(1)		
Cs1-Cs4	5.061(1)	Cs3-Cs4	5.189(1)		
Cs2-Cs2 ^{xiv}	5.385(1)	Cs4-Cs4 ^{xi}	4.825(1)		
Cs2-Cs2 ⁱⁱⁱ	4.647(1)				

^aSymmetriecodes zur Darstellung äquivalenter Atome: (i) -x+1,-y+1,-z; (ii) x+1,y,z; (iii) -x+1,-y,-z; (iv) -x+1,-y+1,-z+1; (v) x-1,y,z; (vi) x,y,z-1; (vii) -x+1,-y,-z+1; (viii) x,y-1,z; (ix) -x,-y+1,-z; (x) -x,-y+1,-z+1; (xi) -x+2,-y,-z+1; (xii) x+1,y-1,z; (xiii) x,y+1,z; (xiv) -x,-y,-z; (xv) x-1,y+1,z.

Tabelle S4. Atomkoordinaten und isotrope Auslenkungsparameter (in $U_{eq}/\text{\AA}^2$) von $\text{Cs}_4\text{Ga}_6\text{Se}_{11}$ (20 °C).

Atom	Wyck.	Sof.	x	y	z	U_{eq}^a
Cs1	2i	1	0.69244(6)	0.45974(6)	0.11401(3)	0.0317(2)
Cs2	2i	1	0.22847(5)	0.04505(6)	0.04771(3)	0.0335(2)
Cs3	2i	1	0.30594(6)	0.46894(6)	0.44355(3)	0.0376(3)
Cs4	2i	1	0.91325(6)	0.01698(6)	0.36703(3)	0.0361(3)
Ga1	2i	1	0.59352(8)	0.07057(8)	0.18130(5)	0.0177(3)
Ga2	2i	1	0.01348(8)	0.25290(9)	0.81595(5)	0.0197(3)
Ga3	2i	1	0.23820(8)	0.42520(9)	0.14972(5)	0.0198(3)
Ga4	2i	1	0.40837(8)	0.27591(8)	0.69259(5)	0.0187(3)
Ga5	2i	1	0.06258(8)	0.58561(8)	0.66453(5)	0.0165(3)
Ga6	2i	1	0.29166(8)	0.10815(8)	0.35380(5)	0.0186(3)
Se1	2i	1	0.46920(8)	0.26775(8)	0.06787(4)	0.0236(3)
Se2	2i	1	0.86808(8)	0.02180(8)	0.14610(5)	0.0225(3)
Se3	2i	0.929(2)	0.25649(9)	0.60787(9)	0.21438(5)	0.0255(4)
Se4	2i	1	0.00431(8)	0.60032(8)	0.08387(5)	0.0247(3)
Se5	2i	1	0.51679(8)	0.15357(9)	0.31416(5)	0.0234(3)
Se6	2i	1	0.45121(8)	0.14240(8)	0.82902(5)	0.0219(3)
Se7	2i	1	0.14514(8)	0.30689(8)	0.67410(4)	0.0187(3)
Se8	2i	1	0.13078(8)	0.24465(8)	0.23577(4)	0.0186(3)
Se9	2i	1	0.63725(8)	0.16050(8)	0.59450(5)	0.0276(3)
Se10	2i	1	0.67720(8)	0.44507(8)	0.33606(5)	0.0220(3)
Se11	2i	1	0.07687(8)	0.26116(8)	0.45182(4)	0.0220(3)
Se3'	2i	0.071	0.344(2)	0.477(3)	0.247(1)	0.020(5)
Se3''	2i	0.071	0.230(3)	0.754(2)	0.203(1)	0.034(5)

^a U_{eq} ist definiert als ein Drittel der Spur des orthogonalisierten U_{ij} Tensors.

Tabelle S5. Anisotrope Auslenkungsparameter $U_{ij}/\text{\AA}^2$ von $\text{Cs}_4\text{Ga}_6\text{Se}_{11}$ (20 °C).

Atom	U_{11}	U_{22}	U_{33}	U_{23}	U_{13}	U_{12}
Cs1	0.0376(3)	0.0277(3)	0.0313(3)	-0.0161(2)	-0.0055(2)	-0.0034(2)
Cs2	0.0219(2)	0.0458(3)	0.0294(3)	-0.0104(2)	-0.0043(2)	-0.0100(2)
Cs3	0.0324(3)	0.0448(3)	0.0441(3)	-0.0239(2)	0.0109(2)	-0.0224(3)
Cs4	0.0454(3)	0.0299(3)	0.0435(3)	-0.0248(2)	-0.0210(3)	0.0080(2)
Ga1	0.0146(4)	0.0157(4)	0.0210(4)	-0.0065(3)	-0.0013(3)	-0.0017(3)
Ga2	0.0160(4)	0.0180(4)	0.0230(5)	-0.0059(3)	-0.0025(3)	-0.0037(3)
Ga3	0.0154(4)	0.0194(4)	0.0219(4)	-0.0059(3)	-0.0009(3)	-0.0046(3)
Ga4	0.0163(4)	0.0148(4)	0.0228(4)	-0.0064(3)	-0.0022(3)	-0.0009(3)
Ga5	0.0142(3)	0.0140(4)	0.0197(4)	-0.0059(3)	-0.0008(3)	-0.0022(3)
Ga6	0.0149(4)	0.0165(4)	0.0220(4)	-0.0063(3)	0.0006(3)	-0.0033(3)
Se1	0.0192(3)	0.0206(4)	0.0192(4)	-0.0026(3)	0.0007(3)	-0.0002(3)
Se2	0.0159(3)	0.0168(4)	0.0332(5)	-0.0086(3)	0.0001(3)	-0.0014(3)
Se3	0.0159(4)	0.0261(5)	0.0361(5)	-0.0075(4)	-0.0056(4)	-0.0106(4)
Se4	0.0244(4)	0.0213(4)	0.0250(4)	-0.0053(3)	-0.0071(3)	-0.0056(3)
Se5	0.0187(3)	0.0314(4)	0.0243(4)	-0.0136(3)	0.0005(3)	-0.0097(3)
Se6	0.0248(4)	0.0205(4)	0.0238(4)	-0.0119(3)	-0.0088(3)	-0.0005(3)
Se7	0.0197(3)	0.0166(4)	0.0222(4)	-0.0101(3)	-0.0024(3)	-0.0032(3)
Se8	0.0178(3)	0.0195(4)	0.0180(4)	-0.0083(3)	0.0002(3)	-0.0045(3)
Se9	0.0238(4)	0.0174(4)	0.0316(5)	-0.0070(3)	0.0069(3)	-0.0013(3)
Se10	0.0152(3)	0.0158(4)	0.0350(5)	-0.0084(3)	-0.0020(3)	-0.0016(3)
Se11	0.0193(3)	0.0220(4)	0.0174(4)	-0.0049(3)	-0.0002(3)	-0.0028(3)
Se3'	0.021(5)	0.019(6)	0.026(6)	-0.012(5)	-0.006(4)	-0.006(4)
Se3''	0.025(6)	0.009(5)	0.078(10)	-0.013(4)	-0.031(6)	0.010(5)

Tabelle S6. Ausgewählte interatomare Abstände und Winkel in Cs₄Ga₆Se₁₁ (20 °C).

Abstand /Å		Abstand /Å		Winkel /°	
Ga1-Se1	2.422(1)	Cs1-Se1	3.784(1)	Se1-Ga1-Se2	102.32(4)
Ga1-Se2	2.420(1)	Cs1-Se1 ⁱ	3.630(1)	Se1-Ga1-Se5	116.18(4)
Ga1-Se5	2.387(1)	Cs1-Se2	3.751(1)	Se1-Ga1-Se6	103.35(5)
Ga1-Se6	2.396(1)	Cs1-Se3	3.848(1)	Se2-Ga1-Se5	103.98(5)
Ga2-Se2	2.362(1)	Cs1-Se4 ⁱⁱ	3.797(1)	Se2-Ga1-Se6	114.45(4)
Ga2-Se3	2.403(1)	Cs1-Se4 ⁱ	3.854(1)	Se5-Ga1-Se6	116.09(4)
Ga2-Se4	2.391(1)	Cs1-Se5	4.584(1)	Se2-Ga2-Se3	119.74(5)
Ga2-Se7	2.505(1)	Cs1-Se6 ^{iv}	3.761(1)	Se2-Ga2-Se4	116.01(4)
Ga3-Se1	2.357(1)	Cs1-Se8 ⁱⁱ	4.451(1)	Se2-Ga2-Se7	106.88(3)
Ga3-Se3	2.403(2)	Cs1-Se10	3.660(1)	Se3-Ga2-Se4	99.63(4)
Ga3-Se4	2.401(1)	Cs2-Se1	4.014(1)	Se3-Ga2-Se7	97.76(4)
Ga3-Se8	2.506(1)	Cs2-Se1 ⁱⁱⁱ	3.654(1)	Se4-Ga2-Se7	115.77(5)
Ga4-Se6	2.369(1)	Cs2-Se2 ^v	3.609(1)	Se1-Ga3-Se3	116.74(5)
Ga4-Se7	2.502(1)	Cs2-Se2 ⁱⁱⁱ	3.849(1)	Se1-Ga3-Se4	118.19(4)
Ga4-Se9	2.391(1)	Cs2-Se3 ^{viii}	4.482(1)	Se1-Ga3-Se8	105.73(4)
Ga4-Se10	2.420(1)	Cs2-Se4	4.957(1)	Se3-Ga3-Se4	99.32(4)
Ga5-Se7	2.441(1)	Cs2-Se4 ^{ix}	3.626(1)	Se3-Ga3-Se8	119.36(4)
Ga5-Se8	2.444(1)	Cs2-Se6 ^{vi}	3.981(1)	Se4-Ga3-Se8	96.21(4)
Ga5-Se10	2.390(1)	Cs2-Se6 ^{vii}	3.581(1)	Se6-Ga4-Se7	105.11(4)
Ga5-Se11	2.392(1)	Cs2-Se8	3.803(1)	Se6-Ga4-Se9	111.79(3)
Ga6-Se5	2.362(1)	Cs3-Se3	3.816(1)	Se6-Ga4-Se10	119.64(5)
Ga6-Se8	2.499(1)	Cs3-Se5	3.685(1)	Se7-Ga4-Se9	120.28(5)
Ga6-Se9	2.384(1)	Cs3-Se7	4.093(1)	Se7-Ga4-Se10	93.21(3)
Ga6-Se11	2.428(1)	Cs3-Se7 ^x	4.507(1)	Se9-Ga4-Se10	106.34(4)
		Cs3-Se9	4.063(1)	Se7-Ga5-Se8	125.58(4)
Ga1-Ga2	3.593(1)	Cs3-Se9 ^{iv}	3.852(1)	Se7-Ga5-Se10	95.51(3)
Ga1-Ga3	3.556(1)	Cs3-Se10	3.570(1)	Se7-Ga5-Se11	112.65(5)
Ga1-Ga4	3.584(1)	Cs3-Se10 ^{iv}	4.030(1)	Se8-Ga5-Se10	111.09(5)
Ga1-Ga6	3.567(1)	Cs3-Se11	3.653(1)	Se8-Ga5-Se11	95.12(3)
Ga2-Ga3	3.015(1)	Cs3-Se11 ^x	3.691(1)	Se10-Ga5-Se11	118.83(4)
Ga2-Ga4	4.011(1)	Cs4-Se2	3.809(1)	Se5-Ga6-Se8	105.21(4)
Ga2-Ga5	3.814(1)	Cs4-Se3 ^{xiii}	4.681(1)	Se5-Ga6-Se9	111.96(4)
Ga3-Ga5	3.781(1)	Cs4-Se5	3.648(1)	Se5-Ga6-Se11	118.81(5)
Ga3-Ga6	3.996(1)	Cs4-Se7 ^{vii}	3.743(1)	Se8-Ga6-Se9	120.31(5)
Ga4-Ga5	3.300(1)	Cs4-Se8 ⁱⁱ	3.818(1)	Se8-Ga6-Se11	92.84(3)
Ga4-Ga6	3.620(1)	Cs4-Se9	4.240(1)	Se9-Ga6-Se11	107.05(4)
Ga5-Ga6	3.314(1)	Cs4-Se9 ^{xi}	3.974(1)		
		Cs4-Se10	3.673(1)		
Se3 ⁺ -Se3 ⁺⁺	2.388(1)	Cs4-Se11 ⁱⁱ	4.086(1)		
		Cs4-Se11 ^{vii}	3.569(1)		
Cs1-Cs1 ⁱ	5.587(1)	Cs2-Cs4 ^v	5.555(1)		
Cs1-Cs2 ^{xiii}	5.372(1)	Cs3-Cs3 ^x	5.583(1)		
Cs1-Cs2 ⁱⁱ	4.888(1)	Cs3-Cs3 ^{iv}	4.909(1)		
Cs1-Cs2 ⁱ	5.329(1)	Cs3-Cs4 ^{xv}	4.935(1)		
Cs1-Cs4	5.287(1)	Cs3-Cs4	5.479(1)		
Cs2-Cs2 ^{xiv}	5.538(1)	Cs4-Cs4 ^{xi}	4.988(1)		
Cs2-Cs2 ⁱⁱⁱ	4.842(1)				

^aSymmetriecodes zur Darstellung äquivalenter Atome: (i) -x+1,-y+1,-z; (ii) x+1,y,z; (iii) -x+1,-y,-z; (iv) -x+1,-y+1,-z+1; (v) x-1,y,z; (vi) x,y,z-1; (vii) -x+1,-y,-z+1; (viii) x,y-1,z; (ix) -x,-y+1,-z; (x) -x,-y+1,-z+1; (xi) -x+2,-y,-z+1; (xii) x+1,y-1,z; (xiii) x,y+1,z; (xiv) -x,-y,-z; (xv) x-1,y+1,z.

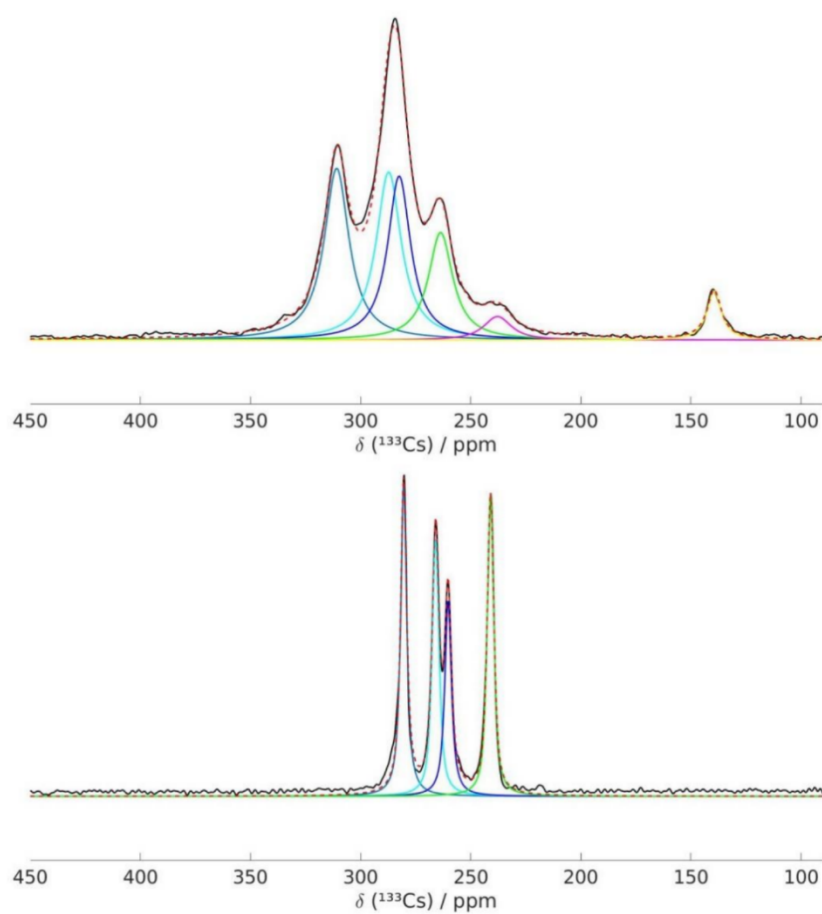


Abbildung S1. Die Entfaltung des ^{133}Cs MAS NMR Spektrums von $\text{Cs}_4\text{Ga}_6\text{Se}_{11}$ (oben) und $\text{Cs}_4\text{Ga}_6\text{S}_{11}$ (unten), zeigen vier Signale bei 310.8, 287.2, 282.5 und 263.7 ppm mit einem Intensitätsverhältnis von 1.00 / 0.98 / 0.96 / 0.63 ($\text{Cs}_4\text{Ga}_6\text{Se}_{11}$) respektive vier Signale bei 280.4, 265.9, 260.3 und 241.0 ppm mit einem Intensitätsverhältnis von 1.10 / 1.00 / 0.84 / 1.07. Die zusätzlichen Resonanzen bei 237.8 und 139.5 ppm mit Intensitäten von 0.14 und 0.29 im Spektrum von $\text{Cs}_4\text{Ga}_6\text{Se}_{11}$ (oben) deuten auf Fehlordnung einer Cäsiumlage hin.

Tabelle S7. Parameter für die Fits der ^{133}Cs MAS NMR Spektren von $\text{Cs}_4\text{Ga}_6\text{S}_{11}$ und $\text{Cs}_4\text{Ga}_6\text{Se}_{11}$. Zuordnung zu den einzelnen Lagen gemäß DFT-Rechnungen (vgl. Tabelle S9).

$\text{Cs}_4\text{Ga}_6\text{S}_{11}$	$\delta_{\text{iso}} / \text{ppm}$	FWHM / ppm	Relative Integrale	Zuordnung
1	280.41	3.2	1.10	Cs1
2	265.93	3.8	1.00	Cs2
3	260.25	3.6	0.84	Cs4
4	240.98	3.6	1.07	Cs3
$\text{Cs}_4\text{Ga}_6\text{Se}_{11}$	$\delta_{\text{iso}} / \text{ppm}$	FWHM / ppm	Relative Integrale	Zuordnung
1	310.83	13.6	1.00	Cs1
2	287.21	13.7	0.98	Cs2
3	282.46	12.5	0.96	Cs4
4	263.67	13.32	0.63	Cs3
5	237.81	15.0	0.14	-
6	139.46	7.8	0.29	Verunreinigung

Tabelle S8. Zellkonstanten von $\text{Cs}_4\text{Ga}_6\text{Se}_{11}$ und $\text{Cs}_4\text{Ga}_6\text{S}_{11}$ nach Geometrieoptimierung mit Hilfe der DFT und prozentuale Abweichungen von den Röntgen-Einkristalldaten.

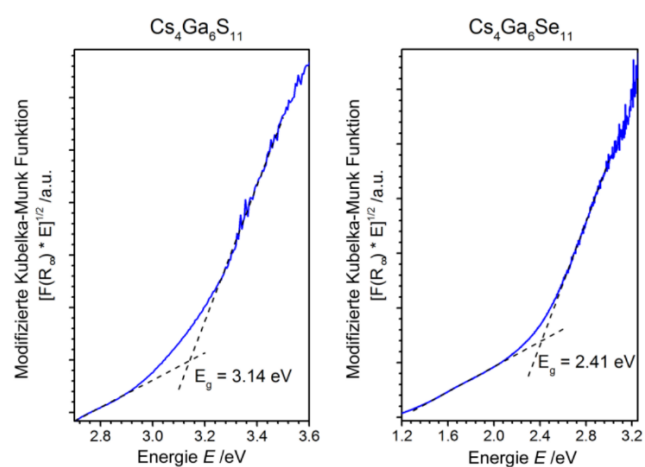
	$\text{Cs}_4\text{Ga}_6\text{S}_{11}$				$\text{Cs}_4\text{Ga}_6\text{Se}_{11}$			
	LDA	%	PBE	%	LDA	%	PBE	%
$a / \text{Å}$	9.129	-2.2	9.599	+2.8	9.471	-2.3	9.978	+2.9
$b / \text{Å}$	9.303	-.2	9.842	+3.4	9.624	-2.5	10.190	+3.2
$c / \text{Å}$	15.748	-2.6	16.724	+3.4	16.257	-3.0	17.317	+3.3
$\alpha / ^\circ$	76.44	+0.7	75.424	-0.6	77.219	+1.0	76.091	-0.5
$\beta / ^\circ$	77.12	+0.5	76.435	-0.3	77.652	+0.7	76.892	-0.3
$\gamma / ^\circ$	61.07	+1.0	59.354	-1.8	61.731	+1.3	60.026	-1.5
$V / \text{Å}^3$	1128.37	-6.2	1304.77	+8.1	1262.45	-6.7	1468.64	+8.2

Tabelle S9. Chemische Verschiebungen δ_{iso} der experimentellen Spektren der DFT Simulationen unter Verwendung des PBE und des LDA Funktionals mit absoluten Abweichungen.

Signal $\text{Cs}_4\text{Ga}_6\text{S}_{11}$	Cs1	Cs2	Cs3	Cs4	St.Abw.
$\delta_{\text{iso}} \text{ exp.} / \text{ppm}$	280.41	265.93	240.98	260.25	
$\delta_{\text{iso}} \text{ calc. PBE} / \text{ppm}$	275.82	264.51	247.82	259.42	4.85
$\Delta_{\text{PBE}} / \text{ppm}$	4.59	1.42	-6.84	0.83	
$\delta_{\text{iso}} \text{ calc. LDA} / \text{ppm}$	289.17	264.84	231.01	262.58	7.81
$\Delta_{\text{LDA}} / \text{ppm}$	-8.76	1.09	9.97	-2.33	
Signal $\text{Cs}_4\text{Ga}_6\text{Se}_{11}$	Cs1	Cs2	Cs3	Cs4	
$\delta_{\text{iso}} \text{ exp.} / \text{ppm}$	310.83	287.21	263.67	282.46	
$\delta_{\text{iso}} \text{ calc. PBE} / \text{ppm}$	304.61	287.63	270.45	281.51	5.35
$\Delta_{\text{PBE}} / \text{ppm}$	6.22	-0.42	-6.78	0.95	
$\delta_{\text{iso}} \text{ calc. LDA} / \text{ppm}$	318.48	292.36	255.61	277.71	7.58
$\Delta_{\text{LDA}} / \text{ppm}$	-7.65	-5.15	8.06	4.75	

Tabelle S10. Parameter der DFT Berechnungen mit Hilfe von CASTEP-8.0.

Cutoff-Energie	800 eV
k-Punkt Raster	0.05 \AA^{-1}
F_{\max}	0.2 eV \AA^{-1}
E_{\max}	$2 \cdot 10^{-5}$ eV/Atom
P_{\max}	0.1 GPa
Relativistische Korrektur	ZORA
$\delta_{\text{ref}}(\text{PBE}, \text{Cs}_4\text{Ga}_6\text{S}_{11})$	5934.23 ppm
$\delta_{\text{ref}}(\text{PBE}, \text{Cs}_4\text{Ga}_6\text{Se}_{11})$	5933.98 ppm
$\delta_{\text{ref}}(\text{LDA}, \text{Cs}_4\text{Ga}_6\text{S}_{11})$	5633.47 ppm
$\delta_{\text{ref}}(\text{LDA}, \text{Cs}_4\text{Ga}_6\text{Se}_{11})$	5625.71 ppm

**Abbildung S2.** UV/vis Spektren von $\text{Cs}_4\text{Ga}_6\text{Q}_{11}$ ($Q = \text{S}, \text{Se}$). Die Bandlücken wurden durch Extrapolation des abfallenden Teils der Kubelka-Munk Funktion auf die Grundlinie ermittelt (gestrichelte Linien).

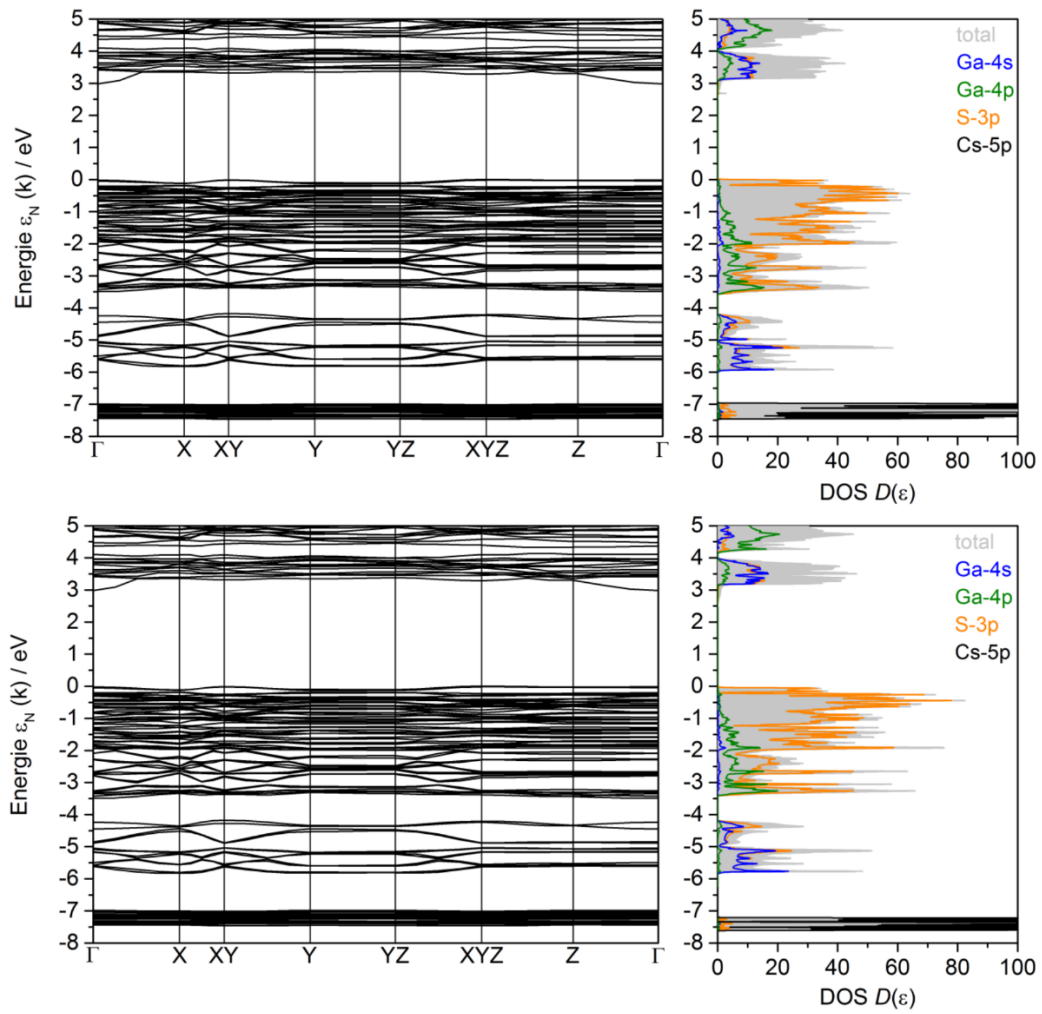


Abbildung S3. Bandstrukturen und DOS mit den Beiträgen der jeweiligen Elemente von $\text{Cs}_4\text{Ga}_6\text{S}_{11}$ berechnet mit LDA (oben) und PBE (unten).

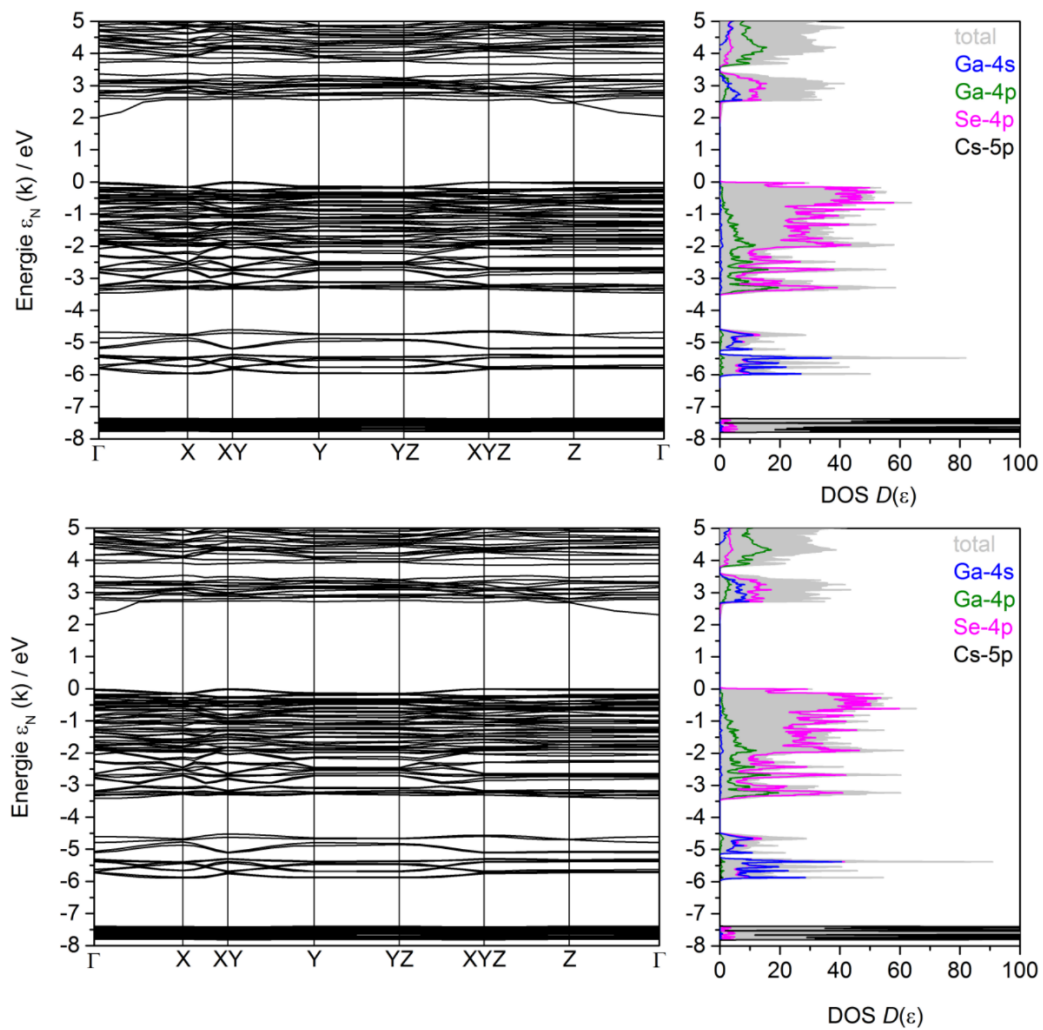


Abbildung S4. Bandstrukturen und DOS mit den Beiträgen der jeweiligen Elemente von $\text{Cs}_4\text{Ga}_6\text{Se}_{11}$ berechnet mit LDA (oben) und PBE (unten)

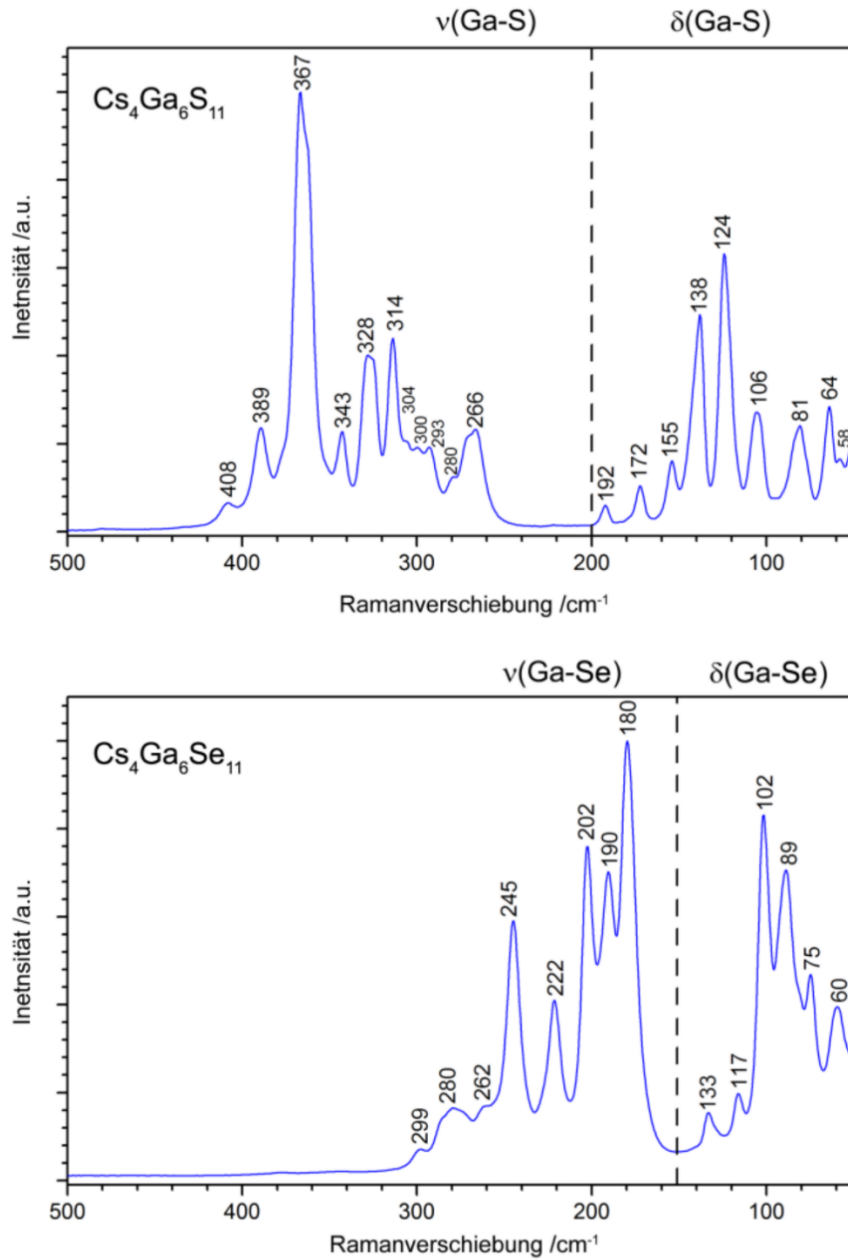


Abbildung S5. Raman-Spektren von $\text{Cs}_4\text{Ga}_6\text{S}_{11}$ (oben) und $\text{Cs}_4\text{Ga}_6\text{Se}_{11}$ (unten) im Bereich von 50 – 500 cm^{-1} .

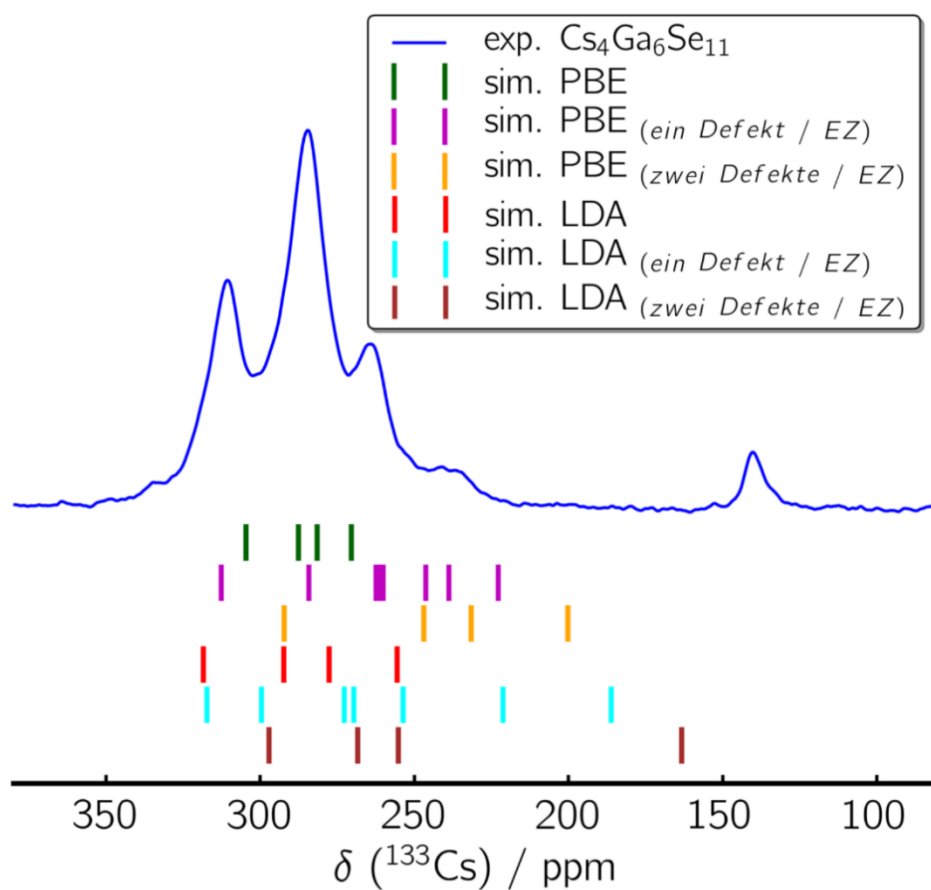


Abbildung S6. ^{133}Cs MAS NMR Spektrum von $\text{Cs}_4\text{Ga}_6\text{Se}_{11}$ mit per DFT berechneten Werten der chemischen Verschiebungen für die Funktionale PBE und LDA für die ursprüngliche Struktur und Strukturen mit einem bzw. zwei Defekten pro Elementarzelle.

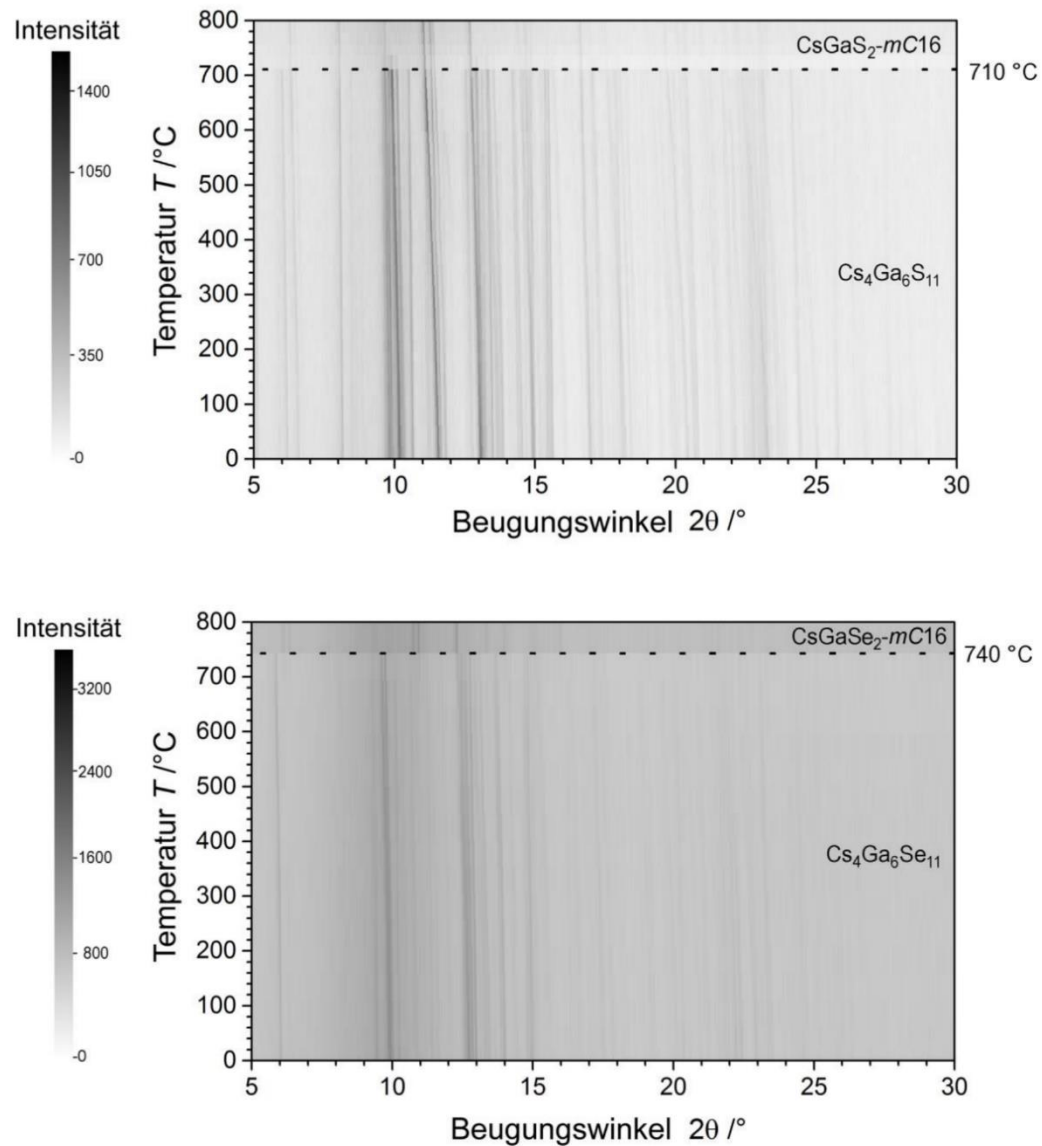


Abbildung S7. Verlauf der Röntgen-Pulverdiffraktogramme (Mo- $K\alpha_1$ Strahlung; $\lambda = 0.70930 \text{ \AA}$; Kapillardurchmesser: 0.3 mm) von $\text{Cs}_4\text{Ga}_6\text{S}_{11}$ (oben) und $\text{Cs}_4\text{Ga}_6\text{Se}_{11}$ (unten) im Temperaturbereich von 25 – 800 °C mit Angabe der vorliegenden kristallinen Phasen. Die Reflexintensitäten sind über den Schwärzungsgrad definiert (vgl. Skala).

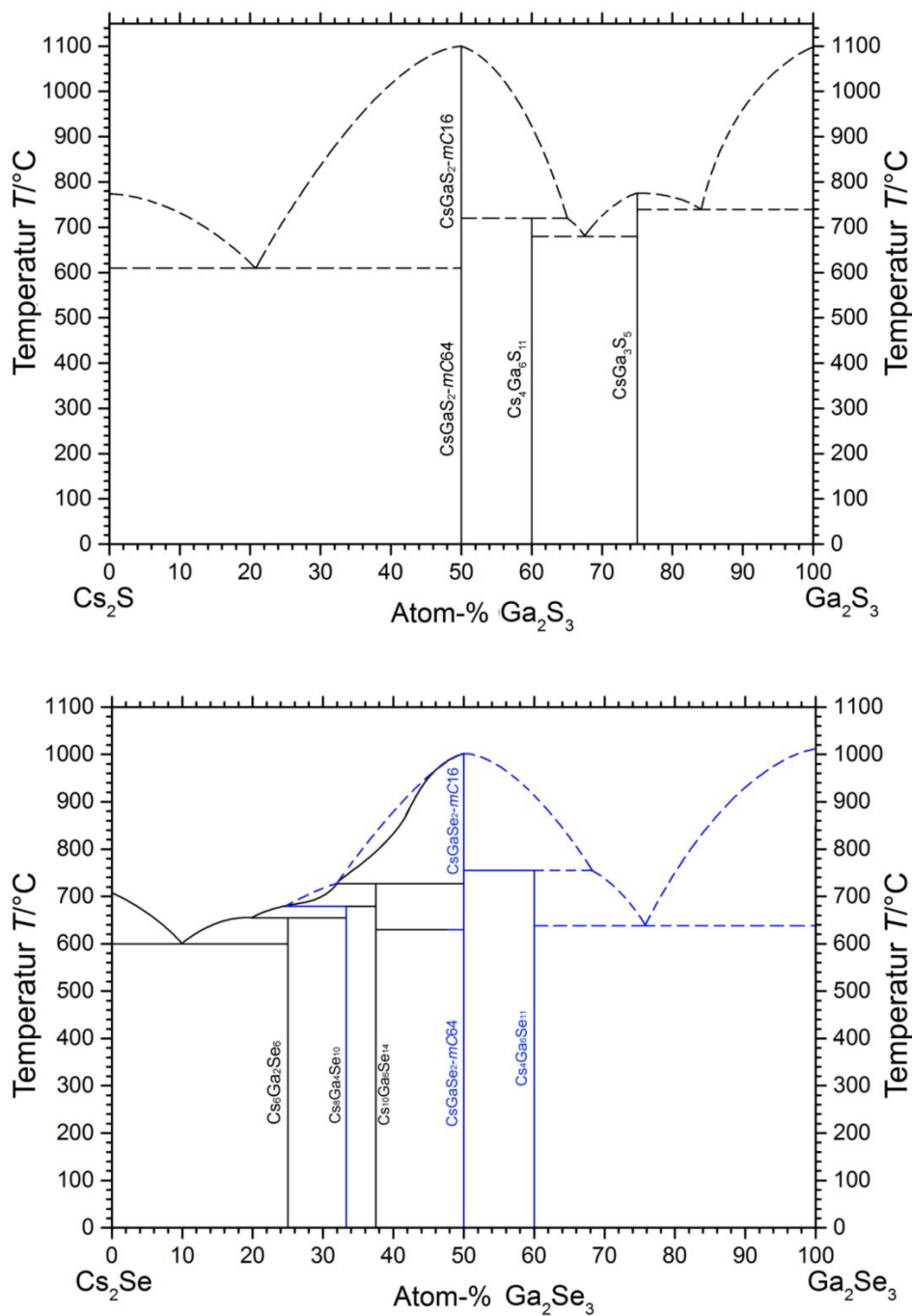


Abbildung S8. Binäre Phasendiagramme der Systeme $\text{Cs}_2\text{S}-\text{Ga}_2\text{S}_3$ (oben) und $\text{Cs}_2\text{Se}-\text{Ga}_2\text{Se}_3$ (unten). Die schwarzen Kurven stammen aus einer Arbeit von Deiseroth^[30] und die blauen Kurven geben den aktuellen Kenntnisstand wieder. Gestrichelte Linien basieren nicht auf tatsächlichen Messwerten sondern wurden mit plausiblen Verlauf eingefügt. Auf der Ga-reichen Seite sind weitere Verbindungen zu erwarten.

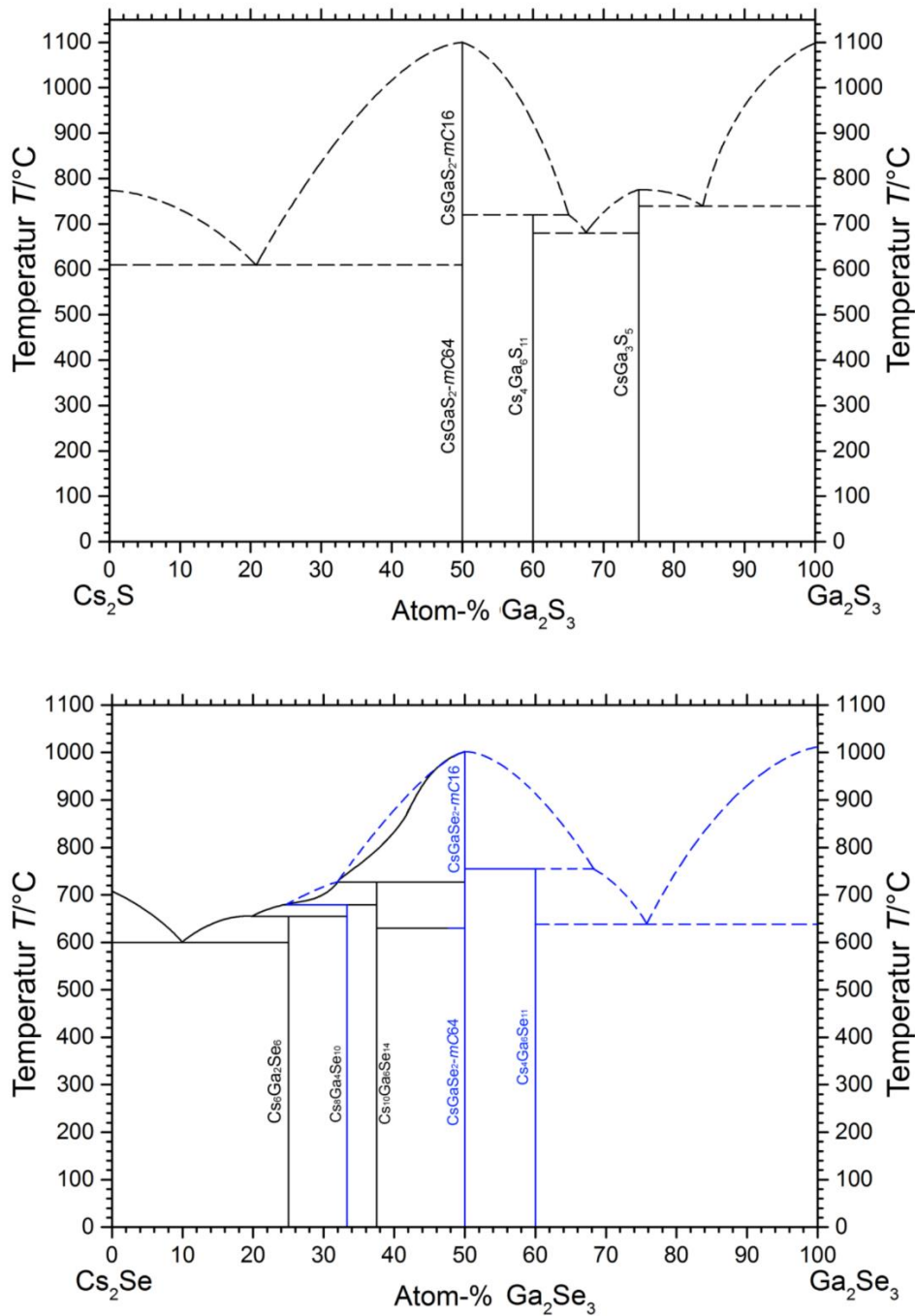


Abbildung S8. Binäre Phasendiagramme der Systeme $\text{Cs}_2\text{S} - \text{Ga}_2\text{S}_3$ (oben) und $\text{Cs}_2\text{Se} - \text{Ga}_2\text{Se}_3$ (unten). Die schwarzen Kurven stammen aus einer Arbeit von Deiseroth^[30] und die blauen Kurven geben den aktuellen Kenntnisstand wieder. Gestrichelte Linien basieren nicht auf tatsächlichen Messwerten sondern wurden mit plausiblen Verlauf eingefügt. Auf der Ga-reichen Seite sind weitere Verbindungen zu erwarten.

Literaturverzeichnis

- [30] H. J. Deiseroth, F. S. Han, *Stud. Inorg. Chem.* **1983**, 18, 655-658.

4.2 Polymorphism in Idasanutlin

This manuscript is the result of a cooperation between the Inorganic Chemistry III of the University of Bayreuth, F. Hoffmann-La-Roche Ltd. 4070 Basel Switzerland and Crystallize! AG 5234 Villigen, Switzerland.

My contributions are:

- conception and main authorship of this article
- crystal structure solution from powder of form III
- analysis of Multinuclear ^1H , ^{13}C , ^{15}N , ^{19}F ssNMR experiments
- quantification of disorders in form III by ^{19}F ssNMR

The other authors contributions are:

- conception and co-authorship of this article
- synthesis of samples
- single crystal structure solutions of form I and III
- synchrotron measurement

Polymorphism in Idasanutlin, a MDM2 antagonist –
a study combining X-ray diffraction, high-resolution
solid-state NMR spectroscopy and quantum
mechanical calculations

*D. Greim, A. Schmutzler, J. Thun, G. Steinfeld, G. Santiso-Quinones, R. Siegel, H. Grüninger and
J. Senker*

D. Greim, A. Schmutzler, Dr. R. Siegel, H. Grüninger and Prof. Dr. J. Senker: Anorganische
Chemie III Universität Bayreuth, Universitätsstraße 32, 95447 Bayreuth, Germany

Dr. G. Steinfeld, Dr. G. Santiso-Quinones: Crystallise! AG, Park INNOVARE: deliveryLab,
5234 Villigen, Switzerland

Dr. J. Thun: Pharma Technical Development Small Molecules, Solid State Sciences, F. Hoffman
La-Roche Ltd., Grenzacher Straße 142, 4070 Basel, Switzerland

Single crystal X-ray structure solution, high-resolution solid-state NMR spectroscopy, Quantum
mechanical calculations

We present the structure solution of two polymorphs, Form I and III, of Idasanutlin, a MDM2 antagonist, combining X-ray diffraction, multinuclear high resolution solid-state NMR spectroscopy and DFT level simulations. The structure solution from single crystal X-ray diffraction using synchrotron radiation showed space group $P1$ with $a=6.525$ $b=12.926$ $c=18.359$ $\alpha =99.62^\circ$ $\beta=91.60^\circ$ and $\gamma=94,15^\circ$ for Form I while the crystal structure solution from powdered samples of Form III yielded a space group $P2_1$ with $a=26.000$ $b=18.565$ $c=6.494$ and $\beta=91.86^\circ$ respectively. Both exhibit a stacked order of Dimers which in Form I follows an AB and in Form III an ABC pattern. Additionally, in the latter disorder in the orientation of one of the benzene rings was observed. Using multinuclear solid-state NMR spectroscopy (ssNMR), performed for both Form I and III combined with quantum mechanical calculations on DFT level, we were able to elucidate the structures. Specifically, using 1D ^{19}F ssNMR spectra combined with DFT level calculations we were able to assign all resonances, including those of the disordered fluorinated benzene rings in Form III. The integrals of these signals fit the X-ray data, yielding a distribution of 0.67/0.23 between the substructures and suggesting a statistical distribution of the two within the crystal structure.

Introduction

The selection of the best suited solid form of an active pharmaceutical ingredient (API) requires the knowledge of the solid form landscape. The selected solid form of the API needs to withstand stresses during the drug substance and drug product manufacturing, like shear stresses upon dry granulation or milling, as well as during shelf life, e.g., relative humidity and temperature excursions. Changes of the solid form may have significant impact on bioavailability and hence on the efficacy, performance and safety of the final drug product.^[1] In

order to identify the best suited solid form, a thorough solid form screening has to be performed and the solid form landscape and transitions pathways need to be known, including hydrates and solvates from at least process relevant solvent systems.

Different types of solid form screenings are described in the literature from high-throughput screening to scale-up experiments to identify the solid form landscape.^[2] Analytical techniques like X-ray powder diffraction (XRPD), single crystal X-ray diffraction, spectroscopy, differential scanning calorimetry (DSC), thermogravimetric analysis with evolved gas analysis (TGA) and dynamic vapor sorption (DVS) help to identify the relationships between solid forms. Knowing the crystal structure of relevant solid forms is not a prerequisite but it simplifies the understanding of the relationship of solid forms. Typically, not all solid forms can be crystallized in the size and quality to solve the crystal structure by single crystal X-ray diffraction. However, with state-of-the-art XRPD laboratory instruments and newest detectors, crystal structure solution from XRPD data is feasible^[3] also for relatively large and flexible organic molecules like typical APIs.^[4,5] In combination with ssNMR, NMR-crystallography is a powerful approach to get confidence on crystal structures of flexible and disordered materials.^[6] In those cases, NMR crystallography can help to overcome the difficulties during structure solution.^[7,8] Due to its resolution of the local environment of the observed nucleus NMR can give additional insights into the crystal structures.^[9,10] This can resolve and explain differences e.g. in hydrogen bonding and packing between different polymorphs.^[1,11] The former can often be determined correlating the ¹H isotropic chemical shift with quantum mechanical chemical shift calculations,^[12] while the latter is accessible through a broad variety of different spin ½ nuclei like ¹³C, ¹⁵N and ¹⁹F.^[13] Fluorine, as a terminal atom, is often of special interest, as it is sensitive to packing, has 100% natural abundance and a high gyromagnetic ratio. This gives rise to a broad variety of

experiments that are feasible, like e.g. 2D double quantum correlation spectra and build-up curves, yielding inter- and intramolecular distances between atoms.^[14] Therefore many complex organic molecules incorporating these nuclei can be investigated, like e.g. Idasanutlin.

Idasanutlin (**1**, Figure 1), is investigated as a potential treatment for a variety of solid tumors and hematologic malignancies and binds to the MDM2 antagonist in order to potentially prevent the p53-MDM2 interaction. Details on the chemical synthesis are reported by Shu et al.^[15] and Rimmner et al.^[16] The solid form landscape of Idasanutlin is rather complex. **1** crystallizes in a variety of different solvates with different types of isomorphous solvate structures. Two

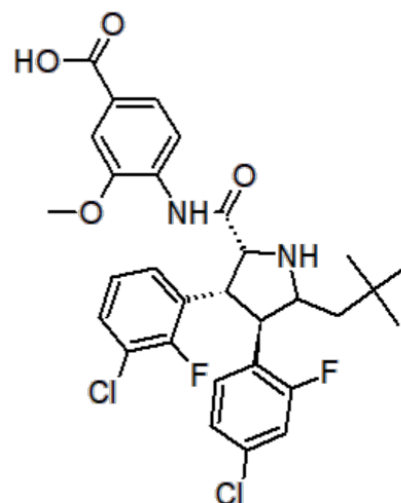


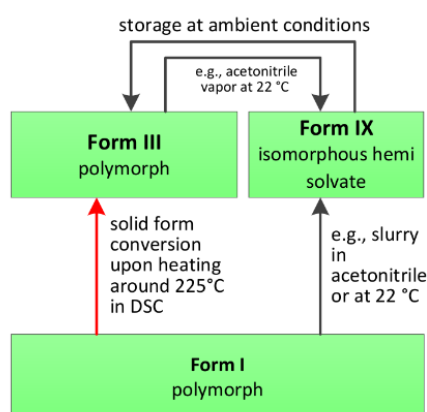
Figure 1: structure of Idasanutlin

anhydrous polymorphs are of special interest, Form I, the (1)

assumed thermodynamically stable form at ambient conditions,

and Form III, a metastable polymorph which is consistently produced by the selected crystallization process. As the final drug product is a stabilized amorphous dispersion, the metastable polymorph is a viable option during chemical synthesis for release of the API as no solid-solid conversion between Form III and Form I was observed so far. The crystal structure of Form I could be solved from single crystal data early on, however, the crystal structure of Form III could not be resolved until recently due to the small crystallite sizes and significant peak overlap (see Figure...). The crystal structure of Form III was of interest as the difference in the packing motif between the thermodynamically stable Form I and the metastable Form III under ambient conditions could help to understand the crystallization behavior. During solid form screening and crystallization process development it turned out the Form III is accessible via a

“transient” solvate Form IX (e.g., an acetonitrile hemi solvate). The interconversion between Form III and Form IX can be achieved easily indicating the structural similarity of Form III and Form IX. However, the correlation with Form I can only be assessed after knowledge of the crystal structure of either Form III and/or Form IX. As the size and the quality of Form III crystals from standard crystallization experiments were not suitable for single crystal structure analysis even using synchrotron radiation, NMR-crystallography was applied on this tricky case. In parallel specialized crystallization techniques were applied in order to grow suitable single crystals for structure solution using synchrotron radiation.



Scheme 1 pathways for transitions between the different polymorphs of Idasanutlin

Experimental section

ss-NMR

^{13}C , ^{15}N and ^{19}F spectra NMR experiments were acquired on Bruker Avance-III HD spectrometers operating at a B_0 field of 9.4T. ^1H spectra were acquired on a Bruker Ascend Aeon 1.0 GHz spectrometer operating at a B_0 field of 23.5 T. ^1H ($\delta = 1000.0$ MHz) and ^{19}F ($\delta = 376.4$ MHz), respectively with a spinning speed of 40 kHz using a commercial Bruker 1.3 mm MAS

triple resonance probe. ^{13}C ($\delta = 100.6$ MHz) and ^{15}N ($\delta = 40.6$ MHz) MAS spectra were obtained with cross-polarization (CP) experiments. The samples were spun at 12.5 kHz (^{13}C) and 10.0 kHz (^{15}N) in a commercial Bruker 4 mm MAS double resonance probe. ^1H and ^{13}C spectra are referenced with respect to TMS (tetramethylsilane) using the secondary standard adamantane. ^{15}N spectra are referenced with respect to CH_3NO_2 using the secondary standard glycine. ^{19}F spectra are referenced with respect to trichlorofluoromethane using the secondary standard NaF?. $^{19}\text{F}^{19}\text{F}$ DQSQ spectra were recorded using the R14₄⁵ sequence with a spinning speed of 40 kHz and recoupling times of 0.2, 0.4, 0.6 and 1.0 ms.^[17] The DFT-D calculations were carried out using the CASTEP 8.0 code.^[18] The GGA with the PBE functional was used.^[19] Semi-empirical dispersion correction was introduced using the scheme of Tkatchenko and Scheffler.^[20] NMR Parameters were calculated using the GIPAW approach.^[21,22] kpoints were distributed using a monkhorst-pack grid^[23] with a spacing of 0.02. The isotropic shieldings were referenced to both Form I and III and the resulting reference shifts were $\delta_{\text{ref}}(^1\text{H}) = 30.2$ ppm; $\delta_{\text{ref}}(^{13}\text{C}) = 170.3$ ppm; $\delta_{\text{ref}}(^{15}\text{N}) = -162.7$ ppm and $\delta_{\text{ref}}(^{19}\text{F}) = 143.0$ ppm respectively.

X-ray diffraction

For the crystal structure solution of Form III from powder synchrotron radiation at the Paul Scherrer Institut (PSI) with a wavelength of 1.001145 Å was used. The indexing, Pawley fitting of each cell and the simulated annealing runs were done using the TOPAS 5 software package. For simulated annealing a rigid body was defined using the dimer motif of Form I. The degrees of freedom were restricted to the dihedral angles of the benzene rings, the opening angle between the two, the length of the hydrogen bonds and the symmetry restricting angle of these. After an initial structure solution with a rather high weighted Rvalue of 12.7%, we introduced a second fluorinated benzene ring for which the sum of occupancies for each affected atom was

restricted to one, according to: $\text{Occ}_i + \text{Occ}_j = 1$. After final Rietveld refinement with relaxation the atom positions within 0.0001* the x, y and z-directions the structure solution reaches a wR-value of 6.4%.

Results & Discussion

XRD

Form I crystallizes in space group $P1$ with cell parameters of $a=6.53 \text{ \AA}$ $b=12.93 \text{ \AA}$ $c=18.36 \text{ \AA}$ and $\alpha=99.63^\circ$ $\beta=91.60^\circ$ $\gamma=94.15^\circ$, while Form III crystallizes in $P2_1$ with cell parameters of $a=6.41 \text{ \AA}$, $b=18.21 \text{ \AA}$ $c=25.83 \text{ \AA}$ and $\beta=92.18^\circ$. When looking at the cell volume and the number of molecules in the asymmetric unit it becomes evident, that Form III ($V=3012.86 \text{ \AA}^3$, $Z=4$, $Z'=2$) is a multiple of Form I ($V= 1514.79 \text{ \AA}^3$, $Z=Z'=2$). This is amongst others caused by Idasanutlin (Fig. 1) being a rather rigid molecule. Due to a delocalised π -system, the acid group, the corresponding benzene ring, the amide group, and to a certain extend the methoxy group as well, all lie within a plane. While the bond between the amide function and the five-membered ring is rotatable, the five-membered ring in the centre of the molecule does not have any degree of freedom. The remaining parts of the molecule are the 2,2 Dimethylpropyl group and the fluorinated and chlorinated benzene rings which are, in principle, rotatable but sterically hindered. As the molecular overlay of Form I and III shows (Fig. 1) Idasanutlin exhibits only minor differences in its conformation between the polymorphs with the main difference being the angles of the fluoro-chloro benzene rings towards the five-membered ring. The 2,2 Dimethylpropyl group has almost the same orientation in both crystal structures. In a molecule overlay, this yields a low RMSD of 0.46 \AA between Form I and III with the maximum deviation being the chlorine atoms with a difference of 1.56 \AA . Comparing the molecules of structure solutions from powder and single crystal data yields an average RMSD values of 0.22 and

0.34 Å. For the first molecule the maximum deviation is as low as 0.4 Å while for the second one it reaches 1.2 Å. This is caused as the methyl atoms are rotated by $\sim 30^\circ$ between the two solutions (Fig S?). Due to thermal motion these have rather high displacement factors in the single crystal structure solution of **INSERT VALUE**.

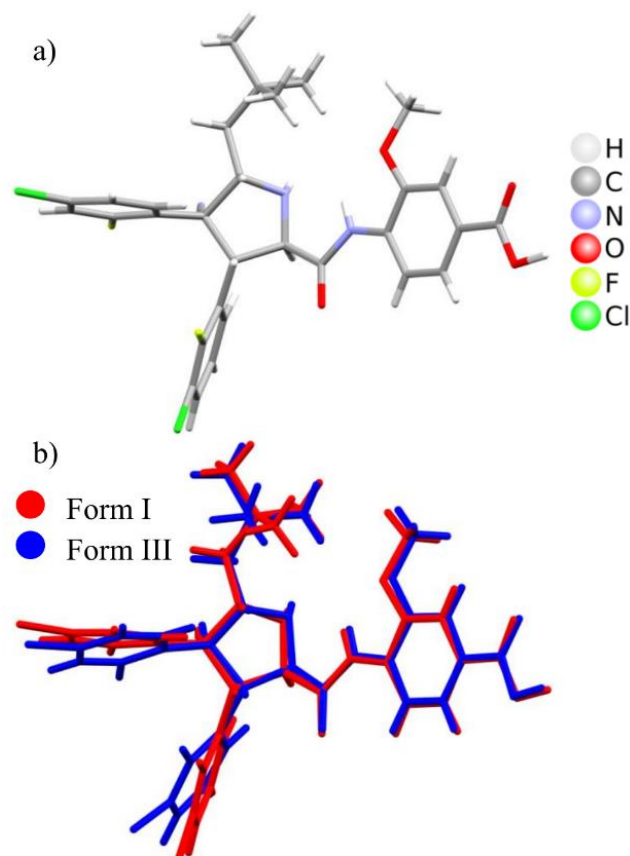


Figure 2: a) Three dimensional illustration of Idasanutlin. b) Molecule overlay of Form I (red) and III (blue) of Idasanutlin.

The packing of the molecules is mainly driven by hydrogen bonding. Both polymorphs form a dimer motif where the acid groups, the corresponding benzene rings, the methoxy groups and the amide groups of both molecules lie within a plane (Scheme 2b). For the second molecule in the dimer the bond between the amide group and the five-membered ring is rotated by 180° so that the methoxy groups of both molecules lie on the same side of the dimer. These dimers show a

slightly different hydrogen bonding pattern though. While Form I exhibits symmetric hydrogen bonding Form III shows asymmetric bonding. In both polymorphs these dimers are stacked on top of each other in a chair like manner so that each one is slightly shifted towards the others (Scheme 2c). These stacks are then arranged in a brick like structure so that each layer of bricks is shifted by 1/3 of the length of one brick towards the subjacent layer/brick. For Form I this results in an ABC like stacking while for Form III AB layering is realised (Scheme 2d). This AB layering adds symmetry to the structure in a way that a 2-fold screw axis is introduced according to the space group $P2_1$ that this structure inhibits. Additionally, Form III exhibits a certain degree of disorder. The ortho-flouro para-chloro benzene ring of one of the two molecules in the asymmetric unit is tilted by 180° with occupancy of 0.23. Detailed information of the structures can be found in Table S1.

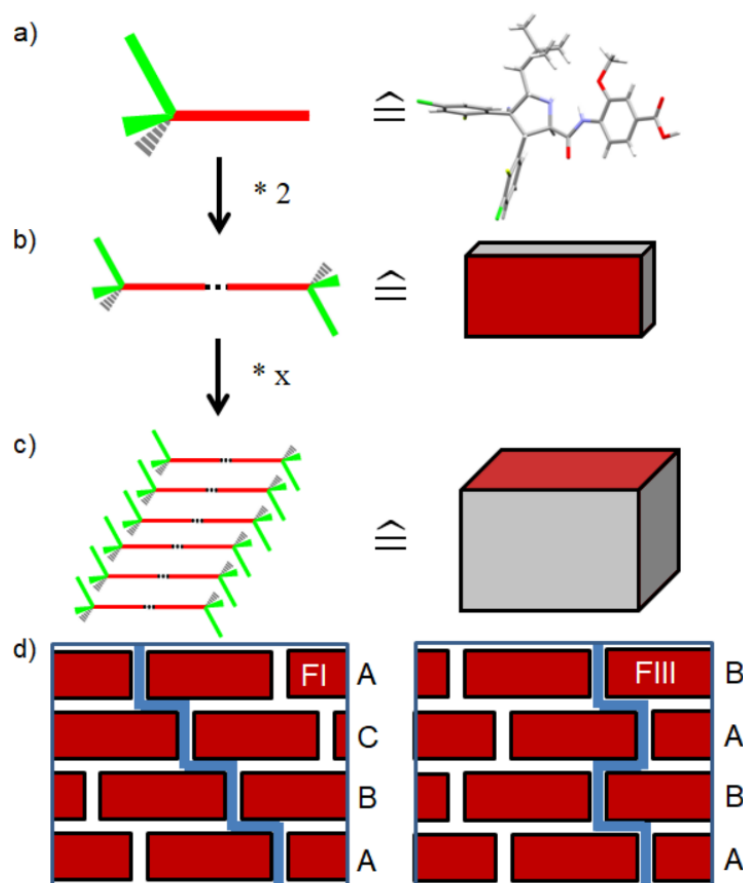


Figure 3: Representation of the packing of both Form I and III of Idasanutlin. Scheme of a single molecule (a), the dimer motif (b), the chair like stapled dimers forming brick like structures (c) and the arrangement of these bricks in Form I and III (d).

NMR & DFT

The high resolution ss- ^1H MAS spectra of Form I and III (Fig. 2, Fig S3 & S4) show a broad range of signals over the whole width of the frequency range. The rather sharp resolved two signals in the lower ppm region of the spectrum (0-2 ppm) can be assigned to CH_3 , CH_2 and NH signals. The range from 2.5 to 5 ppm shows signals of the methoxy- and CH groups of the five-membered rings whereas the part of the spectrum above ~ 9 ppm shows solely aromatic protons. Above those lie the amide and acid protons. Even though the general ranges for the different

chemical groups are the same for both Forms there are three notable differences between the spectra. First signals the CH and methoxy groups split up in Form III whereas in Form I they only yield a single resonance. Secondly Form III shows a smaller shift region of the aromatic hydrogen atoms and finally the splittings of the signals of both the amide and the acid hydrogen atoms are different. All of these are caused by the differences in packing in both forms and the latter shows that the hydrogen bonding has to be symmetric in Form I while it has to be asymmetric for Form III. This information was essential for the structure solution from powder data as it reduced the degrees of freedom for the molecules significantly. The differences are also reproduced by the DFT calculated shifts of all hydrogen atoms that are not strongly influenced by thermal motion (Table S2). Most notably the splittings in the higher ppm region, where the acid and amide hydrogen atoms are located, fit the experiment almost perfectly even though the absolute shift values are overestimated.

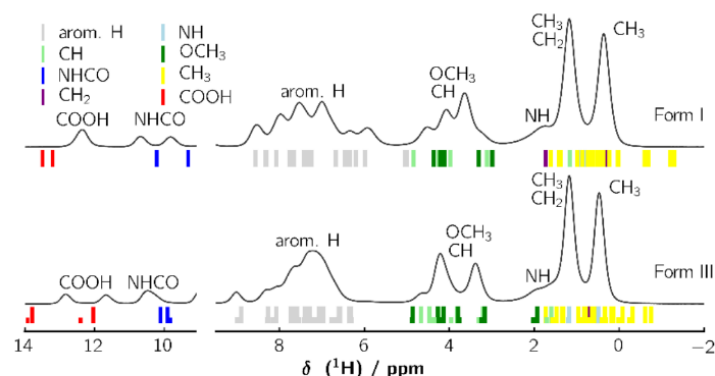


Figure 4. High resolution $ss\text{-}^1\text{H}$ MAS NMR spectra of Form I (top) and III (bottom) measured at 62.5 kHz spinning speed with DFT calculated shifts of each H-atom assigned to its respective chemical group below the spectra. DFT shifts for Form III are scaled according to the occupancy of the substructures. The high ppm region (left) has been referenced separately due to strong overestimation of the shifts of the hydrogen bridged acid protons.

Due to the vast number of signals and the rather subtle difference the ^{13}C CP NMR spectra serve as a fingerprint identification for the two polymorphs. Still, all signals are clearly resolved and can be assigned to the various chemical groups, except for the aromatic region, where overlap is significant. As was the case in the ^1H spectra the amide and acid groups show variances in their respective shifts, even though these are not as pronounced. In the high field region the influence of the packing are in contrast very distinct. Especially the methoxy, CH_3 and CH_2 groups show differences in the splitting of their respective signals resulting from the distinct packing schemes of Form I and III. The DFT predictions for the chemical shifts fit the experimental values very well and reproduce most of the splittings of the various groups well within the error margin of the method: Even though the highest deviations are in the range of 10 ppm this only occurs for signals that would average within the same chemical group. The grand of calculated values deviates less than 1.5 ppm for both Form I and Form III with the average being 2.16 and 1.39 ppm respectively. The median is 1.35 for Form I and 0.96 for Form III (Table S5).

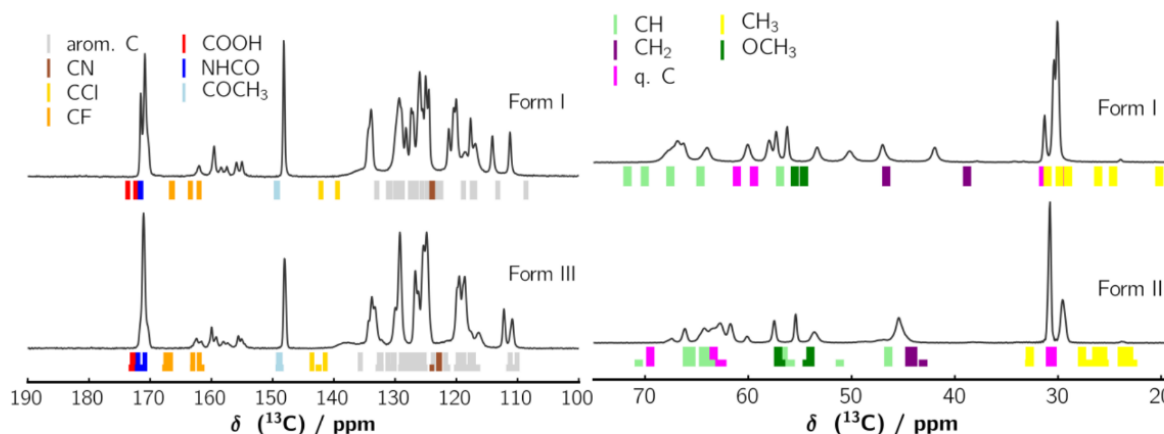


Figure 5. $ss\text{-}^{13}\text{C}$ CPMAS NMR spectra of Form I (top) and III (bottom) with DFT calculated shifts of each C-atom assigned to its respective chemical group below the spectra. DFT shifts for Form III are scaled according to the occupancy of the substructures.

The ^{15}N CPMAS spectra show three distinct signal groups for both polymorphs originating from the three different chemical groups in the molecule. The packing schemes create subtle but distinct differences in the splittings of the NH and amide groups. This leads to an equal splitting for both groups in Form I while for Form III the NH covers a broader shift range. The amide groups, as was already visible in the ^1H spectra, have a very similar environment. The CN group on the other hand does not split up, most probably due to thermal motion. This also explains why the DFT-predicted shifts show splitting for the CN group in Form III which is not visible in the spectrum while all other predictions fit the experiment very well. The ^{15}N spectrum of Form III is the first to show evidence of disorder with an additional smaller signal for the NH group. Quantification using the integrals yields an occupancy of 0.28 - 0.32 for the disordered structure, which is close to the value of 0.23 of the single crystal solution but rather inaccurate due to the noise (Figure 6).

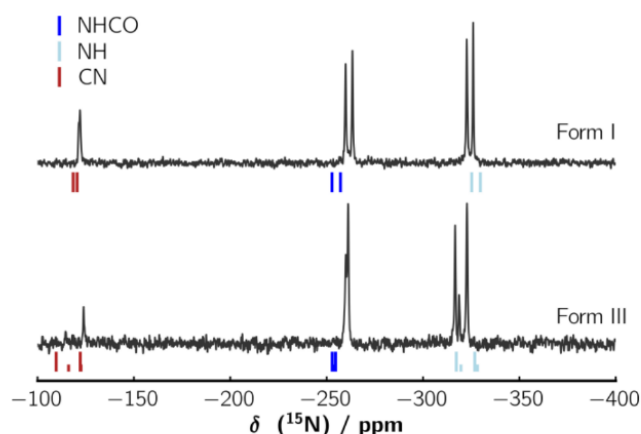


Figure 6. $ss\text{-}^{15}\text{N}$ CPMAS NMR spectra of Form I (top) and III (bottom) measured at 10 kHz spinning speed with DFT calculated shifts of each N-atom assigned to its respective chemical group. DFT shifts for Form III are scaled according to the occupancy of the substructures.

The ^{19}F MAS $ss\text{-NMR}$ spectra (Figure 5) show distinct features of each polymorph and their respective packing. For Form I deconvolution (Figure S1 and Table S2) yields four signals with strong overlap of the ones at -116 ppm. Based on the integrals of 1.07 0.92 1.01 and 1.00 together with the DFT predicted shifts we could assign all signals to the corresponding atom in the crystal structure. In contrast the deconvolution of the spectrum of Form III proved to be non-trivial as it yields seven signals in total with integrals in the range of 0.1 to 1.4 (Figure S2 & Table S3). The DFT predicted shifts for the two substructures enable us to grasp the reason for the additional signals which are caused by the two substructures. Therefore ^{19}F NMR is in contrast to ^1H ^{13}C and ^{15}N in this case the only way to actually further investigate the disorder in Form III. But the DFT calculations of this polymorph only yield six of the seven signals in the spectrum. The small shoulder at -99.1 ppm cannot be explained by calculations of either of the substructures. It seems likely that the additional signal is caused by the boundary between the

two substructures (Figure 8). To investigate this further we recorded $^{19}\text{F}^{19}\text{F}$ DQSQ NMR spectra (Figure 9).

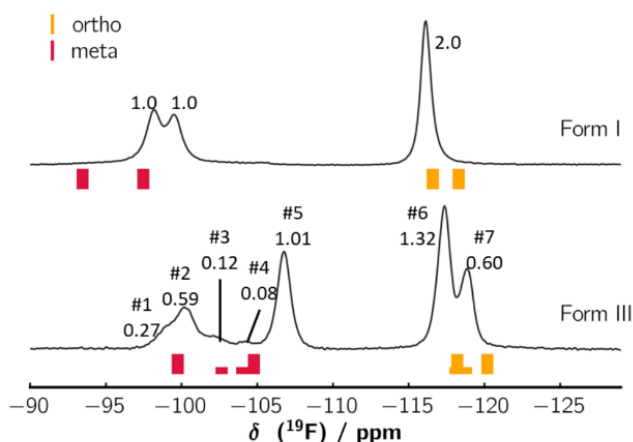


Figure 7. $ss\text{-}^{19}\text{F}$ MAS NMR spectra of Form I and III measured at 40 kHz spinning speed with DFT calculated shifts of each F-atom assigned to its respective chemical group. DFT shifts for Form III are scaled according to the occupancy of the substructures.

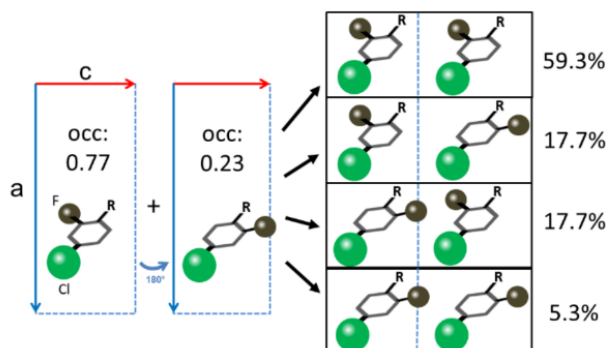


Figure 8: Schematic representation of the possible different Fluorine environments due to the disorder within the structure with their percentage of the whole sample under the assumption that the disorder is distributed statistically.

In these spectra the strong signals can be accounted to shorter distances between the Fluorine atoms, while the ones with low intensities have longer distances. For Form I the cross correlation distances between the three different fluorine species are 4.07, 4.35 Å and 4.58 Å. The self-correlation still yields very weak signals at $\delta_{\text{SQ}} = -99$ ppm, $\delta_{\text{DQ}} = -198$ ppm and $\delta_{\text{SQ}} = -116$ ppm, $\delta_{\text{DQ}} = -232$ ppm where the shortest distance is the length of the a-axis (6.53 Å). For Form III cross correlation between all different species can clearly be seen which lies well within the distances of the different species in the crystal structure. These distances are 2.77, 3.79, 4.07, 4.61 and 4.86 Å respectively. It has to be noted though, that the shortest distance with 2.77 Å only occurs in the substructure with 0.23 occupancy which explains that the intensity of the cross correlations is not much different in comparison to Form I. The self-correlations show only small intensities in the region below $\delta_{\text{SQ}} = -105$ ppm which account for a distance which equals the shortest axis length of 6.49 Å. In contrast the self-correlation at $\delta_{\text{SQ}} = -100$ ppm has considerably higher intensity. This has to be caused by very short interatomic distances between these Fluorine atoms. Due to this short distance DQ-buildup curves (Figure 10) were recorded in order to investigate the two substructures further.

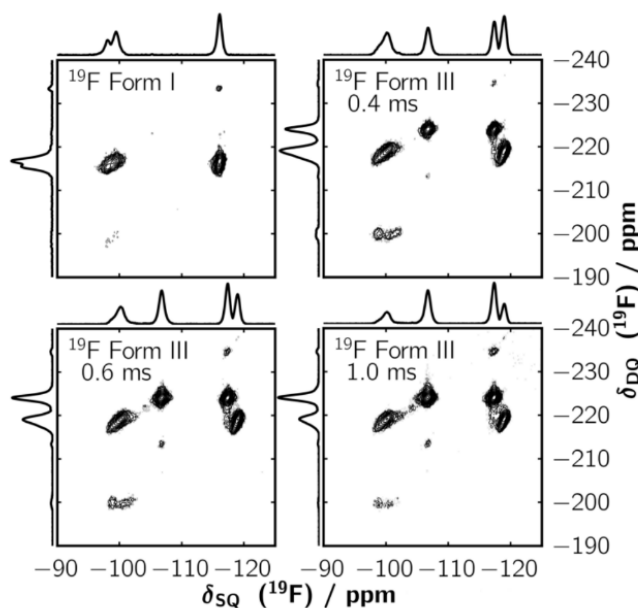


Figure 9. $ss\text{-}^{19}\text{F}^{19}\text{F}$ DQSQ NMR spectra of Form I (top left) and III (top right). Signal intensity indicates distance between the species with short distances resulting in high signal strength and *vice versa*. $^{19}\text{F}^{19}\text{F}$ DQSQ buildup curves for Form III (bottom).

These build up curves in conjunction with the simulated ones from the DFT calculations enabled us to assign each signal in the ^{19}F NMR to its corresponding Fluorine atom in the structure according to position and occupancy. As we already noted signal #1 (naming according to Figure 7) does not have an equivalent from the DFT calculations but the experimental buildup is extremely fast. The only possibility in the structure for such a rapid buildup can be found in the boundary between the two substructures where three Fluorine atoms are within distances of $< 3 \text{ \AA}$ of each other. (Figure 8 third row).

Having assigned each signal to its' corresponding atom in the crystal structure put us in the position to investigate whether the two substructures are distributed statistically or if they occur in domains. For this matter we can simply use the integrations of each signal from the 1D spectrum (Table S3) together with the assignment we got from the build-up curves and

probabilistic evaluation. For two consecutive cells the probability P is given by the occupancy of the given substructure of the first cell multiplied with the occupancy of the next cell and substructure. For a single signal with occupancy distribution of 0.23 and 0.77 this would yield signals with integrals of 0.59, 0.18, 0.18 and 0.05 in the spectrum (Figure 8). Due to the relatively small differences in the surrounding the impact on the chemical shift for all four possibilities is rather small and leads to significant signal overlap in several cases. Assuming distribution of the signals is in fact statistical we can calculate the minorities' occupancy through the square root of the integral of the signal at -118.9 ppm which yields 0.2. In the higher shift region the higher number of signals makes it possible to evaluate if the distribution is statistically and to further refine the occupancy. After assigning the smallest signals to the minority structure again the square root gives the minorities' occupancy of 0.39 which is notably higher than the value from the lower shift part of the spectrum. This can be accounted to an error introduced by the background correction of the spectra. The majority occupancy can be furthermore calculated by the square root of the signal at -100,3 ppm which yields 0,71, much closer to the value gained from both XRD and the lower shift region. With these occupancies we can now test for statistical distribution. In this case the integral for the "mixed" structure would have to have an integral of 0.16 to 0.23. The latter is pretty close to the experimental observed value of 0.26 which is prone to errors introduced by background correction. Therefore we can conclude that the two substructures are distributed statistically and that the distribution lies between 0.61 / 0.39 and 0.8 / 0.2 with an emphasis on the latter one.

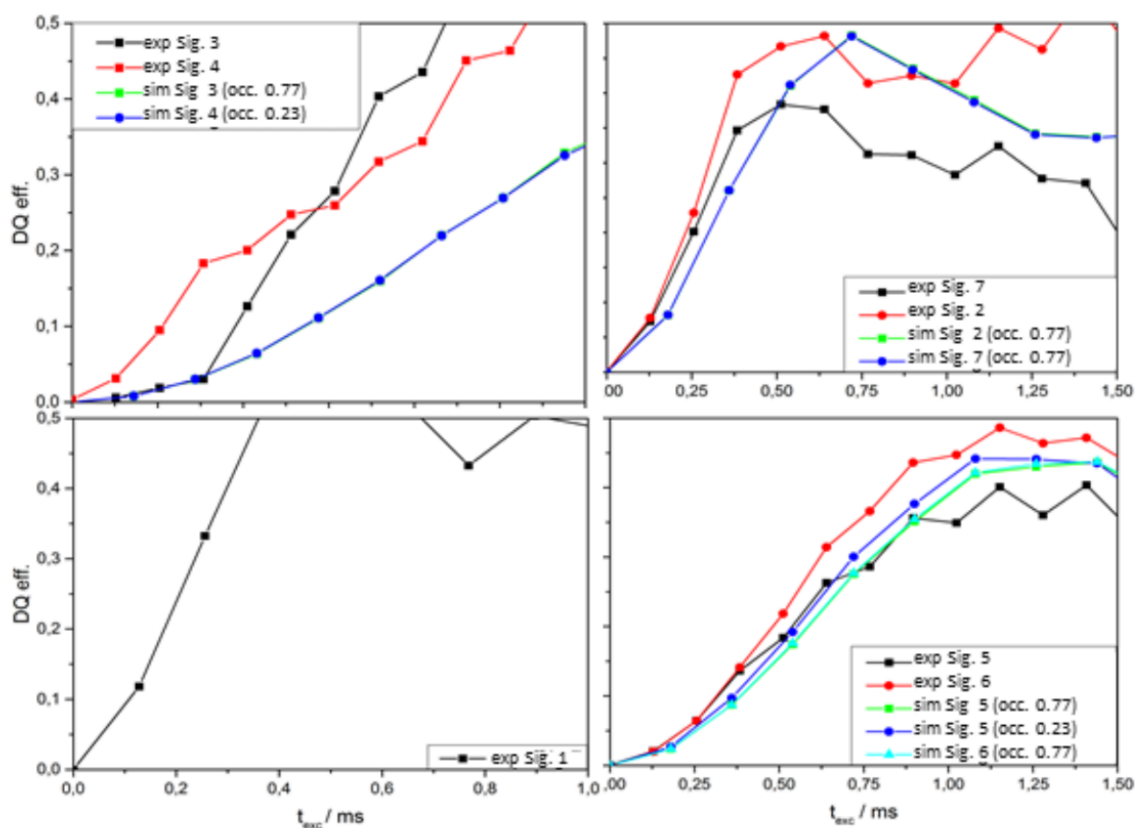


Figure 10: DQ build-up curves for all seven signals of Form III in the ^{19}F ss NMR with simulated build ups for the different substructures from the DFT calculations.

Conclusion

Using a combination of X-ray diffraction, ss-NMR and DFT simulations we were able to solve the structure of two polymorphs of the potential cancerogenic drug Idasanutlin, Form I and III. Both show a dimer motif where the molecules are connected via hydrogen bonds through the acid groups. These dimers are stacked in a chair like manner. The difference between the polymorphs is the arrangement of these stacks with Form I realizing an ABC and Form III exhibiting an AB like layering. While the structure was solved using single crystal X-ray diffraction with the help of DFT calculations and ^1H ss-NMR spectra we were able to resolve the (a-)symmetry of the

hydrogen bonding of the dimer motif. With ^{13}C and ^{15}N spectra we could show the differences in packing especially for the amide group. Focusing on ^{19}F ss-NMR enabled us to further investigate the disorder present in Form III. With 1D and DQ build up curves we were able to assign each signal to the substructures which allowed us to determine that the disorder in Form III is distributed statistically and to provide a second proof for the occupancies found by XRD.

-
- [1] J. Bauer, S. Spanton, R. Henry, J. Quick, W. Dziki, W. Porter, J. Morris, *Pharm. Res.* **2001**, *18*, 859–866.
- [2] A. Newman, *Org. Process Res. Dev.* **2013**, *17*, 457–471.
- [3] J. Thun, L. Seyfarth, J. Senker, R. E. Dinnebier, J. Breu, *Angew. Chemie Int. Ed.* **2007**, *46*, 6729–6731.
- [4] J. Guillon, V. M, P. N, R. L, R. F, S. S, M. S, D. V, M. M, *Struct. Chem. Crystallogr. Commun.* **n.d.**, *2*.
- [5] S. Ahn, A. W. Kahsai, B. Pani, Q.-T. Wang, S. Zhao, A. L. Wall, R. T. Strachan, D. P. Staus, L. M. Wingler, L. D. Sun, et al., *Proc. Natl. Acad. Sci. U. S. A.* **2017**, *114*, 1708–1713.
- [6] D. L. Bryce, F. Taulelle, *Acta Cryst* **1107**, 73–126.
- [7] D. V. Dudenko, P. A. Williams, C. E. Hughes, O. N. Antzutkin, S. P. Velaga, S. P. Brown, K. D. M. Harris, *J. Phys. Chem. C* **2013**, *117*, 12258–12265.
- [8] E. Salager, R. S. Stein, C. J. Pickard, B. Elena, L. Emsley, *Phys. Chem. Chem. Phys.* **2009**, *11*, 2610.
- [9] M. J. Duer, *Introduction to Solid-State NMR Spectroscopy*, Blackwell, **2004**.
- [10] R. K. (Robin K. Harris, R. E. Wasylshen, M. J. Duer, *NMR Crystallography*, Wiley, **2009**.
- [11] M. R. Chierotti, R. Gobetto, C. Nervi, A. Bacchi, P. Pelagatti, V. Colombo, A. Sironi, *Inorg. Chem.* **2014**, *53*, 139–146.

-
- [12] †,‡ Jonathan R. Yates, § Tran N. Pham, † Chris J. Pickard, † Francesco Mauri, ⊥ Ana M. Amado, # and Ana M. Gil, § Steven P. Brown*, **2005**, DOI 10.1021/JA051019A.
- [13] D. L. Bryce, V.-G. J., K. I., B. D. L., G. B., B. D. L., Z. J. W., B. M., M. B. A., B. D. L., et al., *IUCrJ* **2017**, *4*, 350–359.
- [14] C. Zehe, M. Schmidt, R. Siegel, K. Kreger, V. Daebel, S. Ganzleben, H.-W. Schmidt, J. Senker, *CrystEngComm* **2014**, *16*, 9273–9283.
- [15] L. Shu, C. Gu, D. Fishlock, Z. Li, *Org. Process Res. Dev.* **2016**, *20*, 2050–2056.
- [16] G. Rimmler, A. Alker, M. Bosco, R. Diodone, D. Fishlock, S. Hildbrand, B. Kuhn, C. Moessner, C. Peters, P. D. Rege, et al., *Org. Process Res. Dev.* **2016**, *20*, 2057–2066.
- [17] P. E. Kristiansen, D. J. Mitchell, J. N. S. Evans, *J. Magn. Reson.* **2002**, *157*, 253–266.
- [18] S. J. Clark, M. D. Segall, C. J. Pickard, P. J. Hasnip, M. I. J. Probert, K. Refson, M. C. Payne, *Zeitschrift für Krist. - Cryst. Mater.* **2005**, *220*, 567–570.
- [19] J. P. Perdew, K. Burke, M. Ernzerhof, *Phys. Rev. Lett.* **1996**, *77*, 3865–3868.
- [20] A. Tkatchenko, M. Scheffler, *Phys. Rev. Lett.* **2009**.
- [21] J. Yates, C. Pickard, F. Mauri, *Phys. Rev. B* **2007**.
- [22] C. Pickard, F. Mauri, *Phys. Rev. B* **2001**.
- [23] H. J. Monkhorst, J. D. Pack, *Phys. Rev. B* **1976**, *13*, 5188–5192.

Polymorphism in Idasanutlin a MDM2 antagonist –
a X-Ray, high resolution solid state NMR and
quantum mechanical study

Supporting Info

Index

1. Experimental Details	2
1.1 X-Ray.....	2
1.2 NMR	2

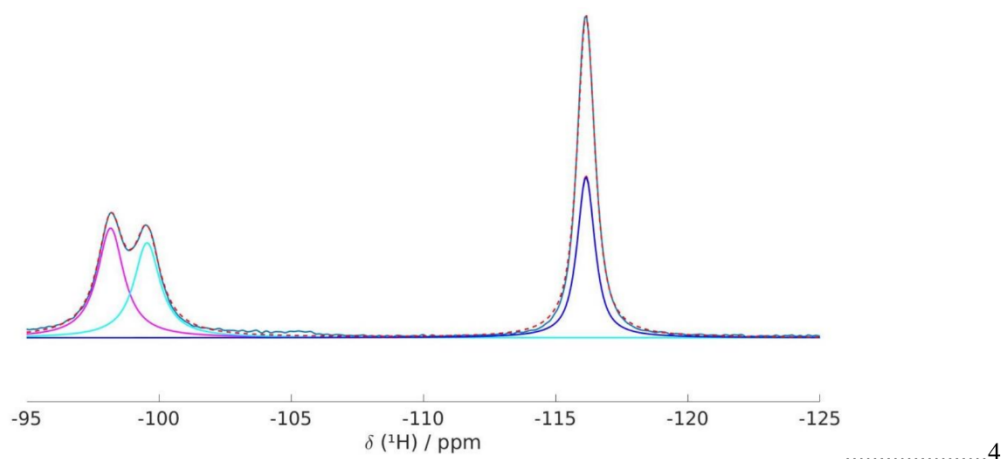
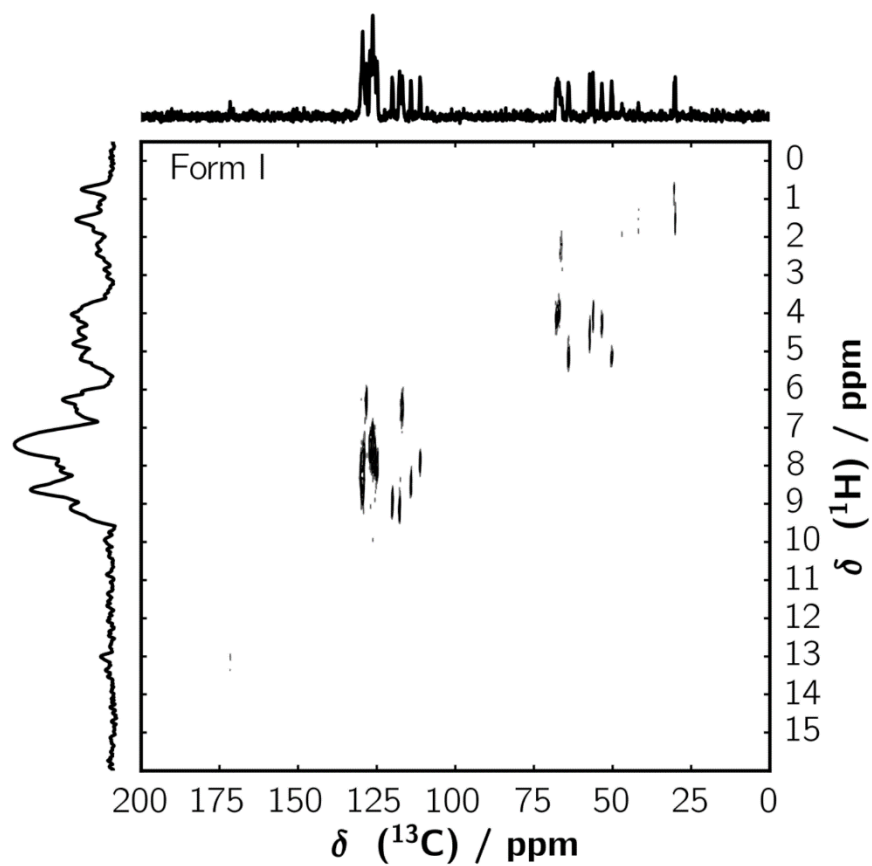


Figure S 4: Super high resolution DQSQ correlation spectra of Form I of Idasanutlin.....6



.....	7
1.3 DFT-D Calculations	8
2. Structural Details of Form I and III of Idasanutlin	9
Insert molecule overlay of structure solution from powder and single crystal	Error! Bookmark not defined.
Evaluation of DFT calculated shifts.....	11

1. Experimental Details

1.1 X-Ray

1.2 NMR

^{13}C , ^{15}N and ^{19}F spectra NMR experiments were acquired on Bruker Avance-III HD spectrometers operating at a B_0 field of 9.4T. ^1H spectra were acquired on a Bruker Ascend Aeon 1.0 GHz spectrometer operating at a B_0 field of 23.5 T. ^1H ($\delta = 1000.0$ MHz) and ^{19}F ($\delta = 376.4$ MHz) spectra were acquired after a 90° flip angle pulse of $1.6 \mu\text{s}$ (^1H) and $3.5 \mu\text{s}$ (^{19}F), respectively with a spinning speed of 40 kHz using a commercial Bruker 1.9 mm MAS triple resonance probe. The relaxation delay was set to 10.0 s (^1H) and 30.0 s (^{19}F). ^{13}C ($\delta = 100.6$ MHz) and ^{15}N ($\delta = 40.6$ MHz) MAS spectra were obtained with ramped cross-polarization (CP) experiments where the nutation frequency ν_{nut} on the proton channel was varied linearly from 50– 100% and 70- 100%. The samples were spun at 12.5 kHz (^{13}C) and 10.0 kHz (^{15}N) in a commercial Bruker 4 mm MAS double resonance probe. The corresponding ν_{nut} on the ^{13}C channel and the contact time were adjusted to 70 kHz and 3.0 ms, respectively. On the ^{15}N channel, the corresponding ν_{nut} and the contact time were adjusted to 35 kHz and 5.0 ms, respectively. Proton broadband decoupling with spinal-64 and $\nu_{\text{nut}} = 70$ kHz was applied during acquisition.[17] ^1H and ^{13}C spectra are referenced with respect to TMS (tetramethylsilane) using the secondary standard adamantane. ^{15}N spectra are referenced with respect to CH_3NO_2 using the secondary standard glycine. ^{19}F spectra are referenced with respect to trichlorofluoromethane using the secondary standard NaF?. ^{19}F DQSQ spectra were recorded using the R14₄⁵ sequence with a spinning speed of 40 kHz and recoupling times of 0.2, 0.4, 0.6 and 1.0 ms.[18]

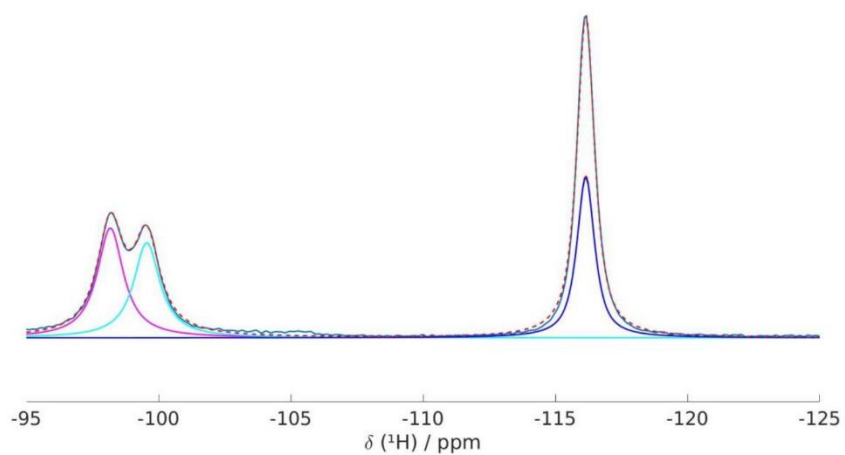


Figure S 1: Deconvolution of the ^{19}F single pulse spectrum of Form I of Idasanutlin.

Table S 1: Values for δ_{iso} , Integrals, Gauss/Lorentz ratio and full width half maximum from the deconvolution of the ^{19}F spectrum of Form I.

$\delta_{\text{iso}} / \text{ppm}$	-98,18	-99,55	-116,2	-116,2
Int.	1,0713	0,9276	1,005	0,9961
G/L	0,005	0,005	0,15	0,15
FWHM	1,2	1,2	0,8	0,8

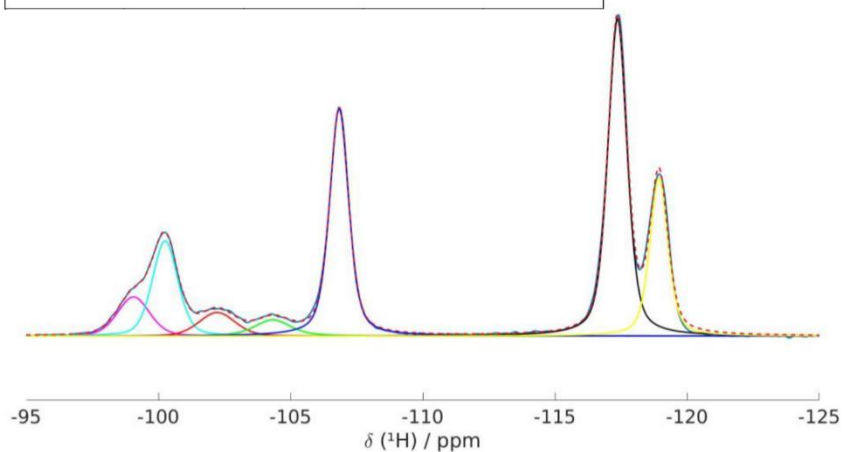


Figure S 2: Deconvolution of the ^{19}F single pulse spectrum of Form III of Idasanutlin.

Table S 2: Values for δ_{iso} , Integrals, Gauss/Lorentz ratio and full width half maximum from the deconvolution of the ^{19}F spectrum of Form III.

δ_{iso} / ppm	-99,06	-100,3	-102,2	-104,3	-106,8	-117,4	-118,9
Int.	0,2582	0,5068	0,1738	0,1353	0,9791	1,36	0,64
G/L	0,75	0,6976	0,75	0,45	0,5284	0,5462	0,55
FWHM	1,4324	1,1318	1,6	1,6	0,8549	0,8566	0,8093

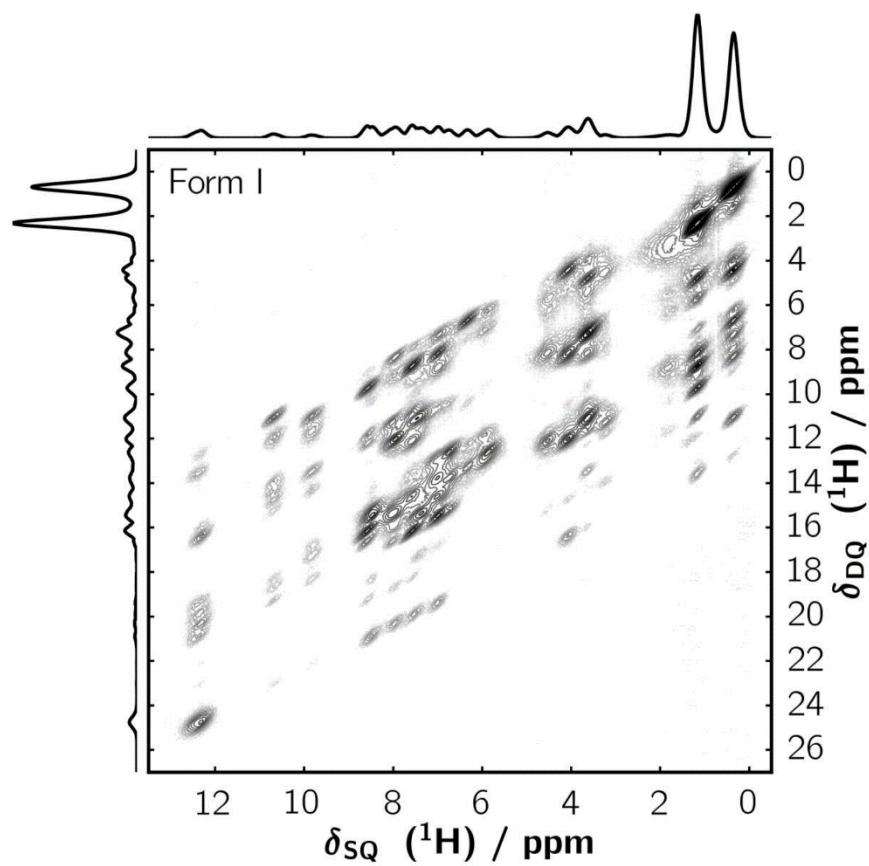


Figure S 3: Super high resolution DQSQ correlation spectra of Form I of Idasanutlin.

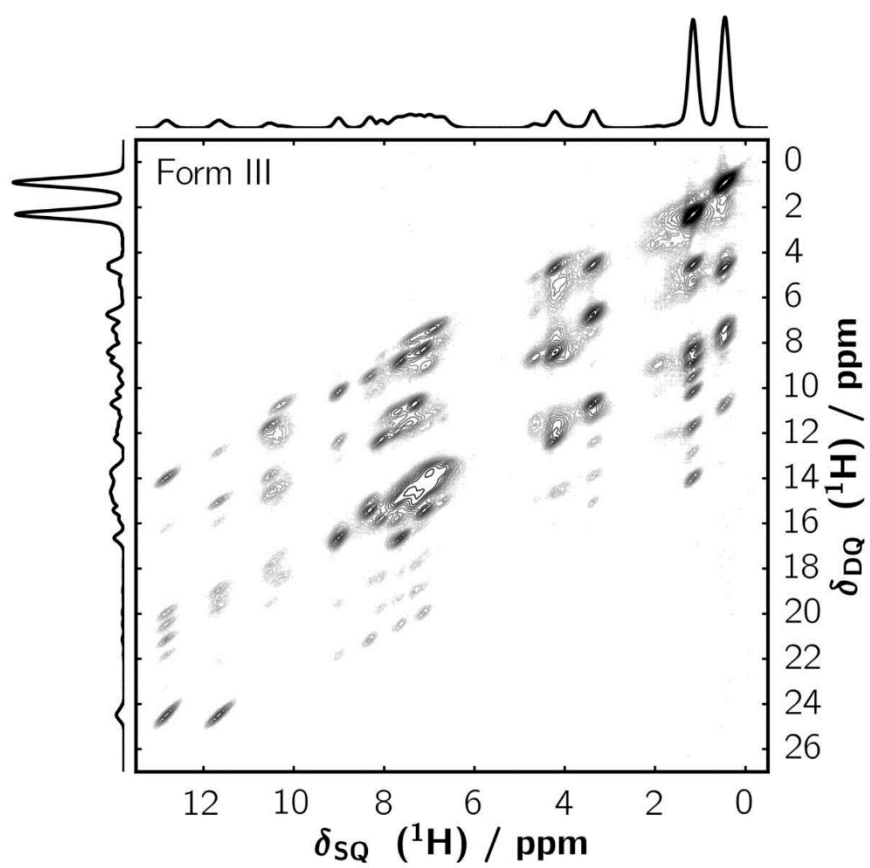


Figure S 4: Super high resolution DQSQ correlation spectra of Form I of Idasanutlin.

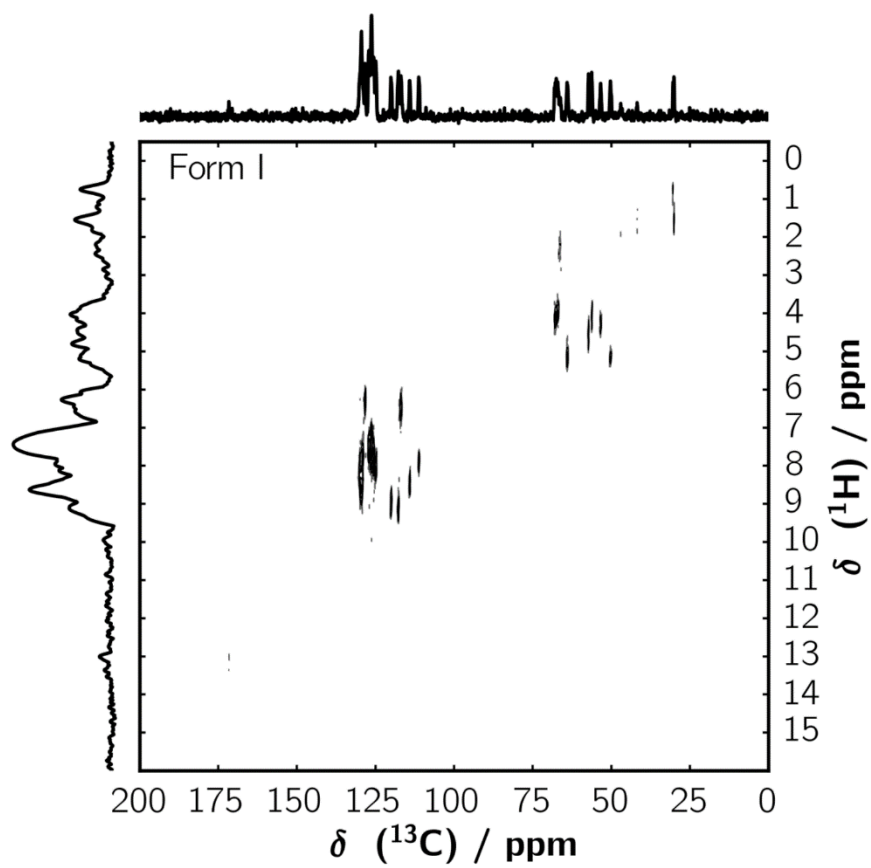


Figure S 5: $^1\text{H} - ^{13}\text{C}$ 2D correlation spectrum of Form I of Idasanutlin recorded using the PRESTO sequence.

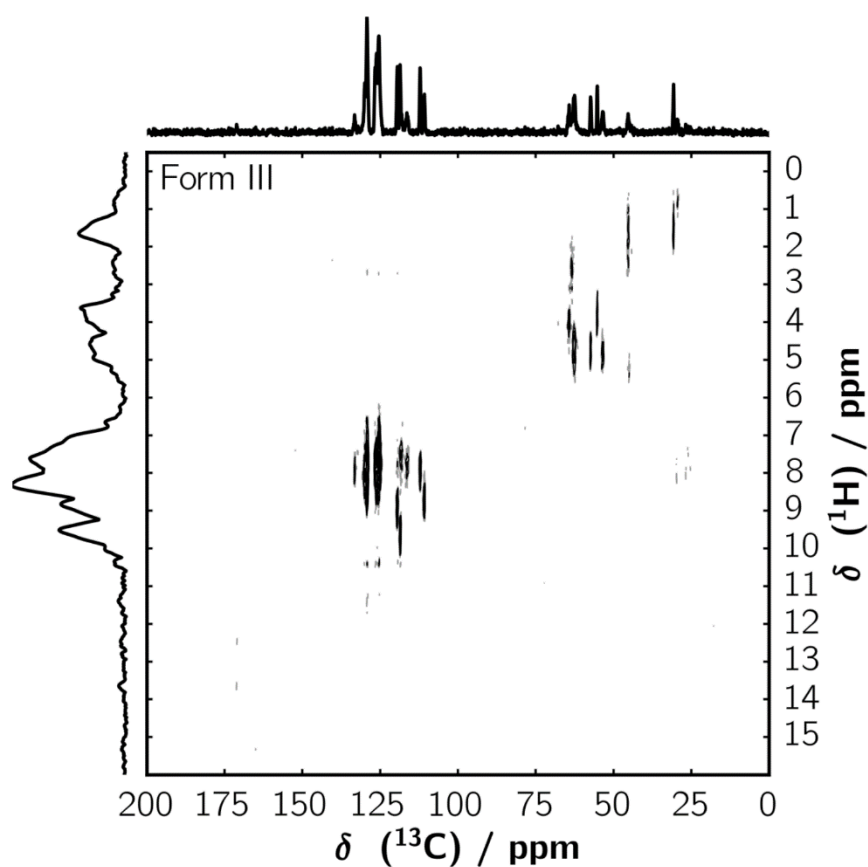


Figure S 6: $^1\text{H} - ^{13}\text{C}$ 2D correlation spectrum of Form I of Idasanutlin recorded using the PRESTO sequence.

1.3 DFT-D Calculations

The DFT-D calculations were carried out using the CASTEP 8.0 code.[19] The GGA with the PBE functional was used.[20] A plane-wave basis set with an energy cutoff of 650 eV was applied and the core electrons were represented by ultra-soft pseudopotentials. K-points were distributed using a Monkhorst-Pack-grid[21] with a reciprocal spacing of 0.03. Semi-empirical

dispersion correction was introduced using the Scheme of Tkatchenko and Scheffler.[22] For the geometry optimization the convergence tolerances of energy, maximum force, and maximum displacement were 2.0×10^{-5} eV per atom, 5.0×10^{-2} eV \AA^{-1} and 1.0×10^{-3} \AA^{-1} , respectively. The allowed stress tolerance was 0.1 GPa. NMR Parameters were calculated using the GIPAW approach.[23,24] The isotropic shieldings were referenced on both Form I and III and the resulting reference shifts were $\delta_{\text{ref}}(^1\text{H}) = 30.2$ ppm; $\delta_{\text{ref}}(^{13}\text{C}) = 170.3$ ppm; $\delta_{\text{ref}}(^{15}\text{N}) = -162.7$ ppm and $\delta_{\text{ref}}(^{19}\text{F}) = 143.0$ ppm respectively.

2. Structural Details of Form I and III of Idasanutlin

Table S 3: Details of the single crystal structure solution of both Form I and III.

	Form I	Form III
Radiaton	Synchrotron, 0.70047 nm	Synchrotron, 0.70047 nm
Formula	C ₃₁ H ₂₉ Cl ₂ F ₂ N ₃ O ₄	C ₃₁ H ₂₉ Cl ₂ F ₂ N ₃ O ₄
M (g/mol)	616.487	616.487
Z, calculated density (g/cm³)	2, 1.346	4, 1.360
No. of Reflections		39194
No. of Reflections(I/σ > 2.0)		12056
T/K	89	100
Θ range (°)		0.778 – 25.973
Crystal system	Triclinic	Monoclinic
Space group	<i>P1</i>	<i>P2₁</i>
a / Å	6.5250(13)	6.4050(13)
b / Å	12.926(3)	18.206(4)
c / Å	18.359(4)	25.829(5)
α	99.63(3)	90.0
β	91.60(3)	92.18(3)
γ	94.15(3)	90.0
Rp	0.0359	0.0491
Rp (I/σ > 2.0)	0.0359	0.0410
wRp	0.0359	0.1071
wRp (I/σ > 2.0)	0.0359	0.1023

Evaluation of DFT calculated shifts

Table S 4: ^1H NMR experimental isotropic shifts with simulated ones and the deviation between the two.

Form I			Form III		
exp.	sim.	RMSD	exp.	sim.	RMSD
12,48	14,3	1,82	12,82	14,74	1,92
10,82	11,17	0,35	11,66	12,99	1,33
9,99	10,26	0,27	10,58	10,96	0,38
8,7	8,51	0,18	10,26	8,2	2,06
8,08	8,19	0,1	9,04	8,9	0,14
7,64	7,68	0,04	8,39	81529	81520,61
7,09	7,29	0,2	8,02	8,03	0,01
6,47	6,46	0,01	7,62	7,6	0,02
6,1	6,13	0,03	7,22	7,24	0,02
4,71	4,98	0,26	6,88	6,91	0,03
4,24	4,1	0,15	6,52	6,58	0,06
3,76	3,33	0,43	6,1	6,28	0,18
2,1	2,94	0,84	4,68	4,61	0,07
1,26	1,2	0,06	4,32	3,28	1,04
0,45	0,1	0,35	3,83	3,84	0,01
			3,35	3,18	0,17
			2,8	1,93	0,87
			2,2	1,61	0,59
			1,73	1,14	0,59
			1,14	1,28	0,14
			0,44	0,18	0,26

Table S 5: ^{13}C NMR experimental isotropic shifts with simulated ones and the deviation between the two.

Form I			Form III		
exp.	sim.	RMSD	Exp.	sim.	RMSD
171.53	173.26	1.73	171.07	172.52	1.45
170.88	171.98	1.11	171.07	171.98	0.91
170.36	171.13	0.76	170.46	171.6	1.14
170.36	171.22	0.86	170.46	170.47	0.01
160.81	166.13	5.32	160	167.03	7.03
160.81	165.98	5.16	160.58	166.29	5.71
158.43	163.04	4.61	157.38	162.65	5.27
156.51	161.61	5.1	156.47	161.58	5.11
148.17	149.02	0.85	148.08	148.64	0.56
148.17	148.79	0.63	148.08	148.38	0.3

134.36	132.61	1.76	134.34	135.3	0.96
133.93	132.59	1.34	133.8	132.18	1.62
129.94	130.69	0.74	133.26	131.91	1.35
129.34	130.58	1.24	130.01	130.79	0.78
128.94	130.41	1.47	129.2	129.94	0.74
128.52	129.52	1	129.2	129.75	0.55
128.36	129.17	0.81	129.2	128.58	0.62
128.22	128.57	0.35	129.2	128.4	0.8
127.35	128.42	1.07	129.2	128.21	0.99
127.09	127.11	0.02	126.69	127.65	0.96
126.2	127.05	0.85	126.69	126.95	0.26
125.97	126.99	1.02	126.18	126.23	0.05
125.51	126.74	1.23	125.41	125.56	0.15
125.04	126.39	1.36	125.41	125.29	0.12
125.04	126.34	1.3	125.41	125.51	0.1
124.49	126.17	1.68	125.41	125.19	0.22
121.2	125.26	4.06	124.83	124.86	0.03
121.2	124.41	3.21	124.83	123.37	1.46
121.2	123.87	2.67	119.5	122.31	2.81
120.44	123.63	3.19	119.5	122.49	2.99
120.02	122.9	2.88	119.5	121.34	1.84
120.02	122.13	2.11	119.5	119.3	0.2
117.67	116.75	0.92	118.61	118.71	0.1
116.84	116.6	0.24	116.34	116.8	0.46
114.12	112.84	1.28	110.91	110.81	0.1
111.23	108.22	3.01	110.91	109.68	1.23
67.77	71.3	3.53	67.44	69.11	1.67
66.84	69.63	2.79	66.15	65.54	0.61
66.24	67.15	0.91	64.31	65.12	0.81
63.96	64.24	0.28	63.46	63.99	0.53
60.04	56.53	3.51	62.67	63.24	0.57
57.99	60.71	2.72	61.73	62.95	1.22
57.3	59.05	1.75	60.13	56.71	3.42
56.26	55.1	1.16	57.48	56.2	1.28
53.33	54.24	0.91	55.41	56.71	1.3
50.16	54.2	4.04	53.61	53.59	0.02
46.99	46.24	0.75	45.41	44	1.41
41.93	38.41	3.52	45.41	43.62	1.79
31.3	30.61	0.69	30.78	32.34	1.56
30.4	29.45	0.95	30.78	30.39	0.39
30.4	28.62	1.78	30.78	30.11	0.67
30.04	25.71	4.33	30.78	27.28	3.5
30.04	24.26	5.78	30.78	25.89	4.89

30.04	19.79	10.25	30.78	25.23	5.55
			29.51	23.42	6.09
			29.51	22.72	6.79

Table S 6: ^{15}N NMR experimental isotropic shifts with simulated ones and the deviation between the two.

Form I					
exp.	sim.	RMSD	exp	sim	RMSD
-121,46	-119,22	2,24	-123,9	-110,44	13,46
-122,01	-121,33	0,68	-123,9	-122,88	1,02
-259,85	-253,55	6,3	-123,9	-116,88	7,02
-263,38	-257,91	5,47	-123,9	-123,31	0,59
-322,73	-325,99	3,26	-259,84	-254,25	5,59
-326,06	-330,55	4,49	-259,84	-253,64	6,2
			-261,11	-255,4	5,71
			-261,11	-255,27	5,84

Table S 7: ^{19}F NMR experimental isotropic shifts with simulated ones and the deviation between the two.

Form I			Form III		
exp	sim	RMSD	exp	sim	RMSD
-98,16	-93,86	4,3	-99,2	-	-
-99,51	-97,87	1,64	-100,26	-100,15	0,11
-116,13	-116,99	0,86	-102,42	-103,04	0,63
-116,13	-118,7	2,57	-104,2	-104,4	0,2
			-106,85	-105,18	1,67
			-117,39	-118,6	1,21
			-117,39	-119,19	1,8
			-117,39	-118,49	1,1
			-118,96	-120,58	1,63

4.3 The structure of $\text{Na}_3[\text{Al}(\text{L-lactate}_3)_2] \cdot 6 \text{H}_2\text{O}$ crystallized from Lohtragon® Al 250 – a commercial cement adjuvant

This work is the result of a cooperation between the Inorganic Chemistry III and I of the University of Bayreuth and Procter & Gamble Germany GmbH & CO Operations OHG Sulzbacher Str. 40 65824 Schwalbach/Taunus, *Chemistry – A European Journal* 2018, Copyright 2018 American Chemical society (*submitted*)

My contributions are:

- conception and main authorship of the article
- DFT+D calculations, including geometry optimization and NMR parameters
- evaluation of ^1H , ^{13}C ^{27}Al and ^{23}Na ssNMR measurements and calculations
- final structure solution of the compound

The other authors contributions are:

- synthesis of the compound
- structure solution of the heavy atoms from single crystal using XRD
- ^1H , ^{13}C ^{27}Al and ^{23}Na ssNMR measurements
- Additional characterization

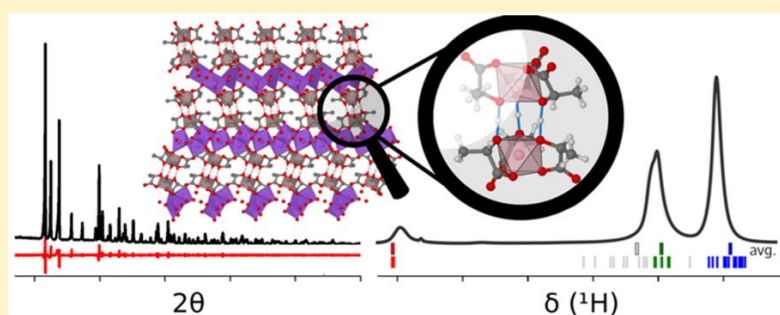
Structure of $\text{Na}_3[\text{Al}(\text{L-Lactate})_3]_2 \cdot 6\text{H}_2\text{O}$ Crystallized from Lohtragon AL 250—A Commercial Cement Adjuvant

Dominik Greim,[†] Wolfgang Milius,[‡] Beate Bojer,[†] Renée Siegel,[†] Josef Breu,^{*,‡} and Jürgen Senker^{*,†}

[†]Inorganic Chemistry III and Northern Bavarian NMR Centre, University of Bayreuth, Universitätsstraße 30, 95440 Bayreuth, Germany

[‡]Inorganic Chemistry I, University of Bayreuth, 95440 Bayreuth, Germany

S Supporting Information



ABSTRACT: Aqueous aluminum(III) solutions at medium pH are used for industrial applications such as cement adjuvants. The necessary high Al^{3+} concentrations are achieved by using complexing ligands, such as lactic acid, to prevent precipitation. Here, we grew crystals from commercially available neutralized aluminum lactate solutions to derive an understanding of the underlying aluminum lactate chemistry. Using X-ray diffraction in combination with multinuclear NMR spectroscopy and quantum mechanical calculations, we found that the crystals have a stoichiometry of $\text{Na}_3[\text{Al}(\text{L-lactate})_3]_2 \cdot 6\text{H}_2\text{O}$ and consist of negatively charged $[\text{Al}(\text{L-lactate})_3]_2^{3-}$ bis-clusters. The remarkable stability of these clusters is achieved by linking both $\text{Al}(\text{L-lactate})_3$ subunits via three very short symmetrical hydrogen bonds between the α -hydroxy groups with half of them being deprotonated. The trends for both the ^{27}Al chemical shift and the spin–spin relaxation for the Lohtragon-type solutions as a function of pH suggest the bis-cluster to be the origin for the stability of highly concentrated Al^{3+} solutions at medium pH. It may inspire alternative synthesis routes to extend the stability of concentrated Al^{3+} solutions over a broad pH range in the future.

INTRODUCTION

Aluminum(III) is known to feature a versatile chemistry in aqueous solutions. At medium pH and concentrations of up to 10^{-4} mol/L monomeric species are stable.¹ With increasing pH and concentration, condensation occurs, leading to a variety of oligomeric species.² By control of the synthesis conditions, a broad range of oligomeric aluminum clusters have been isolated, including brucite-like $\text{Al}_3(\text{OH})_4^{5+}$ clusters, octameric Al_8 species, the Al_{13} -containing Baker–Figgins–Keggin isomers, and Al_{30} structures, which can even be surface-modified.^{3–5}

For industrial applications, usually stable solutions with high Al^{3+} content are required. One possibility to increase the solubility is to complex Al^{3+} , for which a broad variety of ligands can be used.^{1,6} In this context, α -hydroxy carboxylic acids, with their cheapest and most widely used representative being lactic acid, are commonly employed in several industrial applications such as hair styling, skin treatment, super-absorbers, and cement adjuvants.^{7–12} In solution a variety of aluminum lactate complexes with varying compositions,

configurations, and protonation degrees coexist as a function of concentration and pH.⁶ These include mixed species where lactate is gradually replaced by hydroxyl ions and water molecules.⁶ To be able to tune the solution to the requirement of the targeted application, detailed knowledge about the predominant aluminum species is essential. In solution the identification of these species is limited due to dynamic ligand exchange, averaging configurations and composition. Therefore, analyzing precipitates is an alternative. This strategy, for example, led to the crystal structure of $\text{Al}(\text{L-lactate})_3$,¹³ which crystallizes from solution if the pH is 4 or lower¹⁴ as the hydroxyl groups become acidic upon complexing the aluminum ions.⁶ Up to now, the predominant species at medium pH have not been identified either in solution or in the solid state.

Received: March 24, 2019

Revised: June 20, 2019

Published: June 24, 2019

Here we grew crystals from a commercially available neutralized ($4 < \text{pH} < 6$) Al-lactate solution (Lohtragon AL 250), with high Al content to develop a better understanding for the aluminum lactate chemistry under conditions relevant for most applications. Although structures of solids are commonly solved via X-ray diffraction (XRD), this can be challenging if light atoms such as hydrogen atoms are involved. To compensate for their weak scattering forces, often solid-state nuclear magnetic resonance (ssNMR) experiments are used.^{15,16} In particular, for hydrogen atoms, they provide versatile tools to resolve position, connectivities, and information about hydrogen bonding.^{17–20} Ultrafast magic angle spinning (MAS) and homonuclear decoupling meanwhile allow for remarkable resolution.^{21–23} Additionally, dipolar recoupling experiments enable probing distances up to 15 Å.^{24–26} By a comparison of the experimental observables to their simulated counterparts derived from various structure models using ab initio methods, crystal structures could even be solved without the need for diffraction experiments.²⁷

The precipitate obtained for this study was characterized by single-crystal XRD, calculations at the DFT level, multinuclear (^1H , ^{13}C , ^{23}Na , ^{27}Al) NMR spectroscopic experiments as a function of temperature, TG, and IR spectroscopy. Comparing these results with ^{13}C and ^{27}Al NMR spectra of the Lohtragon solution allows for probing the predominant Al species in aqueous environment, at high Al content and medium pH.

■ EXPERIMENTAL SECTION

Commercially available Lohtragon AL 250 solution was crystallized by placing it in an atmosphere saturated with tetrahydrofuran as antisolvent for 7 days.

The single-crystal X-ray diffraction experiment was carried out on a STOE IPDS II instrument (Mo $K\alpha$ radiation) equipped with a Ge(111) monochromator under ambient conditions. The crystal with an approximate size of 0.2 mm \times 0.2 mm \times 1.5 mm was mounted on a glass tip with glue. Data collection, indexing, space group determination, data reduction, and reconstruction of reciprocal space layers were performed with the software package X-Area (STOE). For structure solution and refinement, the software packages SHELXS²⁸ and SHELXL²⁹ were used. All non-hydrogen atoms were refined with anisotropic displacement parameters. The hydroxy group hydrogen atoms were placed via modeling and subsequent geometry optimization at the DFT level (see below) The PXRD pattern was recorded on a STOE STADI P diffractometer with Cu $K\alpha$ radiation using a Dectris MythenIK detector. The Pawley fit was done with the TOPAS v5.0 Academic software package.³⁰

Attenuated total reflectance IR spectra were recorded in the range 400–4000 cm^{-1} with a resolution of 4 cm^{-1} on a Jasco FT/IR-6100 spectrometer with a PIKEGLADIATR accessory. Thermogravimetric analysis (TGA) was carried out on a Netzsch STA 499C instrument in air.

The ^1H and ^{13}C NMR experiments were performed on a Bruker Avance III HD spectrometer operating at a proton frequency of 600.1 MHz (150.9 MHz for ^{13}C). The ^{13}C MAS NMR spectra were obtained using a 1.9 mm triple-resonance probe at a spinning rate of 12.5 kHz with a ramped cross-polarization (CP) experiment, where the nutation frequency ν_{nut} on the proton channel was varied linearly by 50%. The corresponding ν_{nut} on the ^{13}C channel and the contact time were adjusted to 70 kHz and 3 ms, respectively. During acquisition, proton broad-band decoupling was applied using a spinal-64 sequence with $\nu_{\text{nut}} = 70$ kHz. The ^1H MAS spectrum was acquired after a 90° pulse length of 1.5 μs with a recycle delay of 5.0 s using a 1.3 mm double-resonance probe at a spinning rate of 62.5 kHz. Both ^1H and ^{13}C spectra are referenced indirectly with respect to tetramethylsilane (TMS) using adamantane as a secondary reference.²⁷ Al solid-state MAS NMR experiments were recorded

on a Bruker Avance II 300 spectrometer at a rotation frequency of 10 kHz using a 4 mm triple-resonance probe operating at a frequency of 78.2 MHz for ^{27}Al . ^{27}Al liquid-state NMR experiments were acquired on a Bruker Avance III HD spectrometer at a B_0 field of 9.4 T corresponding to an ^{27}Al frequency of 104.3 MHz. The samples were spun at a MAS of 2.0 kHz using a 4 mm double-resonance probe. For all ^{27}Al experiments, a small pulse flip angle of $\sim 10^\circ$ was employed for exciting the central transition selectively and for ensuring the integrability of the resulting ^{27}Al MAS NMR spectra. The chemical shift was referenced to an acidic solution of aluminum chloride hexahydrate adjusted to a pH of 0 and a concentration of 0.01 mol/L. ^{23}Na NMR experiments were recorded on a Bruker Avance II 300 spectrometer using a static double-resonance probe operating at a frequency of 79.4 MHz. The Hahn echo spectra were acquired using 90 and 180° pulses of 8.4 and 16.8 μs , respectively, and an interpulse delay of 20 ms. During acquisition, proton broad-band decoupling was applied using a CW sequence with $\nu_{\text{nut}} = 50$ kHz. The ^{23}Na chemical shift was referenced to a saturated solution of NaNO_3 . The liquid ^1H spectrum of the Lohtragon solution was acquired on a Bruker Avance III HD instrument using a 5 mm CryoProbe Prodigy BBO 500 S2 apparatus at a field of 11.7 T.

The DFT-D calculations were carried out using the CASTEP 8.0 code.³¹ The GGA with the PBE functional was used.³² A plane-wave basis set with an energy cutoff of 800 eV was applied, and the electrons were represented by ultrasoft pseudopotentials. k points were distributed using a Monkhorst–Pack-grid³³ with spacing of 0.03 Å⁻¹. Semiempirical dispersion correction as proposed by Grimme³⁴ was employed. For the geometry optimization the symmetry was restricted, and the convergence tolerances of energy, maximum force, and maximum displacement were 2.0×10^{-5} eV per atom, 5.0×10^{-2} eV Å⁻¹, and 1.0×10^{-3} Å⁻¹, respectively. The allowed stress tolerance was 0.1 GPa. NMR parameters were calculated using the GIPAW approach.³⁵ All chemical shieldings (δ_{iso}) were referenced and transformed into chemical shift values using the formula $\sigma_{\text{calc}} = \sigma_{\text{ref}} - \delta_{\text{iso}}$. The reference values σ_{ref} were adjusted to $\sigma_{\text{ref}}(^1\text{H}) = 29.63$ ppm, $\sigma_{\text{ref}}(^{13}\text{C}) = 185.4$ ppm, $\sigma_{\text{ref}}(^{23}\text{Na}) = 573.2$ ppm, and $\sigma_{\text{ref}}(^{27}\text{Al}) = 544.3$ ppm by using a linear trend correlation between the observed and calculated shift values for $\text{Na}_3[\text{Al}(\text{L Lactate})_3]_2 \cdot 6\text{H}_2\text{O}$.

■ RESULTS AND DISCUSSION

Samples were obtained by antisolvent crystallization of the purchased Lohtragon AL 250 solution (from Dr. Paul Lohmann GmbH KG, Hauptstrasse 2, 31860 Emmerthal, Germany, www.lohmann-chemikalien.de). This led to a phase-pure precipitate in an almost quantitative yield. The single-crystal XRD structure solution results in a trigonal cell with space group $P3_2$ in a hexagonal setting with lattice parameters $a = 9.023(1)$ Å and $c = 35.309(7)$ Å (for more details see Tables S1 and S2). The asymmetric unit contains two aluminum, three sodium, and six oxygen sites as well as six L-lactate molecules. All atoms are placed on Wyckoff site 3a, which multiplies the content of the asymmetric unit by 3 to fill the unit cell. For the hydrogen atoms attached to the oxygen atoms of the α -hydroxy groups and the oxygen atoms not covalently bound to the L-lactate molecules, no unambiguous solution could be obtained on the basis of the single-crystal diffraction data. Depending on the protonation degree of the lactate units, part of the oxygen atoms not directly related to the L-lactate molecules are either water molecules or hydroxy ions to compensate the remaining charge. We attribute this uncertainty to dynamic disorder within the water/hydroxy substructure, which also explains the high R values of the crystal structure solution. The radiographic purity was proven by powder XRD (PXRD). All reflexes could be unambiguously indexed according to the hexagonal metric obtained by the single-crystal diffraction data, and the intensity pattern matches

the predicted one (Figure S1). The subsequent Pawley refinement resulted in a R_p value of 4.0 and lattice parameters $a = 8.9895(1)$ Å and $c = 33.8959(3)$ Å. In order to compensate for the loss of information, additional multinuclear (^1H , ^{13}C , ^{23}Na , and ^{27}Al) ssNMR measurements and DFT calculations for possible structure models were carried out.

The ^{13}C MAS ssNMR cross-polarization (CP) spectrum (Figure 1 and Table S4) shows three distinct signal groups for

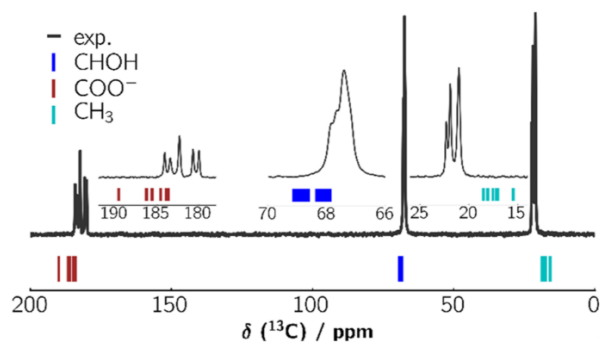


Figure 1. ^{13}C CP MAS NMR spectrum of $\text{Na}_3[\text{Al}(\text{L-lactate})_3]_2 \cdot 6\text{H}_2\text{O}$ measured at 12.5 kHz spinning speed at a field of 9.4 T with DFT calculated shifts sorted by chemical groups (bottom bars).

the three different chemical units of the L-lactate ligands. In the case of the carboxylate groups these are split into five resonances. The methyl groups only show three resonances, while for the CH groups one broader signal with a downfield shoulder is observed. The five carboxylate resonances agree with the six lactate molecules within the asymmetric unit. In particular, one resonance exhibits twice the intensity of the others. As the ^{13}C MAS NMR spectrum (Figure 1) was acquired using a cross-polarization sequence, we strictly limited a comparison of the intensities to the carboxylate groups. They exhibit similar environments leading to similar buildup rates for the intensities of each resonance. Derived intensity ratios are then still representative for the atomic ratios.³⁶ The smaller splitting for the resonances of the CHOH and CH_3 groups—again six resonances are expected from the single-crystal data—indicates that both groups are less sensitive to the packing of the Al-lactate complexes.

In accordance with the results of the XRD structure solution the ^{27}Al MAS NMR spectrum consists of two resonances (Figure 2). Since ^{27}Al is a spin 5/2 nucleus, both signals exhibit the typical shape of second-order quadrupolar broadening.³⁷ Refinement of the spectrum (Figure 2 and Table S5) yields the characteristic parameters for the chemical shift (δ_{iso} 24.3/25.6 ppm) and quadrupolar interaction ($C_q = 2.7/2.2$ MHz as well as $\eta_q = 0.64/0.63$). The isotropic shifts are similar to the those observed for $\text{Al}(\text{L-lactate})_3$ (Figure S2 and Table S6).⁶ This corroborates that for each aluminum within the asymmetric unit three L-lactate molecules coordinate in a bidentate fashion with one oxygen of the carboxylate groups and the oxygen of the CHOH groups, resulting in an octahedral coordination.³⁸ In comparison to $\text{Al}(\text{L-lactate})_3$, this coordination is significantly less distorted, as the quadrupolar coupling constants of the Lohstragon precipitate are smaller by roughly 50% (Table S6 and Figure S2).

The ^1H MAS NMR spectrum (Figure 3 and Table S7) shows signals in the expected regions for methyl groups (δ_{iso} 1.3 ppm, 18.8) and CHOH units in α position to the carboxy

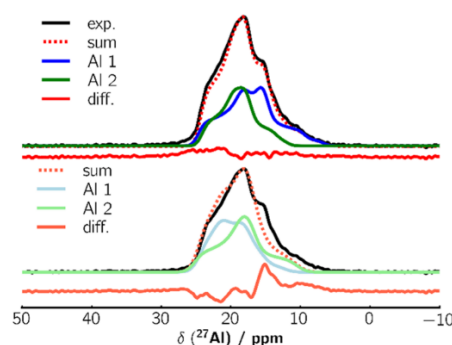


Figure 2. ^{27}Al MAS NMR spectrum of $\text{Na}_3[\text{Al}(\text{L-lactate})_3]_2 \cdot 6\text{H}_2\text{O}$ measured at 25 kHz spinning speed at a field of 7.1 T together with a deconvolution with two Al sites (top) and the theoretical spectrum from DFT calculations (bottom). The line broadening for the latter is 150 Hz.

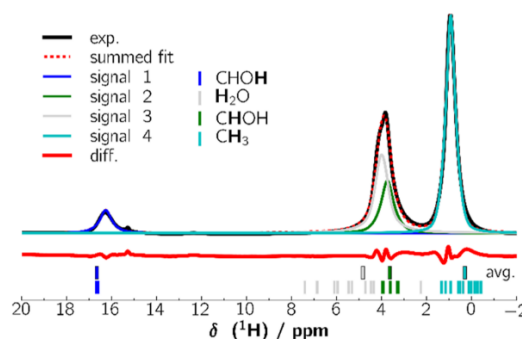


Figure 3. Deconvolution of the ^1H MAS NMR spectrum of $\text{Na}_3[\text{Al}(\text{L-lactate})_3]_2 \cdot 6\text{H}_2\text{O}$ measured at 40 kHz spinning speed at 11.7 T with DFT calculated shifts color-coded according to the chemical species and their averages (bottom bars). The middle bars exhibit the result of averaging the signals for the individual proton types according to a fast reorientational dynamics of the water molecules.

groups (δ_{iso} 4.4 ppm, intensity 5.6). The deconvolution of the ^1H MAS NMR spectrum reveals an additional resonance at 4.0 ppm (intensity 11.4) typical for water. This is in line with the strong absorption band in the infrared spectrum (IR) at about 3500 cm^{-1} (Figure S3). Additionally, a low-field signal at 16.6 ppm (intensity 3.3) is observed which can only be explained by protons involved in exceptionally strong hydrogen bonds. Due to the strong hydrogen bonds, the OH stretching vibration band is shifted into the fingerprint region within the IR spectrum (Figure S3).¹⁶

Taking into account the chemical shift of the signal at 16.3 ppm as well as its intensity, three very strong hydrogen bonds occur within the asymmetric unit. For the heavy-atom substructure model, two $\text{Al}(\text{L-lactate})_3$ cluster are facing each other via the alcohol groups. As a consequence, three of these units have to be deprotonated to be able to form an O–H–O motif with an angle close to 180° and an O–O distance of 2.47 Å, in line with the proposed very strong hydrogen bonds. In comparison to $\text{Al}(\text{L-lactate})_3$, where the alcohol function exhibits a hydrogen bond to a carboxylate group of a neighboring complex, the ^1H NMR resonance of the O–H–O units of the Lohstragon precipitate features a low-field shift of ~ 4 ppm. Thus, the Lohstragon precipitate consists of $[\text{Al}(\text{L-lactate})_3]_2$ bis-clusters where two $\text{Al}(\text{L-lactate})_3$ complexes are linked (Figure 4). Since no other acidic protons have been

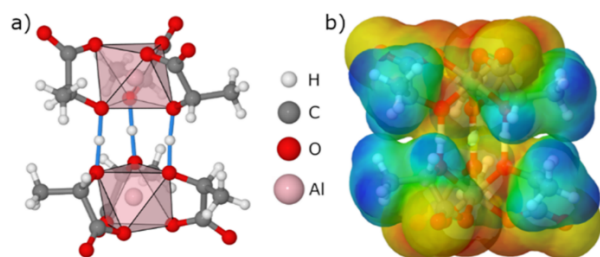


Figure 4. (a) Illustration of the binuclear $[\text{Al}(\text{L-lactate})_3]_2^{3-}$ with short symmetric hydrogen bonding with O–H–O distances of 2.47 Å (solid blue lines). (b) Electrostatic potential at 60% vdW surface. Blue corresponds to -0.35 and red to -0.75 .

observed in the ^1H MAS NMR spectrum, these bis-clusters bear a negative charge of 3. This negative charge is compensated by the three sodium ions within the asymmetric unit.

The six oxygen atoms not related with the L-lactate molecules thus represent water molecules, which is in line with the intensity of 11.6 derived for the water resonance at 4.0 ppm. This allows to specify the stoichiometry of the asymmetric unit as $\text{Na}_3[\text{Al}(\text{L-lactate})_3]_2 \cdot 6\text{H}_2\text{O}$. From these six water molecules only four are bound directly to sodium ions. Two additional water molecules are incorporated via hydrogen bonds to either the water substructure or the carboxylate groups of the bis-clusters. These two can be removed by heating to 100 °C, as shown by the mass loss of 4.8% in the thermogravimetric experiment (Figure S4) corresponding to two water molecules, while the other four water molecules are tightly bound and are removed only upon decomposition of the material.

To corroborate the resulting structure model, quantum mechanical calculations on the DFT level were performed, allowing all atomic positions and unit cell parameters to relax. The hydrogen atoms bound to water were placed into the structure model on the basis of difference Fourier analysis prior to geometry optimization. The resulting unit cell dimensions show only small differences in comparison to the values obtained by XRD. The a and c axes both are $\sim 2\%$ shorter, which decreases the overall volume of the cell by 6% (Table S8). This trend is typical for the functional used and the semiempirical dispersion correction employed. In accordance with the observed unit cell reduction, the bond lengths are also somewhat shorter. We observed a maximal deviation of 3%, with most of the distances reduced by less than 2% in comparison to the experimental data (Table S8) and with the expected error margin of the method being below 5%.³⁹

Larger deviations are observed within the sodium water substructure. This is mainly a consequence of the uncertainty of placing the hydrogen positions on the basis of the XRD data. Since all sodium atoms are in a mixed-octahedral coordination with the oxygen atoms of water and carboxylate groups, relaxation within the hydrogen substructure has an immediate effect on e.g. the sodium–oxygen distances. In this context the largest deviation between experiment and calculation amounts to 5% (Table S9). This deviation correlates with the high thermal displacement parameters of the sodium and water positions (Table S3). In contrast, complete protonation of the hydroxy groups, while compensating the charge with OH^- in the interlayer space, did not lead to a stable structure.

The calculated NMR parameters for the ^{13}C and ^{27}Al MAS ssNMR spectra are in good agreement with the experimental data. The typical ^{13}C shift ranges for the carboxylate, CHOH, and methyl groups of the lactate molecules are reproduced within the expected error margin of the DFT calculation. The spread between the individual resonances of the characteristic chemical units is largest for the carboxylates and decreases over the methyl units to the CHOH groups. This is in line with the trend of the experimental data and matches the packing scheme of the bis-clusters. While the carboxylate groups on each face of the bis-cluster are linked to the bridging sodium–water substructure differently (Figure 4), the methyl groups connect to other bis-clusters via only weak van der Waals interactions and the CHOH units are embedded within the bis-cluster itself. The difference in the two $\text{Al}(\text{L-lactate})_3$ subunits is also reflected in the two sets of characteristic ^{27}Al NMR parameters (δ_{iso} , C_Q , and η_Q) for the two Al sites within the asymmetric unit (Table S5). The deviations in the C_Q and η_Q values are on the same order of magnitude as those observed for $\text{Al}(\text{L-lactate})_3$ (Table S6) and other materials^{40–42} and thus represent the achievable accuracy.

The DFT calculated values for NMR parameters of the hydrogen atoms reproduce the strong experimentally observed downfield shift in the ^1H MAS ssNMR spectrum (Figure 3) for the strong $\text{HC-O}\cdots\text{H}\cdots\text{O-CH}$ hydrogen bonds between the $\text{Al}(\text{L-lactate})_3$ subunits almost perfectly. This is also true for the proton resonances of the CHOH units. In contrast, the calculations yield broad chemical shift ranges for the signals of the water and methyl groups, while the corresponding experimental values show only one resonance for each group. Nevertheless, the average of the calculated shifts matches the experimental data very well. This effect is most likely a consequence of fast motional processes involving both the water molecules and the methyl groups and thus proves the dynamic disorder within the sodium–water substructure proposed earlier.

The disorder is also reflected in the much narrower line shape of the room-temperature ^{23}Na ssNMR spectrum in comparison to that measured at 93 K (Figure 5). While the

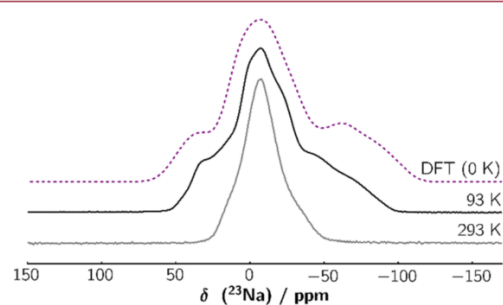


Figure 5. ^{23}Na wide-line Hahn echo NMR spectrum of $\text{Na}_3[\text{Al}(\text{L-lactate})_3]_2 \cdot 6\text{H}_2\text{O}$ measured at 293 K (gray) and 93 K (black) at a field of 7.1 T and the DFT simulated spectrum (dashed purple) corresponding to 0 K.

former mainly consists of one Gaussian-type resonance, the latter deconvolutes into three individual resonances with δ_{iso} , C_Q and η_Q between 1.0 and 3.5 ppm, 1.0 and 2.2 MHz, and 0.25 and 0.75, respectively. These parameters match the DFT calculated values for the crystal structure exceptionally well (Figure 5 and Table S10). This on the one hand supports the structure solution and on the other hand suggests that the

orientational motion of the water molecules slows down sufficiently to reach the slow-motion limit ($\tau > 10^{-3}$ s) at 93 K.

To determine the dominating cluster in Lohtragon-type solutions, ^{13}C and ^{27}Al liquid-state NMR spectra for these solutions were acquired and compared to the ssNMR spectra (Figures 1–3 and Figures S2 and S5) obtained for $\text{Na}_3[\text{Al}(\text{L-lactate})_3]_2 \cdot 6\text{H}_2\text{O}$ and $\text{Al}(\text{L-lactate})_3$. The latter was obtained by crystallization from $\text{Al}(\text{OH})_3$ solutions adjusted to pH 3 by adding L-lactic acid. The ^{13}C liquid NMR spectrum of the Lohtragon-type solution shows three single resonances typical for the carboxy, CHOH, and methyl groups when a lactate molecule is coordinated to aluminum in a bidentate fashion (Figure S5). Since this is true for both the $[\text{Al}(\text{L-lactate})_3]_2^{3-}$ and $\text{Al}(\text{L-lactate})_3$ cluster, ^{13}C experiments are not able to distinguish between both scenarios. The most characteristic NMR spectroscopic feature to probe the existence of the bis-cluster is the proton resonance of the strong O–H–O hydrogen bond at about 16 ppm (Figure 3). Unfortunately, in aqueous solution the chemical exchange between water and the bis-cluster is fast on the NMR time scale, leading to one average signal close to the water resonance at 4.8 ppm (Figure S6).

The ^{27}Al liquid-state NMR spectrum (Figure 6, blue line) of the Lohtragon-type solution shows one Lorentzian-type

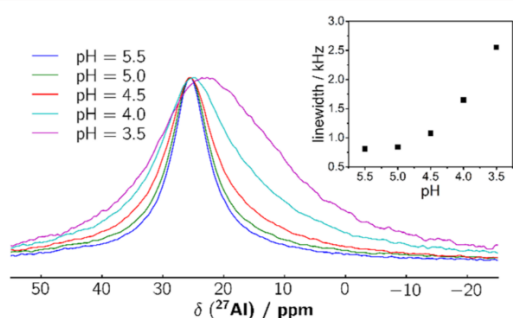


Figure 6. ^{27}Al liquid-state NMR of Lohtragon AL 250 solution with varying pH and dependence of the line width of the ^{27}Al NMR signal on pH.

resonance with an isotropic shift of 28.2 ppm and a line width of 808 Hz. Both the isotropic shift and line width remain roughly constant down to pH 4.5. Toward lower pH this resonance starts to shift to high field and becomes significantly broader. For pH 3.5 an isotropic shift of 26.8 ppm and a line width of 2532 Hz was observed. This trend suggests that for pH values above 4.5 a different aluminum cluster is predominant in the solution in comparison to that for the pH region around 3. As $\text{Al}(\text{L-lactate})_3$ crystallizes from aluminum L-lactate solutions adjusted to a pH in this region,^{13,14,43} we expect the charge-neutral $\text{Al}(\text{L-lactate})_3$ monocluster to be the predominant species within the lower pH region. For the same reason we attribute the negatively charged $[\text{Al}(\text{L-lactate})_3]_2^{3-}$ bis-cluster to the pH region above 4.5. Between these pH values a continuous crossover between both species takes place. We support this assignment by two further observations.

First, the isotropic ^{27}Al NMR shifts of 25.6/24.3 ppm determined for both Al sites within $\text{Na}_3[\text{Al}(\text{L-lactate})_3]_2 \cdot 6\text{H}_2\text{O}$ (Figure 2) are shifted to low field in comparison to those (Figure S2) of $\text{Al}(\text{L-lactate})_3$ (24.6/22.9 ppm), matching the shift change of 1.4 ppm within the Lohtragon-type solutions

with decreasing pH (Figure 6). Second, the trend of the line width as a function of pH suggests that the Al clusters predominant for a pH above 4.5 and below 3.5 differ by a factor of 2 for the quadrupolar coupling constant C_Q with the larger C_Q being expected for lower pH. This is in line with C_Q values derived for the $\text{Al}(\text{L-lactate})_3$ monocluster ($4.6 < C_Q < 5.2$ MHz) and for the $[\text{Al}(\text{L-lactate})_3]_2^{3-}$ bis-cluster ($2.2 < C_Q < 2.8$ MHz).

This analysis is based on the assumption that the spin–spin relaxation is driven by the quadrupolar interaction (eq S1), that the reorientational dynamics is in the fast motion limit as is typical for liquids, and that the viscosity of the liquid does not change significantly.⁴⁴ In this case the line width is proportional to the square of C_Q (for more details refer to eqs S1 and S2 and Table S12). This is in line with both the experimental and DFT calculated C_Q for $\text{Al}(\text{L-lactate})_3$ monoclusters which is roughly 2–3 times larger (Tables S4, S5, and S12), increasing the line width by a factor of 4–9.

CONCLUSION

In this work $\text{Na}_3[\text{Al}(\text{L-lactate})_3]_2 \cdot 6\text{H}_2\text{O}$ was crystallized from Lohtragon-type solutions and characterized by single-crystal and powder X-ray diffraction, DFT calculations, and ssNMR and infrared spectroscopy as well as TG experiments. $\text{Na}_3[\text{Al}(\text{L-lactate})_3]_2 \cdot 6\text{H}_2\text{O}$ crystallizes in a hexagonal metric with lattice parameters of $a = 9.0228(1)$ Å and $c = 35.309(7)$ Å and a space symmetry of $P3_2$. The asymmetric unit contains two aluminum, three sodium, six water, and six L-lactate molecules. Each of the two Al^{3+} ions is coordinated octahedrally by three L-lactate ligands in a bidentate manner via the carboxylate and hydroxyl groups. They form two $\text{Al}(\text{L-lactate})_3$ subunits which are connected via the lactate's hydroxyl groups. From the six hydroxyl groups, three are deprotonated, giving rise to three short and symmetrical hydrogen bonds ($\text{HC}=\text{O} \cdots \text{H} \cdots \text{O}=\text{CH}$), resulting in the three times negatively charged bis-cluster $[\text{Al}(\text{L-lactate})_3]_2^{3-}$ (Figures 4 and 7a). $[\text{Al}(\text{L-lactate})_3]_2^{3-}$ is isostructural with $[\text{Al}(\text{Glycolate})_3]_2^{3-}$ as observed in $\text{Na}_3[\text{Al}(\text{Glycolate})_3]_2$.^{13,45}

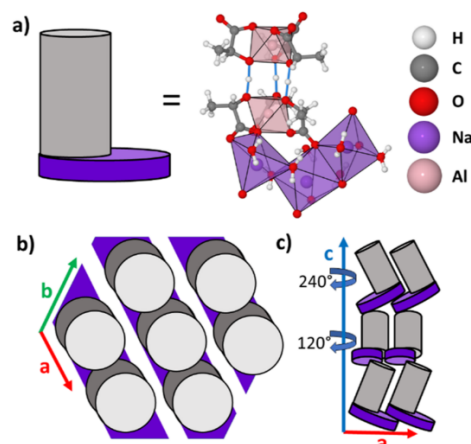


Figure 7. Representation of the packing scheme of $\text{Na}_3[\text{Al}(\text{L-lactate})_3]_2 \cdot 6\text{H}_2\text{O}$: (a) scheme for the asymmetric unit with $[\text{Al}(\text{L-lactate})_3]_2^{3-}$ complexes and the interlayer space with sodium and water; (b) hexagonal packing of the asymmetric units in the a/b plane; (c) packing along c with the 120° screw axis.

As the negative charge is mainly located at the carboxylate units at the terminating faces, the sodium ions preferentially coordinate to the oxygen of the carboxylate units to establish local charge compensation. The sodium ions are in turn linked by water molecules leading to strands of edge-sharing sodium oxygen octahedra (Figure 7a). The voids between the strands are occupied by additional crystal water loosely bound by hydrogen bonds forming water–sodium layers (Figure 7b and Figure S7). At room temperature the water molecules exhibit a pronounced dynamic disorder. The bis-clusters are sandwiched between two such layers and assemble into a two-dimensional hexagonal packing. Within the latter the van der Waals interaction between the methyl groups determines the packing density. Each layer is rotated by 120° and shifted by one-third of the length of the *c* axis toward the underlying layer (Figure 7c).

A comparison of ¹H, ¹³C, and ²⁷Al liquid-state NMR spectra of Lohtragon-type solutions allowed us to derive a better understanding of the Al-lactate chemistry at high aluminum content and medium pH. In a pH range between 4 and 6 the bis-cluster [Al(L-lactate)₃]₂³⁻ is expected to be the predominant species in solution, while at lower pH the bis-cluster is protonated and dissociates into charge-neutral Al(L-lactate)₃. Under even more acidic conditions Al(L-lactate)₁(H₂O)₄²⁺ and Al(L-lactate)₂(H₂O)₂²⁺ are formed.⁴³ This knowledge will be relevant for adapting Al lactate solutions at medium pH to the needs of various applications such as hair styling, skin treatment, superabsorbers, and cement adjuvants in the future.^{7–10,12,46}

■ ASSOCIATED CONTENT

■ Supporting Information

The Supporting Information is available free of charge on the ACS Publications website at DOI: 10.1021/acs.cgd.9b00394.

Crystallographic data of Na₃[Al(L-lactate)₃]₂·6H₂O including atomic coordinates and isotropic displacement parameters, PXRD pattern of Na₃[Al(L-lactate)₃]₂·6H₂O, ¹H, ¹³C, and ²⁷Al ssNMR with DFT calculations, ²⁷Al ssNMR of Al(L-lactate)₃, IR spectra of Al(L-lactate)₃ and Na₃[Al(L-lactate)₃]₂·6H₂O, TGA of Na₃[Al(L-lactate)₃]₂·6H₂O, experimental and DFT calculated cell constants and bond lengths, ²³Na ssNMR of Na₃[Al(L-lactate)₃]₂·6H₂O, ¹H and ¹³C liquid-state NMR of a Lohtragon-type solution, theory of spin–spin relaxation for quadrupolar nuclei in liquids, estimated ²⁷Al C_Q values from theory, and DFT calculated C_Q values for different Al(lactate) species (PDF)

Accession Codes

CCDC 1904297 contains the supplementary crystallographic data for this paper. These data can be obtained free of charge via www.ccdc.cam.ac.uk/data_request/cif, or by emailing data_request@ccdc.cam.ac.uk, or by contacting The Cambridge Crystallographic Data Centre, 12 Union Road, Cambridge CB2 1EZ, UK; fax: +44 1223 336033.

■ AUTHOR INFORMATION

Corresponding Authors

*E-mail for J.B.: Josef.Breu@uni-bayreuth.de.

*E-mail for J.S.: Juergen.Senker@uni-bayreuth.de.

ORCID

Josef Breu: 0000-0002-2547-3950

Jürgen Senker: 0000-0002-7278-7952

Author Contributions

The manuscript was written through contributions of all authors. All authors have given approval to the final version of the manuscript.

Notes

The authors declare no competing financial interest.

■ ACKNOWLEDGMENTS

The authors thank the chair of organic chemistry I of the University of Bayreuth for providing the NMR spectrometer for the ¹H liquid measurement.

■ REFERENCES

- (1) Akitt, J. W. *Multinuclear Studies of Aluminium Compounds. Prog. Nucl. Magn. Reson. Spectrosc.* **1989**, *21* (1–2), 1–149.
- (2) Jolivet, J.-P.; Henry, M.; Livage, J. *Metal Oxide Chemistry and Synthesis: From Solution to Solid State*; Wiley-Blackwell: 2000.
- (3) Perkins, C. K.; Eitrrheim, E. S.; Fulton, B. L.; Fullmer, L. B.; Colla, C. A.; Park, D.-H.; Oliveri, A. F.; Hutchison, J. E.; Nyman, M.; Casey, W. H.; et al. Synthesis of an Aluminum Hydroxide Octamer through a Simple Dissolution Method. *Angew. Chem.* **2017**, *129* (34), 10295–10298.
- (4) Abeyasinghe, S.; Unruh, D. K.; Forbes, T. Z. Surface Modification of Al₃₀ Keggin-Type Polyaluminum Molecular Clusters. *Inorg. Chem.* **2013**, *52* (10), 5991–5999.
- (5) Allouche, L.; Gérardin, C.; Loiseau, T.; Férey, G.; Taulelle, F. Al₃₀: A Giant Aluminum Polycation. *Angew. Chem., intensity Ed.* **2000**, *39* (3), 511–514.
- (6) Corain, B.; Longato, B.; Sheikh-Osman, A. A.; Bombi, G. G.; Maccà, C. Aluminium Carboxylates in Aqueous Solutions. Part 2. Metal Speciation in the Al^{III} – Lactate–OH[–] – H₂O System. *J. Chem. Soc., Dalton Trans.* **1992**, *1*, 169–172.
- (7) Klenk, A.; Hollenberg, D.; Hoeffkes, H. Hair Permanent-Waving Method and Aftertreatment Composition. EP0256462B1, 1987.
- (8) Mange, T.; Tober, B.; Schick, G.; Veeger, M.; Kamps, N. Aluminium Lactate as a Skin Protection Component. EP3148501A1, 2017.
- (9) Buchholz, F. L.; Graham, A. T. *Modern Superabsorbent Polymer Technology*; Wiley-VCH: 1998.
- (10) Wattebled, L.; Loick, C.; Harren, J.; Leininger, S. Water-Absorbing Polymer Having a High Absorption Rate. EP2699609B1, 2014.
- (11) Daniel, T.; Hagen, Y.; Riegel, U.; Hermeling, D.; Bruhns, S. Water-Absorbing Polymeric Particles and Method for the Production Thereof. WO2012052365A1, 2011.
- (12) Auvray, J.-M.; Kebli, F.; Lievin, M.; Benyhaia, K.; Wöhrmeyer, C. An Adjuvant for a Cement or a Refractory Concrete Composition, the Uses Thereof, and Cement and Refractory Concrete Compositions. EP3286156A1, 2016.
- (13) Giorgio Bombi, G.; Corain, B.; Sheikh-Osman, A. A.; Valle, G. C. The Speciation of Aluminum in Aqueous Solutions of Aluminum Carboxylates. Part I. X-Ray Molecular Structure of Al[OC(O)CH(OH)CH₃]₃. *Inorg. Chim. Acta* **1990**, *171* (1), 79–83.
- (14) Powell, A. K.; Heath, S. L. X-Ray Structural Analysis of Biologically Relevant Aluminium(III) Complexes. *Coord. Chem. Rev.* **1996**, *149*, 59–80.
- (15) van Koningsveld, H.; Venema, F. R. IUCr. Structure of the Hydrogen-Bonded Binuclear Complex Trisodium Trihydrogen Bis-[Tris(Glycolato)Aluminate(III)]. *Acta Crystallogr., Sect. C: Cryst. Struct. Commun.* **1991**, *47* (2), 289–292.
- (16) Steiner, T. The Hydrogen Bond in the Solid State. *Angew. Chem., intensity Ed.* **2002**, *41* (1), 48–76.
- (17) Seyfarth, L.; Senker, J. An NMR Crystallographic Approach for the Determination of the Hydrogen Substructure of Nitrogen Bonded Protons. *Phys. Chem. Chem. Phys.* **2009**, *11* (18), 3522.

- (18) Mesch, M. B.; Bärwinkel, K.; Krysiak, Y.; Martineau, C.; Taulelle, F.; Neder, R. B.; Kolb, U.; Senker, J. Solving the Hydrogen and Lithium Substructure of Poly(Triazine Imide)/LiCl Using NMR Crystallography. *Chem. - Eur. J.* **2016**, *22* (47), 16878–16890.
- (19) Mooibroek, S.; Wasylishen, R. E.; Dickson, R.; Facey, G.; Pettitt, B. A. Simultaneous Observation of Shielding Anisotropies and Quadrupolar Splittings in Solid State ^{133}Cs NMR Spectra. *J. Magn. Reson.* **1986**, *66* (3), 542–545.
- (20) Duer, M. J. *Introduction to Solid-State NMR Spectroscopy*; Blackwell: 2004.
- (21) Bryce, D. L.; Taulelle, F. NMR Crystallography. *Acta Crystallogr., Sect. C: Struct. Chem.* **2017**, *73* (3), 126–127.
- (22) Sakellariou, D.; Lesage, A.; Hodgkinson, P.; Emsley, L. Homonuclear Dipolar Decoupling in Solid-State NMR Using Continuous Phase Modulation. *Chem. Phys. Lett.* **2000**, *319* (3–4), 253–260.
- (23) Grüninger, H.; Armstrong, K.; Greim, D.; Boffa-Ballaran, T.; Frost, D. J.; Senker, J. Hidden Oceans? Unraveling the Structure of Hydrous Defects in the Earth's Deep Interior. *J. Am. Chem. Soc.* **2017**, *139* (30), 10499–10505.
- (24) Roos, M.; Mandala, V. S.; Hong, M. Determination of Long-Range Distances by Fast Magic-Angle-Spinning Radiofrequency-Driven ^{19}F – ^{19}F Dipolar Recoupling NMR. *J. Phys. Chem. B* **2018**, *122* (40), 9302–9313.
- (25) Linser, R.; Bardiaux, B.; Higman, V.; Fink, U.; Reif, B. Structure Calculation from Unambiguous Long-Range Amide and Methyl ^1H – ^1H Distance Restraints for a Microcrystalline Protein with MAS Solid-State NMR Spectroscopy. *J. Am. Chem. Soc.* **2011**, *133* (15), 5905–5912.
- (26) Hong, M.; Schmidt-Rohr, K. Magic-Angle-Spinning NMR Techniques for Measuring Long-Range Distances in Biological Macromolecules. *Acc. Chem. Res.* **2013**, *46* (9), 2154–2163.
- (27) Elena, B.; Pintacuda, G.; Mifsud, N.; Emsley, L. Molecular Structure Determination in Powders by NMR Crystallography from Proton Spin Diffusion. *J. Am. Chem. Soc.* **2006**, *128* (29), 9555–9560.
- (28) Sheldrick, G. M. IUCr. A Short History of SHELX. *Acta Crystallogr., Sect. A: Found. Crystallogr.* **2008**, *64* (1), 112–122.
- (29) Sheldrick, G. M. IUCr. Crystal Structure Refinement with SHELXL. *Acta Crystallogr., Sect. C: Struct. Chem.* **2015**, *71* (1), 3–8.
- (30) Coelho, A. A. *TOPAS-Academic*; Coelho Software: Brisbane, Australia, 2007.
- (31) Clark, S. J.; Segall, M. D.; Pickard, C. J.; Hasnip, P. J.; Probert, M. I. J.; Refson, K.; Payne, M. C. First Principles Methods Using CASTEP. *Zeitschrift für Krist. - Cryst. Mater.* **2005**, *220* (5/6), 567–570.
- (32) Perdew, J. P.; Burke, K.; Ernzerhof, M. Generalized Gradient Approximation Made Simple. *Phys. Rev. Lett.* **1996**, *77* (18), 3865–3868.
- (33) Monkhorst, H. J.; Pack, J. D. Special Points for Brillouin-Zone Integrations. *Phys. Rev. B* **1976**, *13* (12), 5188–5192.
- (34) Grimme, S. Semiempirical GGA-type Density Functional Constructed with a Long-range Dispersion Correction. *J. Comput. Chem.* **2006**, *27* (15), 1787–1799.
- (35) Charpentier, T. The PAW/GIPAW Approach for Computing NMR Parameters: A New Dimension Added to NMR Study of Solids. *Solid State Nucl. Magn. Reson.* **2011**, *40* (1), 1–20.
- (36) Martineau, C.; Senker, J.; Taulelle, F. NMR Crystallography. *Annu. Rep. NMR Spectrosc.* **2014**, *82*, 1–57.
- (37) MacKenzie, K. J. D.; Smith, M. E. *Multinuclear Solid-State NMR of Inorganic Materials*; Pergamon: 2002.
- (38) Haouas, M.; Taulelle, F.; Martineau, C. Recent Advances in Application of ^{27}Al NMR Spectroscopy to Materials Science. *Prog. Nucl. Magn. Reson. Spectrosc.* **2016**, *94–95*, 11–36.
- (39) Koch, W.; Holthausen, M. C. *A Chemist's Guide to Density Functional Theory*; Wiley: 2015.
- (40) Zhang, J.; Pilette, M.-A.; Cuevas, F.; Charpentier, T.; Mauri, F.; Latroche, M. X-Ray Diffraction and NMR Studies of $\text{Na}_{3-n}\text{Li}_n\text{AlH}_6$ ($n = 0, 1, 2$) Alanates Synthesized by High-Pressure Reactive Ball Milling. *J. Phys. Chem. C* **2009**, *113* (50), 21242–21252.
- (41) Lafond, A.; Rocquefelte, X.; Paris, M.; Guillot-Deudon, C.; Jouenne, V. Crystal Chemistry and Electronic Structure of the Photovoltaic Buffer Layer, $(\text{In}_{1-x}\text{Al}_x)_2\text{S}_3$. *Chem. Mater.* **2011**, *23* (23), 5168–5176.
- (42) Florian, P.; Veron, E.; Green, T. F. G.; Yates, J. R.; Massiot, D. Elucidation of the Al/Si Ordering in Gehlenite $\text{Ca}_2\text{Al}_2\text{SiO}_7$ by Combined ^{29}Si and ^{27}Al NMR Spectroscopy/Quantum Chemical Calculations. *Chem. Mater.* **2012**, *24* (21), 4068–4079.
- (43) Zhang, L.; Chan, J. C. C.; Eckert, H.; Hensch, G.; Hoyer, L. P.; Frischat, G. H. Novel Sol–Gel Synthesis of Sodium Aluminophosphate Glass Based on Aluminum Lactate. *Chem. Mater.* **2003**, *15* (14), 2702–2710.
- (44) Steigel, A.; Spiess, H. W. *Dynamic NMR Spectroscopy*; Springer Science & Business Media: 2012; Vol. 15.
- (45) Venema, F. R.; van Koningsveld, H.; Peters, J. A.; van Bekkum, H. Co-Operative Hydrogen Bonding with Short O...O Distances in a Binuclear Al^{III} –Glycolate Complex. *J. Chem. Soc., Chem. Commun.* **1990**, *0* (9), 699–700.
- (46) Wattedled, L.; Henn, M.; Teni, R. Superabsorbent Polymers with Rapid Absorption Properties and Process for Producing Same. EP2997051A1, 2014.

Supporting Information

for

The structure of $\text{Na}_3[\text{Al}(\text{L-Lactate})_3]_2 \cdot 6 \text{H}_2\text{O}$

crystallized from Lohtragon® AL 250 – a

commercial cement adjuvant

Dominik Greim,^[a] Wolfgang Milius,^[b] Beate Bojer,^[a] Renée Siegel,^[a] Josef Breu^{(b)} and Jürgen
Senker^{*(a)}*

^a Dominik Greim, Beate, Bojer, Dr. Renée Siegel, Prof. Dr. Jürgen Senker Chair for Inorganic Chemistry III,
University of Bayreuth 95440 Bayreuth (Germany)

^b Dr. Wolfgang Milius, Prof. Dr. Josef Breu Chair for Inorganic Chemistry I, University of Bayreuth
95440 Bayreuth (Germany)

Table of Contents

Table S1. Crystallographic data for the single-crystal X-ray diffraction structure solution of $\text{Na}_3[\text{Al}(\text{L-lactate})_3]_2 \cdot 6 \text{H}_2\text{O}$ obtained by direct methods.

Table S2. Fractional atomic coordinates and equivalent isotropic displacement parameters ($\text{\AA}^2 \times 10^3$) for $\text{Na}_3[\text{Al}(\text{L-lactate})_3]_2 \cdot 6 \text{H}_2\text{O}$. $U(\text{eq})$ is defined as one third of the trace of the orthogonalized U tensor given Table S3.

Figure S1. Powder X-Ray diffraction pattern of $\text{Na}_3[\text{Al}(\text{L-lactate})_3]_2 \cdot 6 \text{H}_2\text{O}$ with Pawley profile plot and difference plot. $R_p = 3.99$, $R_{wp} = 5.83$. cell axes after refinement were $a = 8.9895(1)$ & $c = 33.8959(3)$. The magenta line represents the simulated powder pattern according to the single-crystal X-ray diffraction structure solution (Tables S1 – S3). The lattice parameters have been adapted to the ones derived from the Pawley refinement.

Table S4. ^{13}C isotropic NMR shifts of $\text{Na}_3[\text{Al}(\text{L-lactate})_3]_2 \cdot 6 \text{H}_2\text{O}$ obtained from the observed ^{13}C MAS NMR spectrum depicted in Figure 1 and the comparison to results of DFT shift calculations.

Table S5. Comparison of the observed and calculated ^{27}Al NMR parameters (isotropic shift, CQ and η Q) for $\text{Na}_3[\text{Al}(\text{L-lactate})_3]_2 \cdot 6 \text{H}_2\text{O}$.

Figure S2. ^{27}Al MAS NMR spectrum of $\text{Al}(\text{L-lactate})_3$.

Table S6. Observed and DFT calculated isotropic chemical shifts and quadrupolar coupling parameters of ^{27}Al in solid $\text{Al}(\text{L-lactate})_3$. The deviation between the observed and the calculated values is most likely caused by thermal motion, which is not included in the calculation.

Table S7. Relevant refinement parameters of the deconvolution of the ^1H MAS NMR spectrum of $\text{Na}_3[\text{Al}(\text{L-lactate})_3]_2 \cdot 6 \text{H}_2\text{O}$. Labelling of signals according Figure 3

Figure S3. IR spectra of $\text{Na}_3[\text{Al}(\text{L-lactate})_3]_2 \cdot 6 \text{H}_2\text{O}$ and $\text{Al}(\text{L-lactate})_3$. The bands at 2450 cm^{-1} are artifacts from the measurement.

Figure S4. Thermogravimetric analysis of $\text{Na}_3[\text{Al}(\text{L-lactate})_3]_2 \cdot 6 \text{H}_2\text{O}$. The mass loss up to 200°C corresponds to two water molecules. Calculated wt% of Al_2O_3 and Na_2CO_3 is 27.27% of the initial mass. The total amount of lactate and water calculated from the sum formula amounts to 83.9%.

Table S8. Observed and calculated cell constants including the deviation between both values.

Table S9. Selected bond lengths as determined by XRD and after geometry optimization with DFT for $\text{Na}_3[\text{Al}(\text{L-lactate})_3]_2 \cdot 6 \text{H}_2\text{O}$. Deviations are given in absolute and relative values.

Table S10. ^{23}Na ssNMR refinement parameters of the deconvolution and DFT calculated NMR parameter for the isotropic chemical shift and the quadrupolar interaction for $\text{Na}_3[\text{Al}(\text{L-lactate})_3]_2 \cdot 6 \text{H}_2\text{O}$.

Figure S5. ^{13}C liquid-state NMR spectra of aqueous solutions of $\text{Na}_3[(\text{Al}(\text{L-lactate})_3)_2] \cdot 6 \text{H}_2\text{O}$ and ^{13}C CP MAS NMR of solid $\text{Na}_3[\text{Al}(\text{L-lactate})_3]_2 \cdot 6 \text{H}_2\text{O}$

Figure S6. ^1H liquid-state NMR of the Lohtragon-type solution.

Figure S6. ^1H liquid-state NMR of the Lohtragon-type solution.

Spin-Spin relaxation for quadrupolar nuclei in liquids

Table S11. Estimated CQ values derived from equations S1 and S2 and the observed linewidths for the resonances within the ^{27}Al liquid-state NMR spectra depicted in Figure 7. The temperature was set to 293 K, η_Q to 0.65 and an viscosity of 100 mPas was used. The viscosity has been adjusted to fit the Coupling observed in the solids and is overestimated by a factor of $\sim 2-3$ indicating that CQ is not the only influencing factor on the relaxation. The coupling doubles between pH 5.5 and 3.5.

Table S12. Calculated ^{27}Al NMR parameters of isolated $\text{Al}(\text{L-Lactate})_3$, $\text{Al}(\text{L-Lactate})_3$, $\text{Al}(\text{L-Lactate})_3$, and the binuclear $[\text{Al}(\text{L-Lactate})_3]_2$ complex.

4. Publications

Table S1. Crystallographic data for the single-crystal X-ray diffraction structure solution of $\text{Na}_3[\text{Al}(\text{L-lactate})_3]_2 \cdot 6 \text{H}_2\text{O}$ obtained by direct methods.

Radiation	Mo-K α
Formula	$\text{Na}_3 \text{Al}_2 \text{C}_{18} \text{H}_{39} \text{O}_{24}$
<i>M</i> (g/mol)	762.42
Z, calculated density (g/cm ³)	3, 1.526
Crystal Size / mm ³	0.19 x 0.16 x 0.12
Absorption coefficient	0.219 mm ⁻¹
No. of Reflections	14591
No. of Reflections (<i>I</i> / σ > 2.0)	5791
T / K	293
θ range / °	2.61-25.72
Completeness to theta = 25.72°	96.6 %
Crystal System	Trigonal
Space Group	<i>P</i> 3 ₂
a,b / Å	9.0228
c / Å	35.309
Goodness of Fit	1.019
<i>R</i> _p	0.0860
<i>R</i> _p (<i>I</i> / σ > 2.0)	0.0680
<i>wR</i> _p	0.1467
<i>wR</i> _p (<i>I</i> / σ > 2.0)	0.1354
Data / restraints / parameters	5791 / 16 / 424
Refinement method	Full-matrix least-squares on F ²
Residual electron density (RMS)	0.123

Table S2. Fractional atomic coordinates and equivalent isotropic displacement parameters ($\text{\AA}^2 \times 10^3$) for $\text{Na}_3[\text{Al}(\text{L-lactate})_3]_2 \cdot 6 \text{H}_2\text{O}$. $U(\text{eq})$ is defined as one third of the trace of the orthogonalized U tensor given Table S3.

site	x	y	z	U(eq)
Al1	0.2877(2)	0.18806(19)	0.19756(4)	0.0270(3)
Al2	0.4701(2)	0.26631(2)	0.32051(4)	0.0271(3)
Na1	-0.3210(3)	-0.1167(3)	0.12161(6)	0.0318(5)
Na2	-0.5737(3)	-0.4923(3)	0.06311(6)	0.0337(5)
Na3	-0.4782(3)	-0.8568(3)	0.08645(6)	0.0443(6)
O1	0.6931(5)	0.3328(5)	0.33837(10)	0.0336(9)
O2	0.5880(5)	0.4280(5)	0.28205(10)	0.0301(8)
O3	0.9701(5)	0.52971(5)	0.33161(11)	0.0392(9)
O4	0.3794(5)	0.0947(5)	0.35965(10)	0.0338(9)
O5	0.4417(5)	0.0794(5)	0.28956(10)	0.0306(8)
O6	0.3131(5)	-0.17121(6)	0.37468(12)	0.0415(10)
O7	0.4593(5)	0.4165(5)	0.35834(9)	0.0297(8)
O8	0.2591(5)	0.2386(5)	0.30484(9)	0.0311(8)
O9	0.26879(5)	0.4589(5)	0.39017(10)	0.0333(9)
O10	0.3044(5)	0.3586(5)	0.16214(10)	0.0313(8)
O11	0.5011(5)	0.3692(5)	0.21484(10)	0.0308(8)
O12	0.4945(5)	0.5937(5)	0.13180(10)	0.0339(9)
O13	0.0635(5)	0.0392(5)	0.17842(10)	0.0315(8)
O14	0.1704(5)	0.2256(5)	0.23780(9)	0.0279(8)
O16	0.3796(5)	0.1183(5)	0.15621(10)	0.0332(9)
O17	0.3146(5)	0.0240(5)	0.22589(10)	0.0299(8)
O18	0.4446(6)	-0.0772(6)	0.13785(11)	0.0411(10)
O19	-0.0331(6)	-0.1052(7)	0.10578(12)	0.0503(11)

4. Publications

site	x	y	z	U(eq)
O20	-0.2080(5)	0.1662(5)	0.10070(11)	0.0388(9)
O21	-0.3308(6)	-0.5430(6)	0.07810(11)	0.0428(10)
O22	0.0306(6)	0.4158(6)	0.14608(14)	0.0505(11)
O23	0.1427(7)	-0.2952(7)	0.09509(15)	0.0593(13)
O24	-0.7168(7)	-0.7969(7)	0.07969(17)	0.0654(15)
C1	0.8216(7)	0.4616(7)	0.3210(14)	0.0289(11)
C2	0.7679(7)	0.5225(7)	0.28566(15)	0.0296(11)
C3	0.83439(8)	0.71309(9)	0.28713(2)	0.0502(16)
C4	0.3556(7)	-0.0544(7)	0.35137(14)	0.0290(11)
C5	0.3850(7)	-0.0791(7)	0.30903(15)	0.0325(12)
C6	0.51161(9)	-0.14059(8)	0.30473(19)	0.0453(15)
C7	0.3101(7)	0.40239(7)	0.36254(14)	0.0301(12)
C8	0.18391(7)	0.3059(7)	0.32990(15)	0.0301(11)
C9	0.0141(9)	0.1633(9)	0.34542(17)	0.0426(14)
C10	-0.0621(7)	0.0331(7)	0.19725(15)	0.0296(11)
C11	-0.0119(7)	0.1338(7)	0.23494(14)	0.0297(11)
C12	-0.0837(8)	0.2535(9)	0.23868(19)	0.0420(14)
C13	0.4543(7)	0.4921(7)	0.15860(14)	0.0273(11)
C14	0.5807(7)	0.5175(7)	0.19083(15)	0.0299(11)
C15	0.7484(8)	0.5452(9)	0.17562(17)	0.0422(14)
C16	0.4036(7)	-0.0082(7)	0.16303(15)	0.0313(12)
C17	0.3790(7)	-0.0666(7)	0.20530(15)	0.0316(11)
C18	0.2588(9)	-0.2593(8)	0.20785(17)	0.0418(14)

Table S3. Anisotropic displacement parameters as derived from the single-crystal X-ray diffraction structure solution of $\text{Na}_3[\text{Al}(\text{L-lactate})_3]_2 \cdot 6 \text{H}_2\text{O}$.

	U11	U22	U33	U23	U13	U12
Al1	0.0295(8)	0.0286(8)	0.0231(7)	0.0001(6)	-0.0003(6)	0.0145(7)
Al2	0.0285(8)	0.0307(8)	0.0222(7)	-0.0013(6)	-0.0009(6)	0.0148(7)
Na1	0.0322(11)	0.0286(11)	0.0328(11)	0.0022(8)	0.0007(8)	0.0139(9)
Na2	0.0349(11)	0.0318(11)	0.0354(11)	-0.0019(9)	-0.0018(9)	0.0175(10)
Na3	0.0521(14)	0.0472(14)	0.0392(12)	0.0024(10)	-0.0019(10)	0.0290(12)
O1	0.036(2)	0.035(2)	0.027(2)	-0.0040(15)	-0.0029(15)	0.0159(18)
O2	0.035(2)	0.032(2)	0.0248(17)	-0.0062(14)	-0.0037(14)	0.0179(17)
O3	0.046(2)	0.041(2)	0.039(2)	-0.0075(17)	-0.0030(18)	0.029(2)
O4	0.027(2)	0.042(2)	0.0277(19)	0.0010(16)	-0.0001(14)	0.0139(18)
O5	0.033(2)	0.032(2)	0.0261(18)	0.0015(14)	0.0009(14)	0.0150(17)
O6	0.034(2)	0.049(2)	0.037(2)	-0.0108(18)	-0.0074(17)	0.017(2)
O7	0.034(2)	0.031(2)	0.0260(18)	0.0011(14)	0.0022(15)	0.0180(17)
O8	0.040(2)	0.039(2)	0.0195(17)	0.0020(15)	0.0042(15)	0.0229(18)
O9	0.040(2)	0.0281(19)	0.0248(19)	0.0028(15)	0.0010(15)	0.0117(17)
O10	0.032(2)	0.028(2)	0.033(2)	0.0035(15)	-0.0034(15)	0.0152(18)
O11	0.030(2)	0.033(2)	0.0263(19)	0.0020(15)	-0.0021(14)	0.0136(16)
O12	0.040(2)	0.028(2)	0.031(2)	0.0035(16)	-0.0010(16)	0.0149(17)
O13	0.031(2)	0.032(2)	0.0274(19)	-0.0016(15)	0.0006(15)	0.0128(17)
O14	0.0274(19)	0.0312(19)	0.0252(18)	-0.0033(14)	-0.0014(14)	0.0147(16)
O15	0.027(2)	0.041(2)	0.037(2)	-0.0075(16)	-0.0045(16)	0.0095(18)
O16	0.040(2)	0.036(2)	0.0281(19)	0.0012(15)	0.0045(15)	0.0223(18)
O17	0.036(2)	0.0274(19)	0.0268(18)	0.0008(14)	-0.0008(15)	0.0160(17)
O18	0.044(2)	0.049(2)	0.034(2)	-0.0082(18)	0.0020(17)	0.026(2)

4. Publications

	U11	U22	U33	U23	U13	U12
O19	0.043(3)	0.068(3)	0.035(2)	-0.008(2)	-0.0063(18)	0.024(2)
O20	0.041(2)	0.030(2)	0.034(2)	0.0023(16)	-0.0046(17)	0.0092(18)
O21	0.052(3)	0.049(3)	0.030(2)	-0.0018(17)	0.0008(18)	0.027(2)
O22	0.046(3)	0.051(3)	0.059(3)	-0.013(2)	-0.009(2)	0.028(2)
O23	0.068(3)	0.057(3)	0.060(3)	-0.020(2)	-0.012(2)	0.036(3)
O24	0.047(3)	0.057(3)	0.088(4)	0.025(3)	0.001(3)	0.023(3)
C1	0.032(3)	0.031(3)	0.027(3)	0.002(2)	0.003(2)	0.018(2)
C2	0.029(3)	0.032(3)	0.035(3)	-0.001(2)	0.001(2)	0.021(2)
C3	0.029(3)	0.046(4)	0.076(5)	-0.021(3)	-0.006(3)	0.019(3)
C4	0.031(3)	0.031(3)	0.028(3)	-0.004(2)	-0.002(2)	0.018(3)
C5	0.029(3)	0.037(3)	0.030(3)	-0.004(2)	0.000(2)	0.015(2)
C6	0.052(4)	0.029(3)	0.042(3)	0.004(2)	-0.007(3)	0.010(3)
C7	0.028(3)	0.034(3)	0.024(3)	-0.006(2)	-0.006(2)	0.012(2)
C8	0.036(3)	0.029(3)	0.025(3)	-0.001(2)	0.000(2)	0.017(2)
C9	0.052(4)	0.054(4)	0.032(3)	0.009(3)	0.004(3)	0.034(3)
C10	0.032(3)	0.026(3)	0.031(3)	0.004(2)	0.001(2)	0.014(2)
C11	0.029(3)	0.032(3)	0.025(3)	0.002(2)	-0.0001(19)	0.013(2)
C12	0.033(3)	0.048(4)	0.048(4)	-0.009(3)	-0.003(2)	0.024(3)
C13	0.031(3)	0.027(3)	0.027(3)	-0.003(2)	-0.002(2)	0.016(2)
C14	0.032(3)	0.026(3)	0.030(3)	-0.001(2)	-0.001(2)	0.013(2)
C15	0.037(3)	0.057(4)	0.033(3)	0.012(3)	0.001(2)	0.024(3)
C16	0.025(3)	0.036(3)	0.030(3)	-0.006(2)	-0.002(2)	0.012(2)
C17	0.031(3)	0.033(3)	0.031(3)	-0.005(2)	-0.002(2)	0.016(2)
C18	0.056(4)	0.031(3)	0.038(3)	0.001(2)	0.007(3)	0.021(3)

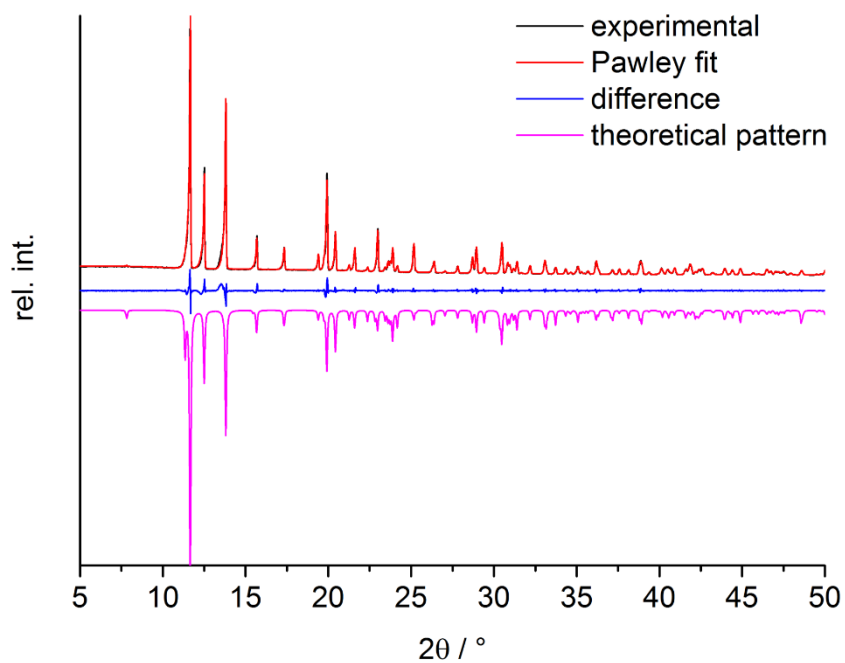


Figure S1. Powder X-Ray diffraction pattern of $\text{Na}_3[\text{Al}(\text{L-lactate})_3]_2 \cdot 6 \text{H}_2\text{O}$ with Pawley profile plot and difference plot. $R_p = 3.99$, $R_{wp} = 5.83$. cell axes after refinement were $a = 8.9895(1)$ & $c = 33.8959(3)$. The magenta line represents the simulated powder pattern according to the single-crystal X-ray diffraction structure solution (Tables S1 – S3). The lattice parameters have been adapted to the ones derived from the Pawley refinement.

Table S4. ^{13}C isotropic NMR shifts of $\text{Na}_3[\text{Al}(\text{L-lactate})_3]_2 \cdot 6 \text{H}_2\text{O}$ obtained from the observed ^{13}C MAS NMR spectrum depicted in Figure 1 and the comparison to results of DFT shift calculations. #1 and #2 refer to the two individual $\text{Al}(\text{L-lactate})_3$ units within the biscluster.

	$\delta_{\text{iso}} / \text{ppm} (\text{COO}^-)$	$\delta_{\text{iso}} / \text{ppm} (\text{CHOH})$	$\delta_{\text{iso}} / \text{ppm} (\text{CH}_3)$
exp	184.5	67.9	22.7
	183.8		22.3
	182.7		21.4
	181.1		
	180.4		
DFT	189.5 ($\text{Al}(\text{L-Lactate})_3$ #1)	68.1 ($\text{Al}(\text{L-Lactate})_3$ #1)	17.4 ($\text{Al}(\text{L-Lactate})_3$ #1)
	186.1 ($\text{Al}(\text{L-Lactate})_3$ #1)	67.9 ($\text{Al}(\text{L-Lactate})_3$ #1)	16.9 ($\text{Al}(\text{L-Lactate})_3$ #1)
	185.4 ($\text{Al}(\text{L-Lactate})_3$ #1)	68.8 ($\text{Al}(\text{L-Lactate})_3$ #1)	17.9 ($\text{Al}(\text{L-Lactate})_3$ #1)
	184.4 ($\text{Al}(\text{L-Lactate})_3$ #2)	68.8 ($\text{Al}(\text{L-Lactate})_3$ #2)	15.3 ($\text{Al}(\text{L-Lactate})_3$ #2)
	183.8 ($\text{Al}(\text{L-Lactate})_3$ #2)	68.6 ($\text{Al}(\text{L-Lactate})_3$ #2)	18.4 ($\text{Al}(\text{L-Lactate})_3$ #2)
	183.5 ($\text{Al}(\text{L-Lactate})_3$ #2)	67.8 ($\text{Al}(\text{L-Lactate})_3$ #2)	17.0 ($\text{Al}(\text{L-Lactate})_3$ #2)

Table S5. Comparison of the observed and calculated ^{27}Al NMR parameters (isotropic shift, C_Q and η_Q) for $\text{Na}_3[\text{Al}(\text{L-lactate})_3]_2 \cdot 6 \text{H}_2\text{O}$.

	Al1 (exp.)	Al1 (DFT)	Al2 (exp.)	Al2DFT
$\delta_{\text{iso}} / \text{ppm}$	25.6	25.0	24.3	24.9
C_Q / MHz	2.76	2.35	2.21	2.30
η_Q	0.64	0.84	0.63	0.58

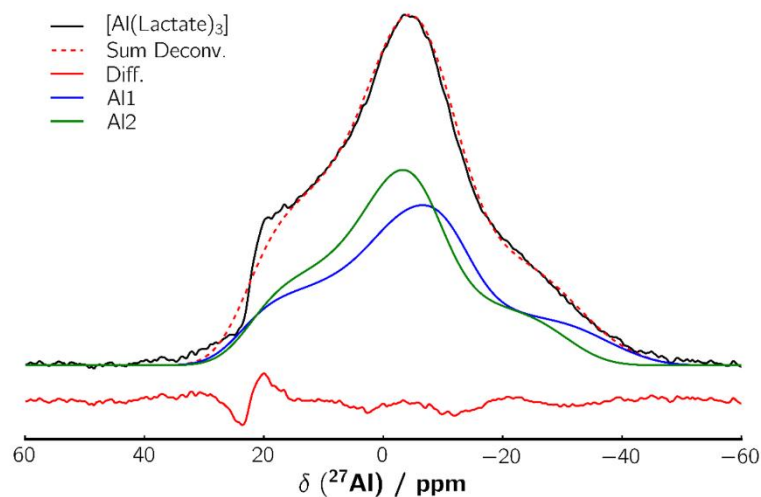


Figure S2. ^{27}Al MAS NMR spectrum of $\text{Al}(\text{L-lactate})_3$.

Table S6. Observed and DFT calculated isotropic chemical shifts and quadrupolar coupling parameters of ^{27}Al in solid $\text{Al}(\text{L-lactate})_3$. The deviation between the observed and the calculated values is most likely caused by thermal motion, which is not included in the calculation.

	Al1 (exp.)	Al1 (DFT)	Al2 (exp.)	Al2DFT
$\delta_{\text{iso}} / \text{ppm}$	24.6	22.9	22.9	24.6
C_Q / MHz	5.0	5.2	4.6	4.8
η_Q	0.75	0.50	0.8	0.51

Table S7. Relevant refinement parameters of the deconvolution of the ^1H MAS NMR spectrum of $\text{Na}_3[\text{Al}(\text{L-lactate})_3]_2 \cdot 6 \text{H}_2\text{O}$. Labelling of signals according Figure 3.

	0 (CHOH)	1 (H ₂ O)	2 (CHOH)	3 (CH ₃)
$\delta_{\text{iso}} / \text{ppm}$	16.6	4.4	4.0	1.3
FWHM	1.00	0.23	0.75	0.709
G/L ratio	0.15	0.43	1.	0.40
Int.	3.3	5.6	11.4	18.8

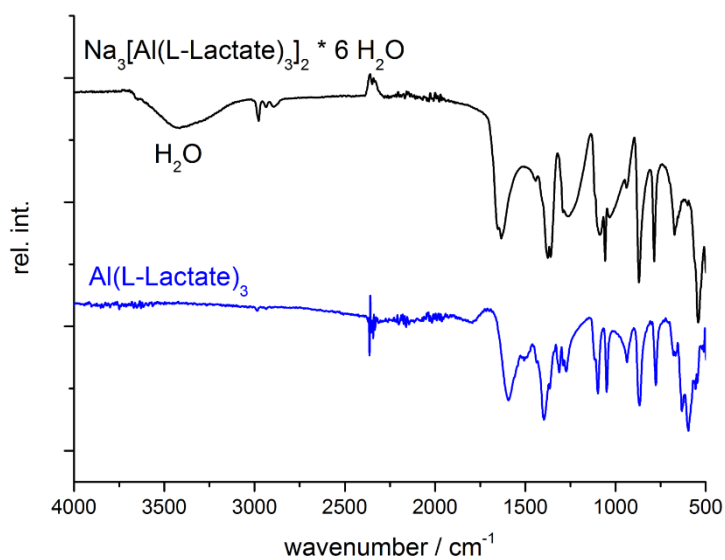


Figure S3. IR spectra of $\text{Na}_3[\text{Al}(\text{L-lactate})_3]_2 \cdot 6 \text{H}_2\text{O}$ and $\text{Al}(\text{L-lactate})_3$. The bands at 2450 cm^{-1} are artifacts from the measurement.

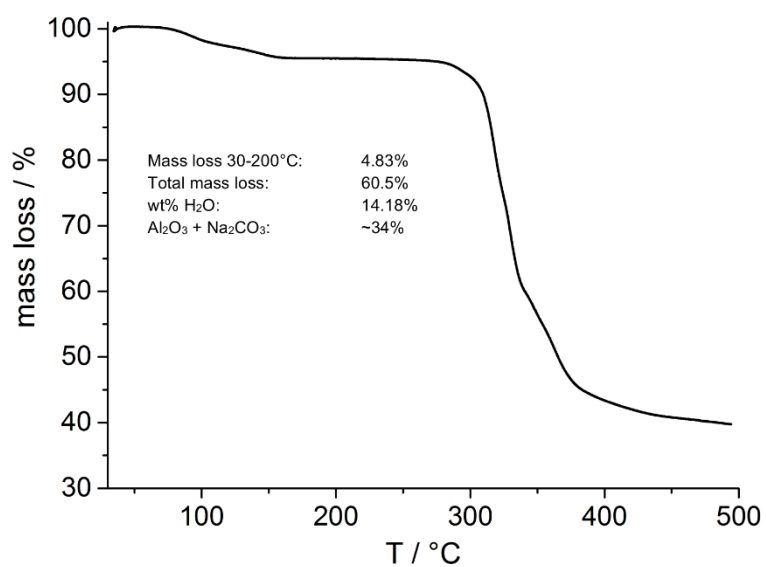


Figure S4. Thermogravimetric analysis of $\text{Na}_3[\text{Al}(\text{L-lactate})_3]_2 \cdot 6 \text{H}_2\text{O}$. The mass loss up to 200°C corresponds to two water molecules. Calculated wt% of Al_2O_3 and Na_2CO_3 is 27.27% of the initial mass. The total amount of lactate and water calculated from the sum formula amounts to 83.9%.

Table S8. Observed and calculated cell constants including the deviation between both values.

	XRD	DFT	Deviation / %
a / Å	9.02	8.86	-1.78
c / Å	35.31	34.48	-2.39
V / Å ³	2489.4	2346.9	-6.07

Table S9. Selected bond lengths as determined by XRD and after geometry optimization with DFT for Na₃[Al(L-lactate)₃]₂ * 6 H₂O. Deviations are given in absolute and relative values.

Atom #1	Atom #2	Bond length XRD / Å	Bond length DFT / Å	Deviation / Å	Deviation / %
Na1	O12	2,319	2,365	0,004	0,187
Na1	O20	2,347	2,387	-0,003	-0,134
Na1	O18	2,384	2,474	0,045	1,893
Na1	O15	2,451	2,529	0,023	0,933
Na1	O9	2,527	2,525	-0,056	-2,202
Na1	O19	2,598	2,569	-0,075	-2,889
Na2	O6	2,334	2,414	0,036	1,548
Na2	O9	2,395	2,428	-0,009	-0,379
Na2	O3	2,45	2,479	-0,026	-1,052
Na2	O24	2,461	2,52	0,014	0,575
Na2	O21	2,51	2,517	-0,038	-1,496
Na2	O12	2,528	2,524	-0,059	-2,335
Na3	O20	2,39	2,455	0,022	0,901
Na3	O21	2,47	2,527	0,012	0,473
Na3	O24	2,481	2,566	0,04	1,612
Na3	O18	2,519	2,587	0,017	0,681
Na3	O7	2,519	2,562	-0,012	-0,458
Na3	O16	2,733	2,662	-0,128	-4,673
Al1	O11	1,899	1,884	-0,014	-0,75
Al1	O14	1,899	1,877	-0,022	-1,18
Al1	O17	1,903	1,89	-0,013	-0,688
Al1	O13	1,907	1,905	-0,002	-0,099

4. Publications

Atom #1	Atom #2	Bond length XRD / Å	Bond length DFT / Å	Deviation / Å	Deviation / %
Al1	O10	1,932	1,92	-0,012	-0,611
Al1	O16	1,935	1,914	-0,021	-1,071
Al2	O8	1,876	1,885	0,009	0,488
Al2	O2	1,884	1,874	-0,009	-0,502
Al2	O1	1,897	1,906	0,009	0,492
Al2	O5	1,915	1,897	-0,018	-0,938
Al2	O4	1,927	1,92	-0,007	-0,355
Al2	O7	1,94	1,913	-0,027	-1,411
C1	O1	1,315	1,305	0,01	0,756
C1	O3	1,221	1,238	-0,017	-1,41
C2	O2	1,412	1,425	-0,013	-0,921
C4	O4	1,284	1,291	-0,007	-0,521
C4	O6	1,239	1,246	-0,007	-0,59
C5	O5	1,432	1,429	0,003	0,229
C7	O7	1,297	1,298	-0,001	-0,08
C7	O9	1,24	1,241	-0,002	-0,156
C8	O8	1,426	1,429	-0,003	-0,196
C10	O13	1,291	1,307	-0,015	-1,194
C10	O15	1,236	1,239	-0,003	-0,254
C11	O14	1,426	1,43	-0,003	-0,222
C13	O10	1,288	1,306	-0,018	-1,424
C13	O12	1,239	1,236	0,004	0,285
C14	O11	1,426	1,427	0	-0,015
C16	O16	1,288	1,288	0	-0,024
C16	O18	1,239	1,251	-0,012	-0,984

4. Publications

Atom #1	Atom #2	Bond length XRD / Å	Bond length DFT / Å	Deviation / Å	Deviation / %
C17	O17	1,419	1,43	-0,01	-0,74
C1	C2	1,534	1,527	0,007	0,442
C2	C3	1,512	1,52	-0,008	-0,538
C4	C5	1,553	1,524	0,029	1,849
C5	C6	1,506	1,524	-0,018	-1,207
C7	C8	1,549	1,531	0,018	1,157
C8	C9	1,525	1,522	0,002	0,154
C10	C11	1,549	1,531	0,019	1,199
C11	C12	1,517	1,522	-0,005	-0,309
C13	C14	1,546	1,526	0,02	1,266
C14	C15	1,506	1,521	-0,015	-0,989
C16	C17	1,564	1,521	0,044	2,799
C17	C18	1,525	1,521	0,004	0,231

Table S10. ^{23}Na ssNMR refinement parameters of the deconvolution and DFT calculated NMR parameter for the isotropic chemical shift and the quadrupolar interaction for $\text{Na}_3[\text{Al}(\text{L-lactate})_3]_2 \cdot 6 \text{H}_2\text{O}$.

	Na1 exp	Na1 DFT	Na2 exp.	Na2 DFT	Na3 exp.	Na3 DFT
$\tilde{\delta}_{\text{iso}}$ / ppm	1.35	1.83	-2.91	-1.41	3.42	1.4
$\tilde{\delta}_{\text{aniso}}$ / ppm	10.22	10.2	5.47	5.47	8.74	-8.74
η	0.65	0.65	0.33	0.33	0.81	0.81
C_Q / MHz	2.21	-2.54	1.15	1.37	2.01	2.07
η_Q	0.25	0.26	0.60	0.60	0.76	0.77

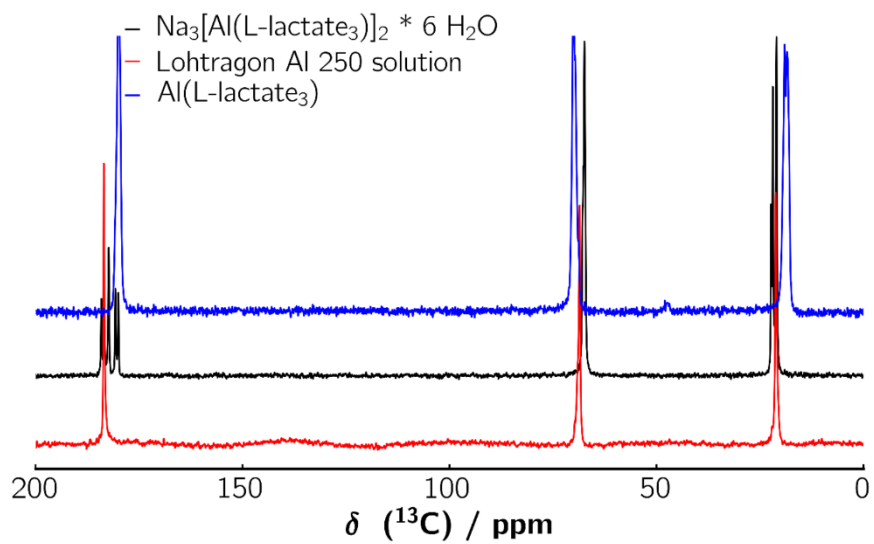


Figure S5. ^{13}C liquid-state NMR spectra of aqueous solutions of $\text{Na}_3[(\text{Al}(\text{L-lactate})_3)_2] \cdot 6 \text{H}_2\text{O}$ and ^{13}C CP MAS NMR of solid $\text{Na}_3[(\text{Al}(\text{L-lactate})_3)_2] \cdot 6 \text{H}_2\text{O}$ and solid $\text{Al}(\text{L-lactate})_3$.

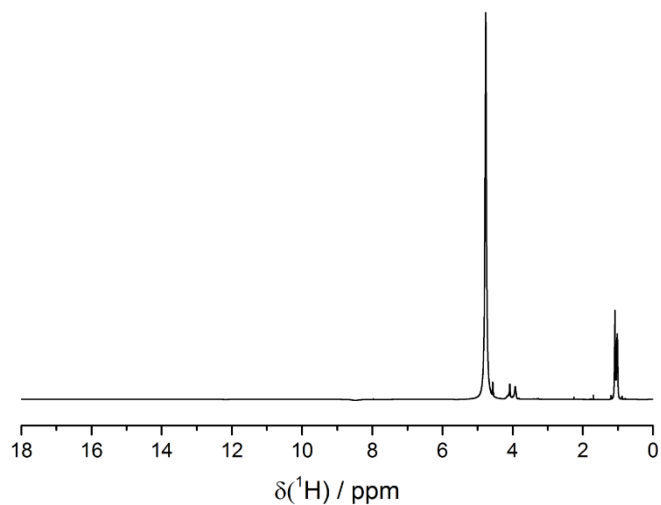


Figure S6. ^1H liquid-state NMR of the Lohtragon-type solution.

Spin-Spin relaxation for quadrupolar nuclei in liquids

Since the quadrupolar interaction is usually large it is often the dominating factor of the spin-lattice relaxation of quadrupolar nuclei in liquid state NMR. For fast isotropic motion T_2 is given by:¹

$$T_2 = \frac{3}{40} \frac{(2I + 3)}{[I^2(2I - 1)]} [1 + \eta_Q^2/3] C_Q^2 \tau_c \quad (S\ 1)$$

with T_2 being the spin-spin relaxation time under the influence of a quadrupolar interaction. I equals $5/2$ for aluminium, η_Q is the quadrupolar asymmetry, C_Q the quadrupolar coupling and τ_c the rotational correlation time given by:

$$\tau_c = (4\pi\eta r^3)/(3kT) \quad (S\ 2)$$

where η is the viscosity of the solution, r the radius of the molecule (under the assumption it is spherical), k the Boltzmann-constant and T the temperature.

Table S11. Estimated C_Q values derived from equations S1 and S2 and the observed linewidths for the resonances within the ^{27}Al liquid-state NMR spectra depicted in Figure 7. The temperature was set to 293 K, η_Q to 0.65 and an viscosity of 100 mPas was used. The viscosity has been adjusted to fit the Coupling observed in the solids and is overestimated by a factor of ~ 2 -3 indicating that C_Q is not the only influencing factor on the relaxation. The coupling doubles between pH 5.5 and 3.5.

pH	FWHM / Hz	estimated C_Q / MHz
5.5	808.2	2.7
5.0	839.9	2.7
4.5	1077	3.1
4.0	1646	3.8
3.5	2552	4.8

Table S12. Calculated ^{27}Al NMR parameters of isolated $\text{Al}(\text{L-Lactate})_3$, $\text{Al}(\text{L-Lactate})_3^-$, $\text{Al}(\text{L-Lactate})_3^{2-}$, and the binuclear $[\text{Al}(\text{L-Lactate})_3]_2^{3-}$ complex.

	$\text{Al}(\text{L-Lactate})_3$	$\text{Al}(\text{L-Lactate})_3^{1-}$	$\text{Al}(\text{L-Lactate})_3^{2-}$	$[\text{Al}(\text{L-Lactate})_3]_2^{3-}$
δ_{iso} / ppm	31.6	41.1	48.5	24.4 / 25.0
C_Q / MHz	11.3	-10.7	-9.6	3.8 / 3.8
η_Q	0.02	0.81	0.7	0.41 / 0.44

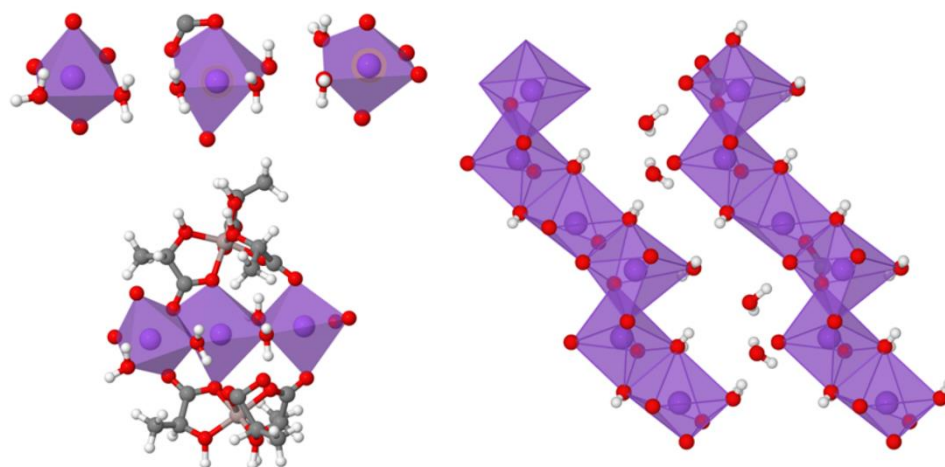


Figure S7. First coordination sphere of the three sodium atoms of $\text{Na}_3[\text{Al}(\text{L-lactate})_3] \cdot 6 \text{H}_2\text{O}$ and the edge sharing connection between them. (top Left to top middle Na1 – Na3, bottom left: Edge sharing sodium channels in the interlayer space with the terminal water that causes the highest C_Q). Right side: sodium octahedra strands with non coordinating water between the strands.

Bibliography

- (1) Steigel, A.; Spiess, H. W. *Dynamic NMR Spectroscopy*; Springer Science & Business Media, 2012; Vol. 15.

5. Addendum

5.1 Density Functional Theory (DFT)

This section is just a short overview of the basic concepts of DFT with focus on the techniques employed in the scope of this thesis, for an in-depth review consider the literature.^[30,125,126]

DFT, as an *ab-initio* method, is based on the Schrödinger-equation

$$\hat{H}\Psi = E\Psi \quad (1.2.1)$$

Where Ψ is the wave function, E the systems total energy, and \hat{H} the Hamiltonian. This equation correlates an atomic or molecular system with its total energy via the wave function, where \hat{H} contains the interaction between the particles.

As the Schrödinger equation is not analytically solvable for Systems bigger than the hydrogen atom, as a first, step the Born-Oppenheimer approximation is applied. It states that the nuclei mass exceeds the one of the electrons by far, having the latter follow every movement instantaneously. In a first approximation this lets us divide the degrees of freedom of the nuclei from the degrees of freedom of the electrons:

$$\hat{H}_{tot} = T_n + T_e + V_{ne} + V_{ee} + V_{nn} \quad (1.2.2)$$

with \hat{H}_{tot} denoting all interactions, being split up into kinetic energy T of the nuclei n and the electrons e and the potential energy V between all interacting particles.^[127] We can therefore treat the electrons as if they were interacting with each other within an external potential V_{ext} of the (fixed) nuclei. The Hamiltonian can then be written as follows:

$$\hat{H} = -\frac{\hbar^2}{2m_e} \sum_i \nabla_i^2 + \sum_i V_{ext}(r_i) + \frac{1}{2} \sum_{i \neq j} \frac{e^2}{|r_i - r_j|} \quad (1.2.3)$$

where m_e is the electrons mass, \hbar Plancks constant, ∇ the nabla operator, meaning the derivative into every direction of space, r the distance between nucleus and electron and e the elementary electric charge.

DFT is based on the two Hohenberg-Kohn theorems, which aim to formulate it as an exact theory of many body systems:

H-K theorem 1: *For any given system of interacting particles in an external potential, this potential is, except for a constant, uniquely determined by the ground state particle density.*

This also means that the Hamiltonian is, except for a constant shift in energy, fully determined and therefore the many body wavefunctions are determined as well. Hence, all properties of the system are completely determined given the ground state density.

H-K theorem 2: *A universal Energy functional of the electron density ρ can be defined which is valid for any external potential. For any potential the exact ground state energy is the global minimum of this functional and the corresponding density at this minimum is the exact ground state density.*

This means that only an exact functional is needed to find both ground state energy and electron density of a system. One of the main problems of modern DFT is that the exact functional is unknown, therefore the challenge is to get as close approximation as possible. It also implies that excited states can't be determined.

These theorems show that the wave function of the electrons is solely depending on the total electron density ρ :

$$\rho(r_1) = \int \Psi_{(r_1 r_2 \dots r_n)} \Psi_{(r_1 r_2 \dots r_n)} dr_2 \dots dr_n. \quad (1.2.4)$$

This reduces the computational effort from $3N$ variables to 3 resulting in an immense speed advantage. The problem at this point is, that we still have to deal with a many body system of interacting particles.^[128]

The Kohn-Sham *ansatz*

The Kohn-Sham *ansatz*, which resolves the necessity to deal with interacting many body systems is based upon two assumptions:

- (1) The exact ground state density of any many body system with interacting particles can be represented by an artificially chosen system of non-interacting particles.

It is important to note, that this is an *ansatz* which has not been proven. Even though there is no rigorous proof, given the broad adoption of the method and the outstanding amount of research being done using this theory, we assume its validity.

- (2) The Hamiltonian is constructed in a way that it contains the usual kinetic operator and an effective potential acting on an electron of spin sigma at point r. Ignoring spin-orbit interactions, we assume that the external potential is spin-independent but the effective potential still has to be spin-dependent in order to give the right density for each spin.

After consideration of the orthonormality, similar to the Raleygh-Ritz principle this leads to the Kohn-Sham Schrödinger-like equations:

$$(H_{KS}^{\sigma} - \varepsilon_i^{\sigma})\Psi_i^{\sigma}(r) = 0 \quad (1.2.5)$$

with ε_i^{σ} being the eigenvalues and H_{KS}^{σ} being the effective Hamiltonian.

$$H_{KS}^{\sigma}(r) = -\frac{1}{2}\nabla^2 + V_{KS}^{\sigma}(r) \quad (1.2.6)$$

$$V_{KS}^{\sigma}(r) = V_{ext}(r) + \frac{\delta E_{Hartree}}{\delta n(r, \sigma)} + \frac{\delta E_{XC}}{\delta n(r, \sigma)} = V_{ext}(r) + V_{Hartree}(r) + V_{XC}^{\sigma}(r) \quad (1.2.7)$$

These are independent particle equations employing a potential that must be self-consistent with the resulting density. Under the presumption that the exchange and correlation functional E_{XC} , is known these yield the exact ground-state energy and density independently of any approximations to E_{XC} . As the Hohenberg and Kohn theorems state the ground state density uniquely determines the potential at the minimum. This also means that for any given system of interacting electrons there is a unique Kohn-Sham potential. This approach separates the independent-particle kinetic energy and the long-range Hartree terms from the exchange-correlation functional which can then be approximated as (nearly) local functional of the density. Therefore, the energy can be expressed as:

$$E_{XC}[n] = \int dr n(r) \epsilon_{XC}([n], r) \quad (1.2.8)$$

where ϵ_{XC} is the energy per electron at the position r that's dependant solely upon the density $n(r, \sigma)$ in the near vicinity of r. For spin polarized systems the spin is incorporated in ϵ_{XC} .

This approximates the exchange correlation energy E_{XC} with the one of a uniform electron gas with the same charge density η in dependency of the point in space \vec{r} . The exchange interaction is in principle nothing but considering the Pauli exclusion principle by repulsion of same spin electrons and therefore alters the distance between them. The correlation interaction is a measure of how much the movement of an electron influences all other surrounding electrons.^[129,130]

The most general way to define a functional is to make use of the local density approximation (LDA) which assumes that the exchange-correlation energy is an integral over the whole space with the exchange correlation density to be the same as the homogenous electron gas density at each point:

$$E_{XC}^{LDA}[n] = \int d^3r n(r) [\epsilon_X^{hom}(n(r)) + \epsilon_C^{hom}(n(r))] \quad (1.2.9)$$

Due to E_{XC} being universal it is the exact same as in the homogenous electron gas. The exchange-correlation energy as function of the electron density is needed though. While the exchange energy can be calculated analytically the correlation energy is being approximated based on Monte-Carlo methods.^[131]

Even though the LDA functional is widely used to predict properties of materials,^[112,132–138] it is known to overestimate bond lengths due to an underestimation of bond strength.^[139]

Kohn and Sham already suggested in their original work a so called “gradient expansion approximation” in which a functional of the magnitude of gradient of the density $|\nabla n^\sigma|$ and the value n are approximated.^[130] Even though this approach was investigated further, it didn’t lead to consistent results due to violation of the sum rule.^[140] This then led to the generalized-gradient approximation in which the functional is defined in a generalized form of (1.2.9):

$$E_{XC}^{GGA}[n] = \int d^3r n(r) \epsilon_X^{hom}(n) F_{XC}(n, \nabla n, \dots) \quad (1.2.10)$$

where F_{XC} is dimensionless and which lowest order terms have been solved analytically:^[141,142]

$$F_X = 1 + \frac{10}{81} s_1^2 + \frac{146}{2025} s_2^2 + \dots \quad (1.2.11)$$

ϵ_x is the exchange energy of the unpolarized electron gas. Due to a spin scaling factor for the exchange only the spin-unpolarized $F_{XC}(n, |\nabla n|,)$ has to be considered. This leads to explicit first dimensionless reduced density gradients of the form:

$$s_1 = s = \frac{|\nabla r_s|}{2(2\pi/3)^{1/3}r_s} \quad (1.2.12)$$

In the case of the Perdew Burke Ernzerhof (PBE) functional, which has been extensively used in this work, equation (1.2.1:6) takes the form of:

$$E_{XC}^{GGA}[n] = \int d^3r n(r) \epsilon_X^{hom}(n) F_{XC}(r_s, \xi, s) \quad (1.2.13)$$

Where r_s is the local Seitz radius ($n = 3/4\pi r_s^3$) and ξ the relative spin polarization ($= \frac{(n_\uparrow - n_\downarrow)}{n}$).^[143]

Periodic boundary conditions and Pseudopotentials

In crystalline systems the external potential for the electrons is periodical. This also means that the electron density fulfils periodicity ($n(r) = n(r + R)$ with R being the lattice vectors. Bloch's theorem shows that the single particle wave functions are quasi periodical :

$$\Psi_k^n(r + R) = e^{ik \cdot R} \Psi_k^n(r) \quad (1.2.14)$$

The physical properties are calculated as the average over all values of the wavenumber k which only unique ones lie within the first Brillouin zone (BZ).^[144] For insulators the electron density varies only smoothly within the BZ giving rise to the ability to integrate over a grid of special points.^[145] While metals are not within the scope of this thesis it should still be noted that they need higher precision sampling of the BZ.^[146]

For practical reasons^[42] we express the wave functions using a set of plane waves:

$$\Psi_k^n(r) = \sum_G c_k^n(G) e^{i(k+G) \cdot r} \quad (1.2.15)$$

When choosing G to be a set of reciprocal lattice vectors the planewave functions necessarily fulfil periodic boundary conditions. The number of functions is defined using a cutoff radius or energy E_{cut} :

$$\frac{1}{2}|k + G|^2 \leq E_{cut} \quad (1.2.16)$$

This limits the basis set by kinetic energy which, on the other hand means that we would need big basis sets to represent the core electrons. While these contribute the most to the total energy of a system, they have almost no effect on their chemistry. Therefore it is a valid approximation to treat these electrons as an effective charge reduction of the nucleus and just treat the valence electrons quantum mechanically. This reduces the computational effort drastically. A second approximation has to be made due to the fact that the valence electrons wave functions oscillate strongly. This leads to the frozen core approximation which replaces the nuclear Coulomb interaction between core and valence electrons by a smooth effective potential. This is called Pseudopotential (PP) and two schemes have been proposed for their construction, namely norm conserving^[147] and “*ultrasoft*”^[148] PPs. The latter is the state-of-the-art scheme, which has been employed in the work for this thesis. In this scheme, extremely smooth wave functions are obtained by relaxing norm conservation in a way that the wave functions should yield the charge density. This is then compensated by including atom-centred effective charges to maintain total charge within the system.

The gauge including projector augmented wave method

While PPs significantly reduce the computational effort needed to calculate a system, their application is only valid to calculate systems that depend on characteristics caused outside of the core region. This does not include NMR properties which are heavily dependent on all electrons surrounding the core. In order to calculate such properties within the PP-formalism it is necessary to map the valence pseudo wave functions on the corresponding all-electron wave functions as shown by Van de Walle and Blöchl using Projector Augmented Waves (PAW)^[149]:

$$T = 1 + \sum_{R,n} [|\phi_{R,n}\rangle - |\tilde{\phi}_{R,n}\rangle] \langle \tilde{P}_{R,n} | \quad (1.2.17)$$

where $\langle \tilde{P}_{R,n} |$ denotes a set of projectors that map the pseudo wave functions $|\phi_{R,n}\rangle$ on the all-electron ones $|\tilde{\phi}_{R,n}\rangle$, with R being an atomic site and n referring to angular momentum quantum numbers. Both all-electron and pseudo wave functions are derived from calculations of isolated atoms.

While the ground state charge density is sufficient to calculate the electric field gradient, just like in the real-world application, the basis for the NMR shielding is the electronic current induced by an external magnetic field. As the changes in current are small, they can be treated by perturbation theory within the DFT formalism. This means expanding the wavefunctions into:

$$\Psi(r) = \Psi^0(r) + \Psi^{(1)}(r) + O(B^2) \quad (1.2.18)$$

Where $\Psi^0(r)$ is the unpertubated ground-state wave function, O the all-electron operator in dependence of the magnetic field B and $\Psi^{(1)}(r)$ the first order change which is can be described as an addition of unoccupied states e via:

$$\Psi^{(1)}(r) = \sum_e a_e \Psi_e^{(0)}(r) \quad (1.2.19)$$

To calculate the current the corresponding operator $J(r')$ is needed which is the sum of diamagnetic and paramagnetic terms:

$$J(r') = J^d(r') + J^p(r') \quad (1.2.20)$$

In conjunction with the symmetric gauge for the vector potential the induced orbital current $j^{(1)}(r)$ is given by:

$$j^{(1)}(r) = 4 \frac{1}{2c} \sum_o Re \left[\langle \Psi_o^{(0)} | J^p(r') \mathcal{G}(\varepsilon_o^{(0)})(r - r') \times p | \Psi_o^{(0)} \rangle \right] \quad (1.2.21)$$

Which resembles the paramagnetic and diamagnetic current and the fact that only the sum of both is well defined and they can't be treated separately.^[150–152] In this case $\eta(r')$ is spin polarized, to account for spin degeneracy. \mathcal{G} is a Green's function to fulfil boundary conditions.

Even though the planewave approach in principle does not suffer from the “gauge origin problem” this is introduced when using projector augmented waves. This is caused by the fact that the paramagnetic and diamagnet terms converge differently depending on the

distance to the gauge origin and would, for finite basis sets, lead to different electric currents surrounding two chemical identical nuclei due to their different distance to the gauge origin. To address this gauge dependence a field-dependent transformation parameter T_B was introduced by Mauri and Pickard which leads to the Gauge Including Projector Augmented wave (GIPAW) method:^[150]

$$T_B = 1 + \sum_{R,n} e^{i/2cr \cdot R \times B} \left[|\phi_{R,n}\rangle - \tilde{\phi}_{R,n}\rangle \right] \langle \tilde{p}_{R,n} | e^{-(i/2c)r \cdot R \times B} \quad (1.2.22)$$

With this approach it is possible to calculate the complete magnetic shielding σ_{iso} of the surrounding electrons of a nucleus. This shielding correlates with the isotropic chemical shielding δ_{iso} through:

$$\delta_{iso} = -\sigma_{iso} + \sigma_{ref} \quad (1.2.23)$$

Where σ_{ref} is a nucleus dependant referencing constant.^[78]

Semi-empirical dispersion correction

When DFT started to be used to calculate real world systems, it became obvious early on that long-range dispersion interactions are not described correctly in common density functionals.^[153–158] Functionals like the popular BLYP, B3LYP and PBE do not account for attractive long-range interactions.^[159–163] Dispersion is a part of electron correlation that operates only on large scales, While standard functionals deal very well with short electron-electron distances because these are deeply related to electron density changes. This on the other hand means that DFT faces the challenge to merge both long and short-range asymptotical behaviours.

To date there are four methods for implementation of dispersion correction in DFT: nonlocal vdW-DF,^[164,165] parameterized versions of standard hybrid approximations,^[166] dispersion correcting atom-centred one-electron potentials^[167–169] and DFT-D methods.^[170–173] While there are reasons to use the former three (like correction of the actual wavefunction or electron density), DFT-D has the inevitable advantage of low numerical complexity and therefore is the most common one.

The Grimme scheme

DFT-D treats the dispersion interactions semiclassical by introducing a corrective dispersion energy E_{disp}^{DFT-D} that acts on every pair of atoms (AB) in the system depending on their distance R_{AB}^n :

$$E_{disp}^{DFT-D} = - \sum_{AB} \sum_{n=6,8,10,..} s_n \frac{C_n^{AB}}{R_{AB}^n} f_{damp}(R_{AB}) \quad (1.2.23)$$

C_n^{AB} denotes the averaged (isotropic) nth-order ($n = 6, 8, 10, \dots$) dispersion coefficient. The global scaling factor s_n is mainly dependent on the applied Density functional.^[171] A dampening function $f_{damp}(R_{AB})$ is necessary to avoid singularities for small distances and to avoid overestimating contributions at intermediate R. Usually this dampening has the form:

$$f_{damp}(R_{AB}) = \frac{1}{1 + 6(R_{AB}/(s_{r,n}R_0^{AB}))^{-y}} \quad (1.2.24)$$

or:

$$f_{damp}(R_{AB}) = \frac{1}{1 + e^{-y(R_{AB}/s_{r,n} R_0^{AB} - 1)}} \quad (1.2.25)$$

Where R_0^{AB} is an (empirical vdW) cutoff radius for each atom pair (AB) and y a constant that determines the steepness of the function for small distances.^[174,175]

DFT-D exists in different iterations, dubbed DFT-D1-D3 boasting accuracy and applicability with each version combined with less empirism. The latest version contains *ab initio* atom pairwise-specific dispersion coefficients and refined cutoff radii for all elements with $Z \leq 94$.^[173] In addition DFT-D3 introduced fractional coordination numbers (CNs) which are calculated by:

$$CN^A = \sum_{B \neq A}^{N_{atoms}} \frac{1}{1 + e^{-16(4(R_{A,cov} + R_{B,cov})/(3R_{AB}) - 1)}} \quad (1.2.26)$$

Where $R_{A,cov} + R_{B,cov}$ are molecular single-bond covalent radii.^[176] This takes into account the chemical fact, that atoms in different bonding or hybridization environments have different coordination numbers.^[177]

The Tkatchenko-Scheffler scheme

In contrast, the Tkatchenko-Scheffler (TS) approach is a pairwise dispersion correction scheme dependent on density.^[178] By using the density it takes into account the molecular environment. The energy is given similarly to (1.2.23):

$$E_{disp}^{TS} = - \sum_{AB} \frac{C_6^{AB}}{R^6} f_{damp}^{Fermi}(R) \quad (1.2.27)$$

Within the TS approach the so-called average-energy or Unsöld approximation is employed which results in excitation energies being replaced by averages.^[179–181] The dispersion coefficient C_6^{AB} is approximated from the homoatomic ones with static polarizabilities α_A^0 via:^[182]

$$C_6^{AB} = \frac{C_6^{AA} C_6^{BB}}{(\alpha_B^0 / \alpha_A^0) C_6^{AA} + (\alpha_A^0 / \alpha_B^0) C_6^{BB}} \quad (1.2.28)$$

Where the homoatomic coefficients are calculated using the ratio of the effective atom volume in a molecule and the free atom volume v_A ^[183] and dispersion coefficients $C_{6,free}^{AA}$ as calculated by Chu *et. al.*:^[184]

$$C_6^{AA} = v_A^2 C_{6,free}^{AA} \quad (1.2.29)$$

$$\alpha_A^0 = v_A \alpha_{A,free}^0 \quad (1.2.30)$$

where v_A is obtained by Hirshfeld partitioning.^[185]

This basically means that the TS method approximates effects of the environment on the polarizability by a change of atomic volume.

Erklärung

Hiermit versichere ich eidesstattlich, dass ich die Arbeit selbstständig verfasst und keine anderen als die von mir angegebenen Quellen und Hilfsmittel benutzt habe.

Hiermit erkläre ich, dass ich die Dissertation nicht bereits zur Erlangung eines akademischen Grades eingereicht habe und dass ich nicht bereits diese oder eine gleichartige Doktorprüfung endgültig nicht bestanden habe.

Hiermit erkläre ich, dass ich die Hilfe gewerblichen Promotionsberatern bzw. –vermittlern oder ähnlichen Dienstleistern weder bisher in Anspruch genommen habe noch künftig in Anspruch nehmen werde.

Hiermit erkläre ich mein Einverständnis, dass die elektronische Fassung meiner Dissertation unter Wahrung meiner Urheberrechte und des Datenschutzes einer gesonderten Überprüfung unterzogen werden kann.

Hiermit erkläre ich mein Einverständnis, dass bei Verdacht wissenschaftlichen Fehlverhaltens Ermittlungen durch universitätsinterne Organe der wissenschaftlichen Selbstkontrolle stattfinden können.

Dominik Greim, Bayreuth, 21. November 2020